First Principles Study of Magnesium/Oxygen Batteries and Glassy Solid Electrolytes

by

Jeffrey G. Smith

A dissertation submitted in partial fulfillment
of the requirements for the degree of
Doctor of Philosophy
(Mechanical Engineering)
in the University of Michigan
2018

Doctoral Committee:

       Associate Professor Donald J. Siegel, Chair
       Associate Professor Christian M. Lastoskie
       Professor Wei Lu
       Associate Professor Jeff Sakamoto

Jeffrey G. Smith

jgsmi@umich.edu

ORCID: 0000-0002-0613-8057

To Liam and Owen.

Acknowledgements

Table of Contents

List of Tables

List of Figures

Abstract

A transition to electrified transportation would benefit from the development of batteries with energy densities beyond that of Li-ion batteries. New battery chemistries and materials are needed to realize this transition. Metal-air and solid-state batteries have attracted attention due to their potential to meet this demand. This dissertation employs first-principles calculations to characterize materials of importance for two 'beyond Li-ion' chemistries: 1) the magnesium-air battery, and 2) solid state Li batteries employing a lithium thiophosphate Li_3PS_4 glassy electrolyte.

Mg-air batteries have high theoretical energy densities and rely on earth abundant materials. Nevertheless, metal-air batteries based on alkaline earth anodes have received limited attention and generally exhibit modest performance. In addition, many fundamental aspects of this system remain poorly understood, such as the reaction mechanisms associated with discharge and charging and the charge transport mechanisms within the discharge products. First principles calculations are employed to study the electrochemical and transport properties of the likely discharge products, MgO and MgO_2. Thermodynamic overpotentials for discharge and charge are calculated for several scenarios, including variations in surface stoichiometry and the presence/absence of intermediates in the reaction pathway. The calculations indicate that reaction pathways involving oxygen intermediates such as superoxides or peroxides are preferred. In agreement with recent experiments, our calculations predict that cells that discharge to MgO will exhibit low round-trip efficiencies. In contrast, MgO_2-based cells are predicted to approach round-trip efficiencies of 90%, suggesting that performance can be improved by 'steering' discharge towards formation of MgO_2.

Secondly, the transport properties of MgO and MgO_2 discharge products were investigated. The transport mechanisms in these compounds either are incompletely understood (in MgO_2) or remain a matter of debate (in MgO). For MgO, negative Mg vacancies and hole polarons were identified as the dominant charge carriers. However, their large formation energies suggest low equilibrium concentrations. A large asymmetry in the carrier mobility is predicted: hole polarons are mobile at room temperature, while Mg vacancies are immobile. Accounting for nonequilibrium effects such as frozen-in defects, the calculated conductivity data for MgO is shown to be in remarkable agreement with the three "Arrhenius branches" observed in experiments, thus clarifying the long-debated transport mechanisms within these regimes. In the case of MgO_2, electronic carriers are the most prevalent. Similar to MgO, equilibrium concentrations in MgO_2 are low, and moderate mobility further limits conductivity. If equilibrium behavior is realized, then (*i*) sluggish charge transport in MgO or MgO_2 will limit battery performance when these compounds cover the cathode support and (*ii*) what little conductivity exists in these phases is primarily electronic in nature (i.e., polaron hopping). Artificially increasing the carrier concentration via monovalent substitutions, or circumventing solid-state transport altogether via liquid-phase redox-mediators, are suggested as strategies for overcoming transport limitations.

Regarding solid electrolytes, the lithium thiophosphate family of glasses has reemerged as a promising candidate electrolyte due to its high conductivity and formability. However, due to their amorphous structure, the ion migration mechanisms that underlie their high Li-ion conductivity have been difficult to characterize. Our calculations reveal that: (*i*) cation migration events involve the nearly simultaneous migration of multiple adjacent cations, and (*ii*) cations are dynamically coupled to the reorientation and thermal vibrations of the PS_4 anions. This dynamic

coupling is expected to enhance the transport of cations through the anion sub-lattice and could be

used as a guide in the design of fast ion conductors.

Chapter 1

Introduction

1.1 Motivation

The introduction of Lithium-ion batteries in 1991 had tremendous impact on the development of portable electronic devices. It is increasingly likely that the next frontier for batteries will be the electrification of transport. Current Li-ion batteries fall short of the energy densities and targeted costs in the personal electric vehicle (EV) sector.[1] In response, the Department of Energy Vehicle Technologies Office has set goals to double the energy density and significantly reduce the cost of EV batteries by 2022.[2] Next generation Li-ion batteries utilizing advanced anode, cathode, and electrodes will accelerate vehicle electrification and may also play a role in stationary storage applications. However, due to the intrinsic energy density limitations of Li-ion batteries it is generally accepted that "beyond Li-ion" batteries will be necessary in the long term.[3–6] These batteries require new chemistries and materials to be explored and developed. This dissertation presents first-principles computational studies of two types of next-generation battery chemistries: magnesium-oxygen batteries and solid state batteries.

Magnesium−oxygen (or "Mg-air") batteries are attractive beyond Li-ion energy storage devices due to their high theoretical energy densities. The anode is earth abundant, less susceptible to dendrite formation during plating, and has a volumetric capacity nearly twice that of lithium. In total, a Mg/O_2 cell has a theoretical specific energy nearly seven times (3.9 kW h/kg) that of Li-ion batteries (0.57 kW h/kg) and even exceeds that of the well-studied "Li-air" system.

1

Another beyond Li-ion candidate is an all solid-state battery. Inorganic solid electrolytes offer improved safety, more compact cell design, and may facilitate the use of lithium-metal anodes. Solid solution electrolytes in the lithium thiophosphate family (based, for example, on a mixture of Li_2S and P_2S_5) exhibit some of the highest Li-ion conductivities, comparable to or exceeding that of liquid electrolytes in commercial Li-ion batteries. Additionally, they exhibit favorable mechanical properties compared to oxide electrolytes, enabling room temperature formability and good electrode contact during volume changes incurred during battery cycles.

1.2   Magnesium-Air Batteries

Magnesium-air batteries are attractive due to their essentially inexhaustible supply of cathode reactant (oxygen), which in theory allows for very high energy densities. They feature an electrochemical couple comprised of a magnesium anode and an oxygen cathode. Metal-air batteries based on zinc negative electrodes have historically received the most attention because zinc is relatively stable in aqueous electrolytes. Primary zinc-air batteries are commercially available and widely used in miniature hearing aids. Secondary zinc-air batteries have been under development for several decades and would be a promising power source for portable applications. However, progress has suffered from zinc dendrite formation during charging and parasitic carbonate formation restricting the gas diffusion electrode.[7]

The magnesium-air cell was under development by General Electric Company in the 1960s.[8] The cell design used a magnesium alloy anode, saline electrolyte, and an air cathode. During operation magnesium is precipitated as magnesium hydroxide and requires the anode and electrolyte to be replenished periodically. In a non-aqueous environment, magnesium and oxygen form a solid MgO_x discharge product of magnesium–superoxide, –peroxide, or –oxide within the

positive electrode (Figure 1.1). During charge, the process is (ideally) reversed and MgO_x decomposes to magnesium ions and molecular oxygen.
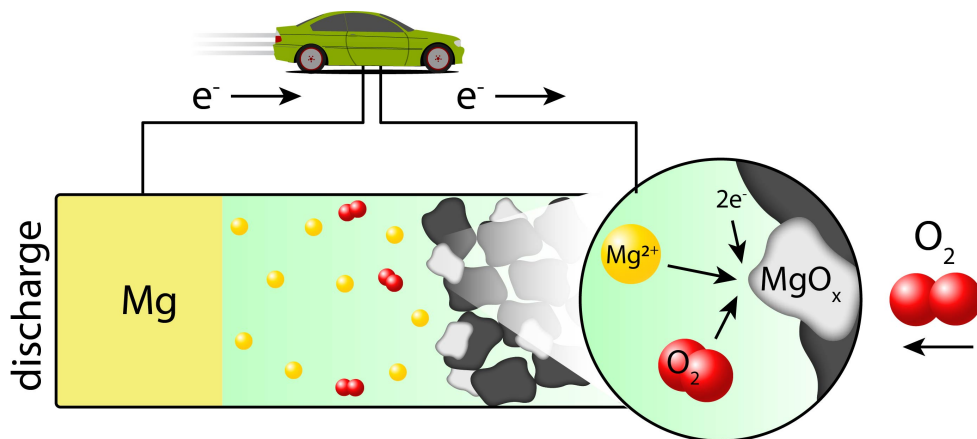
Figure 1.1. A magnesium-air battery.

Magnesium metal exhibits important advantages compared to lithium, such as higher volumetric capacity (3832 mAh cm^{-3} Mg vs. 2062 mAh cm^{-3} Li), suppressed dendrite formation, as well as lower cost.[9] The theoretical energy density of the Mg/O_2 couple, 3.9 kWh/kg for a cell that discharges to magnesium oxide (MgO), lies above Li-ion and Li-air, along with other metal-oxygen chemistries based on alkali metals (Figure 1.2).
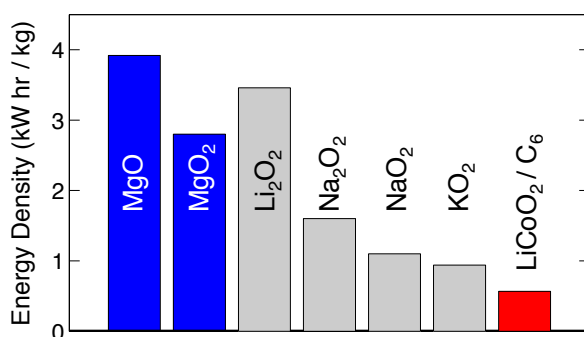
Figure 1.2. Theoretical specific energies of selected metal-oxygen chemistries (blue and grey bars) compared to Li-ion (red bar).

A brief report of a non-aqueous Mg-air battery first appeared in 2008,[10] followed in 2013 by a small number of more detailed publications.[11–13] In the experiments performed by Shiga *et al.*[11,12] it was concluded that the discharge product was MgO; furthermore, it was demonstrated that MgO was not rechargeable at moderate voltages. The addition of redox mediators enabled a recharge capacity. In the latter study, Vardar *et al.*[13] found the discharge product to comprise a mixture of MgO and MgO_2, with the peroxide component exhibiting more facile decomposition during recharge. Despite its promise, the non-aqueous system exhibited large overpotentials and limited rechargeability.

1.3 Sulfide Glassy Electrolytes

Inorganic solid electrolytes are a promising alternative to combustible liquid electrolytes used in conventional Li-ion batteries. Paramount are safety concerns as Li-ion batteries are becoming increasingly prevalent in electrifying transportation systems. Non-volatile and non-flammable solid state batteries alleviate safety concerns regarding battery puncture (e.g. EV crashes) and thermal runaway during harsh operating conditions. In addition, the use of a solid electrolyte is expected to enable high energy density anodes, such as Li metal, making these systems particularly attractive for long-range electric vehicle applications.

A century ago, Tubandt and Lorenz's discovery of the anomalous highly conductive α-AgI (1.3 S cm^{-1} at 147°C) phase lead to a new field of study, "fast ion conduction in solids," and encouraged the possibility of solid electrolytes for energy storage and conversion application.[14,15] From early investigations of silver and cuprous solid electrolytes some common features began to emerge. These included: anions arranged in a manner to provide a flat energy landscape allowing for a difference in potential energy the same order as the thermal energy; cations that were structurally disordered; a preference for monovalent cations; and highly polarizable anions were a

requirement.[16–18] The last insight likely lead to the development of sulfur-based solid electrolytes.[19]

Sulfide glasses were reported in 1980 as an alternative to oxides, when it was found that replacing the oxygen with sulfur increased the conductivity from 1 to 3 orders of magnitude.[20,21] It was well established that doping the oxide glasses with halide salts and modifying the glass former cations (Si, P, Ge) resulted in higher conductivity.[20] These practices quickly carried over to the lithium sulfides with a conductivity of 10^{-3} S cm^{-1} for the Li$_2$S–P$_2$S$_5$–LiI system, rivaling that of the silver oxide glasses.[21–23]
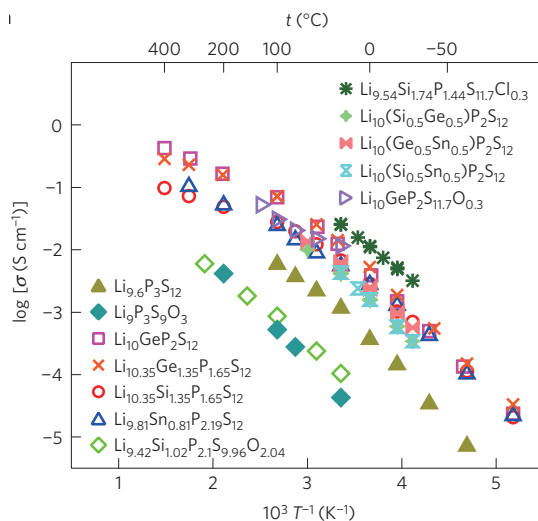
Figure 1.3. Arrhenius plots of the conductivity for sulfide solid electrolytes reported by Kato *et al.*[24]

The development of solid state batteries has been slowed for many years due to the lack of solid electrolytes with conductivity comparable to liquid electrolytes. Arrhenius plots of the conductivity for sulfide solid electrolytes are shown in Figure 1.3. More recently, several promising electrolytes from the lithium thiophosphate family have been reported with conductivities exceeding liquid electrolytes, these include: Li$_{10}$GeP$_2$S$_{12}$ (12 mS cm^{-1}), Li$_7$P$_3$S$_{11}$ (17 mS cm^{-1}), and Li$_{9.54}$Si$_{1.74}$P$_{1.44}$S$_{11.7}$Cl$_{0.3}$ (25 mS cm^{-1}).[24–26] However, the latter two suffer from poor

electrochemical stability.[24] In contrast, the chemical compositions Li_3PS_4 (0.5 mS cm^{-1}) and $Li_{9.6}P_3S_{12}$ (1.2 mS cm^{-1}) show high electrochemical stability against lithium metal.[24,27] Illustrating the need to have a variety of compositions as depicted in Figure 1.3. Glasses offer the possibility of continuously tuning the composition to meet future demands on material properties, for instance, formability and chemical stability.

1.4   Scope of Dissertation

This dissertation examines two battery technologies that aim to surpass the energy density of Li-ion systems: magnesium-air batteries and solid state batteries employing glassy sulfide electrolytes. First principles simulations are employed to characterize several phenomena related to the materials that comprise these next-generation battery systems.

Early experiments on magnesium-air batteries have demonstrated the inability to electrochemically decompose magnesium oxide in an efficient fashion upon recharge. Other noted inefficiencies include the presence of large overvoltages during discharge. In chapters 3 and 4, the electrochemical processes on the surfaces of likely discharge phases (MgO and MgO_2) are characterized, as are charge transport mechanisms within those phases. By clarifying these mechanisms we aim to reveal design strategies that can accelerate the development of magnesium-air batteries.

In the case of solid electrolytes, amorphous (or glassy) solids in the Li–P–S system are known to exhibit fast ion conduction, making them a promising class of materials. However, fundamental understanding of the local structure of mobile Li-ions, and connections between structure and transport mechanisms, are lacking in these materials. The goal of chapter 5 is to provide insight into of how local structural diversity and dynamical correlations can influence lithium transport. Computational techniques based on *ab initio* molecular dynamics are used to

predict the structure of the glassy LPS system, and to reveal how this structure influences and

evolves during ion migration.

Chapter 2

Methodology

2.1   Density Functional Theory

Less than one hundred years ago, a framework for the description of matter on the quantum scale was first assembled, based on contributions from Born, Heisenberg, and Schrödinger. The equation of motion at the atomic scale was provided by Schrödinger,

$$-i\hbar \frac{\partial \psi(\boldsymbol{r})}{\partial t} = \sum_i \frac{\hbar^2}{2m_i} \nabla^2 \psi + V(\boldsymbol{r})\psi \qquad (2\text{-}1)$$

which in principle explains all atomic phenomena except magnetism and relativity.[28]

Due to their complexity, predictions of atomic and electronic structures for systems involving more than a few atoms generally require approximations. First, the kinetic energies of the nuclei and electrons are often separated into two separate mathematical entities; this is known as the Born-Oppenheimer approximation. This is justified by the large difference in mass between nuclei and electrons, and the fact that the electrostatic forces acting on the two are nearly the same. Second, a large number of plane waves are needed to expand the orbitals of core electrons and valence electron near the nuclei core region. Pseudopotential methods replace the strong ion-electron interactions near the core by a much weaker and smoother potential in a manner where the valence electrons experience the same potential outside a designated cut-off radius. Thirdly, Density Functional Theory (DFT) introduces an important simplification by reducing the many-body problem of solving the 3N-dimensional wave function $\psi(\boldsymbol{r}_1, \boldsymbol{r}_1, \dots, \boldsymbol{r}_N)$ to one of solving

single electron wave functions in an effective non-local potential described by the electron density. This approach was introduced by Hohenberg and Kohn in 1964 and Kohn and Sham in 1965.[29,30] They proved that the total energy was a unique functional of the electron density, and the single-particle density that yielded the minimum value of the total energy functional was the ground-state density.

In DFT the total energy functional in a static, total electron-ion potential $V_{ion}(\mathbf{r})$ can be written in the form

$$E[n] = \int V_{ion}(\mathbf{r})n(\mathbf{r})d\mathbf{r} + \frac{1}{2}\iint \frac{n(\mathbf{r})n(\mathbf{r}')}{|\mathbf{r}-\mathbf{r}'|}d\mathbf{r}d\mathbf{r}' + T[n] + E_{xc}[n] \qquad (2\text{-}2)$$

where $n(\mathbf{r})$ is the density, the second term is the Coulomb energy, $T[n]$ is the kinetic energy of the system and $E_{xc}[n]$ is the exchange and correlation functional. The electronic density

$$n(\mathbf{r}) = \sum_i |\psi_i(\mathbf{r})|^2 \qquad (2\text{-}3)$$

is expressed in terms of the non-interacting single-particle wavefunctions, ψ_i. In order to determine the set of wave functions that minimize the energy functional, the single-particle Kohn-Sham equations are solved self-consistently,

$$\left[\frac{-\hbar^2}{2m}\nabla^2 + V_{ion}(\mathbf{r}) + V_H(\mathbf{r}) + V_{xc}(\mathbf{r})\right]\psi_i = \varepsilon_i\psi_i, \qquad (2\text{-}4)$$

ε_i is the Kohn Sham eigenvalue and V_H is the Hartree potential,

$$V_H(\mathbf{r}) = e^2 \int \frac{n(\mathbf{r}')}{|\mathbf{r}-\mathbf{r}'|}d\mathbf{r}', \qquad (2\text{-}5)$$

which describes the potential between the electron and the total electron density. $V_{xc}(\mathbf{r})$ is given formally be the functional derivative of the exchange correlation energy

$$V_{xc}(\mathbf{r}) = \frac{\delta E_{xc}(\mathbf{r})}{\delta n(\mathbf{r})}. \qquad (2\text{-}6)$$

2.2 Molecular Dynamics

Molecular dynamics describes the evolution of particle positions (typically taken as atoms) in time. For a system of N particles, with the ith particle having mass m_i and coordinates $\boldsymbol{q}_i = (x_i, y_i, z_i)$, the kinetic energy is

$$T = \frac{1}{2}\sum_{i=1}^{N} m_i \dot{\boldsymbol{q}}_i^2 \tag{2-7}$$

and potential energy $V = (t, \boldsymbol{q}_1, \boldsymbol{q}_2, \dots, \boldsymbol{q}_N)$, where the overdot denotes differentiation with respect to time. The MD trajectory consists of all particle paths along the time interval $[t_0 \; t_1]$, and the motion of the system is subject to the *principle of least action.* By introducing the function $\mathcal{L} = T - V$, called the *Lagrangian*, and minimizing the functional $\int_{t_0}^{t_1} \mathcal{L}\, dt$, the equations of motion that govern the system satisfy Euler's equation,

$$\frac{\partial \mathcal{L}}{\partial \boldsymbol{q}_i} - \frac{d}{dt}\frac{\partial \mathcal{L}}{\partial \dot{\boldsymbol{q}}_i} = 0. \tag{2-8}$$

For a computational cell with variable volume and shape under constant external hydrostatic pressure *p*, the *Lagrangian* is given by:[31]

$$\mathcal{L} = \frac{1}{2}\sum_{i=1}^{N} m_i \dot{\boldsymbol{s}}_i' \boldsymbol{G} \dot{\boldsymbol{s}}_i - V_N + \frac{1}{2}WTr\dot{\boldsymbol{h}}'\dot{\boldsymbol{h}} - p\Omega\ . \tag{2-9}$$

Here, the three vectors that span the edges of the computational cell $\boldsymbol{a}_1$, $\boldsymbol{a}_2$, and $\boldsymbol{a}_3$ form a 3×3 matrix $\boldsymbol{h}$, $\boldsymbol{G} = \boldsymbol{h}\boldsymbol{h}'$, where the prime denotes the transpose. $\boldsymbol{s}_i$ is a vector with components (ξ_i, η_i, ζ_i) which defines the position of the particle $\boldsymbol{r}_i = \xi_i\,\boldsymbol{a}_1 + \eta_i\,\boldsymbol{a}_2 + \zeta_i\,\boldsymbol{a}_3$, , Ω is the volume, and W determines the relaxation time of the internal stress subject to an external pressure. The temperature of the system is regulated by the Langevin thermostat, which mimics the coupling of

the system to another system at the desired temperature. The Langevin equation describes the stochastic motion of particles, such as particles suspended in a liquid (Brownian motion) or lithium in a conducting glass. Recognizing the functional dependence of T and V, equation 2-8 can be expressed in the form of Newton's equations of motion,

$$\dot{p}_i = f_i. \tag{2-10}$$

The Langevin equation adds a frictional force and a random force to the force acting on the particles,

$$\dot{p} = f - \xi v + \sigma \dot{w} \tag{2-11}$$

where w is a Wiener (random) process; the friction coefficient ξ, and the strength of the random forces σ, are related $\sigma = \sqrt{2\xi k_B T}$ by the fluctuation dissipation theorm.[32]

2.3 Phonon Frequencies

The Hellmann-Feynman forces are used in combination with the supplemented direct method[33] to evaluate the interatomic force constants. The total energy of a periodic crystal with small lattice distortions can be expressed as,[34]

$$E_{tot}(\{\Delta\tau\}) = E_{tot}^{(0)} + \sum_{a\kappa\alpha}\sum_{b\kappa'\beta} \frac{1}{2}\left(\frac{\partial^2 E_{tot}}{\partial\tau_{\kappa\alpha}^a \partial\tau_{\kappa'\beta}^b}\right)\Delta\tau_{\kappa\alpha}^a \Delta\tau_{\kappa'\beta}^b + \cdots \tag{2-12}$$

here $\Delta\tau_{\kappa\alpha}^a$ is the displacement along direction α of atom κ in cell a form its equilibrium position at τ_κ. The interatomic force constants are

$$C_{\kappa\alpha,\kappa'\beta}(a,b) = \left(\frac{\partial^2 E_{tot}}{\partial\tau_{\kappa\alpha}^a \partial\tau_{\kappa'\beta}^b}\right). \tag{2-13}$$

The dynamical matrix $\widetilde{D}$, defined from the Fourier transform of C is

$$\widetilde{D}_{\kappa\alpha,\kappa'\beta}(\boldsymbol{q}) = \frac{\widetilde{C}_{\kappa\alpha,\kappa'\beta}(\boldsymbol{q})}{(M_\kappa M_{\kappa'})^{\frac{1}{2}}} \tag{2-14}$$

where M_κ is the mass of atom κ, the eigenvalues of $\widetilde{D}$ are the squared phonon frequencies $\omega^2(\boldsymbol{q})$.[35]

For polar crystals there is a non-vanishing effective charge; the dynamical matrix is non-analytical, such that it depends on the direction that $\boldsymbol{q} = 0$ is attained. In this case, the interatomic force constant matrix is split into two parts

$$\tilde{C}_{\kappa\alpha,\kappa'\beta} = \tilde{C}_{\kappa\alpha,\kappa'\beta}(\boldsymbol{q}) + \tilde{C}^{NA}_{\kappa\alpha,\kappa'\beta}(\boldsymbol{q} \to 0) \tag{2-15}$$

the non-analytical term is evaluated as

$$\tilde{C}^{NA}_{\kappa\alpha,\kappa'\beta}(\boldsymbol{q} \to 0) = \frac{4\pi}{\Omega} \frac{\left(\sum_\gamma q_\gamma Z^*_{\kappa,\gamma\alpha}\right)\left(\sum_{\gamma'} q_{\gamma'} Z^*_{\kappa',\gamma'\beta}\right)}{\sum_{\alpha\beta} q_\alpha \varepsilon^\infty_{\alpha\beta} q_\beta} \tag{2-16}$$

where Ω is the volume of the cell, and $\varepsilon^\infty_{\alpha\beta}$ is the electronic dielectric permittivity tensor and Z^* is the Born effective charge tensor for each atom.[34]

2.4 Raman Spectra

The Raman susceptibility tensor is constructed as[36]

$$R^j_{\alpha\beta} = \sqrt{\frac{V_0 \hbar}{2\omega_j}} \sum_\kappa \frac{\partial \chi_{\alpha\beta}}{\partial \tau(\kappa)} \frac{e(j,\kappa)}{\sqrt{M_\kappa}} \tag{2-17}$$

where V_0 is the volume of the primitive cell and χ is the high frequency electronic susceptibility tensor. For crystals, the differential cross section for non-resonant first order Raman scattering is given by

$$\frac{d\sigma^2}{d\Omega d\omega} = N_0 \frac{\omega_s^4}{c^4 V_0} \sum_j \left| e_s \cdot R^j_{\alpha\beta} \cdot e_i \right|^2 \left(n_j(\omega_j, T) + 1\right) \frac{\hbar}{2\omega_j} \delta(\omega - \omega_j) \tag{2-18}$$

here N_0 is the number of primitive cells, e_s and e_i are the scattered and incident light polarization versors, and ω_j is the frequency of the j-th phonon mode.[36]

Chapter 3

Reaction Mechanisms and Theoretical Limiting Potentials of Magnesium-Oxygen Batteries

3.1 Introduction

A Mg/O$_2$ cell that discharges to MgO is expected to be a difficult system to cycle, as MgO is chemically inert[37] and does not typically decompose under moderate conditions.[38] Shiga *et al*[11,12] demonstrated a Mg/O$_2$ battery with a non-aqueous electrolyte. The discharge plateau of ~1.1-1.2 V was attributed to the formation of MgO, and is well below the theoretical voltage of 2.95 V. Decomposition of the discharge product was not observed for charging potentials up to 3.2 V and at an elevated temperature of 60°C, unless a redox mediator was employed. Additionally, Abraham[10] has described a Mg/O$_2$ battery with a discharge voltage between 0.7 to 1.1 V at room temperature.

Given the low discharge voltages and apparent irreversibility of MgO, a potentially more desirable discharge product is magnesium peroxide, MgO$_2$. The analogous Li/O$_2$ system provides support for this strategy, as it is now well established that cells that discharge to Li$_2$O$_2$ can be reversed with the application of moderate potentials, while those that form Li$_2$O cannot.[39–42] MgO$_2$ is stable up to temperatures of 345°C,[43] and only marginally less favored thermodynamically than MgO: ΔG_f^0(MgO) = −568.9 kJ/mol *vs.* ΔG_f^0(MgO$_2$) = −567.8 kJ/mol.[44,45] In addition, recent experiments involving Na/O$_2$ cells have shown that kinetic factors can play a role in determining

the composition of the discharge phase. For example, Hartmann *et al.*[46] have observed that Na/O$_2$

cells discharge to sodium superoxide (NaO$_2$) despite the higher stability of the peroxide phase,

Na$_2$O$_2$. Taken together, these data suggest that an Mg/O$_2$ battery that discharges to MgO$_2$ – rather

than to MgO – could be possible, and may be desirable from the standpoint of reversibility.

The operation of an Mg/O$_2$ cell is expected to be governed by the following half-reactions

at the anode and cathode:

Anode:

$$Mg \rightleftharpoons Mg^{2+} + 2e^- \tag{3-1}$$

Cathode:

$$Mg^{2+} + 2e^- + \frac{1}{2}O_2 \rightleftharpoons MgO, \quad U_0 = 2.95 \text{ V} \tag{3-2}$$

$$Mg^{2+} + 2e^- + O_2 \rightleftharpoons MgO_2, \quad U_0 = 2.94 \text{ V} \tag{3-3}$$
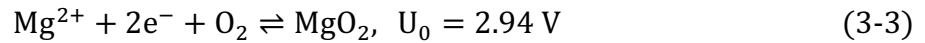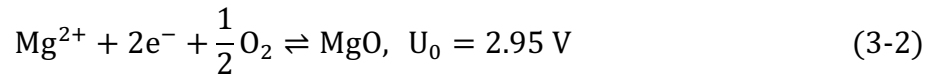
Here U_0 represents the theoretical cell voltage. MgO adopts the rock salt crystal structure with a

lattice constant of 4.21 Å, whereas MgO$_2$ adopts the pyrite crystal structure with a lattice constant

of 4.84 Å. Vannerberg has prepared the peroxide compound by treating MgO with hydrogen

peroxide between 0-20°C.[47] Vol'nov also prepared MgO$_2$ at room temperature using an aqueous

solution of magnesium hydroxide and hydrogen peroxide, followed by drying with phosphorous

pentoxide.[43] Magnesium superoxide, Mg(O$_2$)$_2$, has also been reported, and was prepared using an

ozone-saturated solution of Freon with MgO$_2$ suspended in the same media. The presence of the

superoxide radical, O$_2^-$, was confirmed by EPR spectra. X-ray diffraction on the yellowish

Mg(O$_2$)$_2$ crystals indicated a rhombohedral crystal structure with lattice constants a = 7.93 Å and

α = 93°. Because Mg(O$_2$)$_2$ decomposes[48] at temperatures above -30°C it is unlikely to be a viable

candidate discharge product in an Mg/O$_2$ battery.

The present study aims to clarify the reaction mechanisms and energetics associated with charge and discharge of an Mg/O_2 cell. Density functional theory calculations, in combination with the method of Norskov *et al.*,[49–51] are used to predict the theoretical limiting potentials for several plausible reaction pathways. This method has previously been used to describe trends in electrochemical reactions in aqueous environments[52,53] and in metal/O_2 batteries based on Li,[54–56] Na,[57] Zn,[58] and Al.[59] Application to the Mg/O_2 system can facilitate an understanding of the origin of the low discharge voltage and irreversibility observed in prior experiments.[11,12] Such an analysis could also reveal strategies for improving performance.

Toward these goals, in this Chapter we computationally examine discharge/charge reactions as a function of discharge product (MgO *vs.* MgO_2), surface stoichiometry (stoichiometric *vs.* oxygen-rich), and for pathways with and without intermediate phases. The calculations suggest that thermodynamic limitations are a major contributor to the low potentials observed in cells that discharge to MgO. In addition, they reveal that it is energetically favorable to reduce (i.e., during discharge) and evolve (i.e., during charging) oxygen via multi-step pathways that involve intermediate, less-reduced species. In contrast to the poor performance predicted for MgO-based cells, discharging to an MgO_2 product along a pathway that involves electrochemistry on oxygen-rich (superoxide-terminated) surfaces yields the best combination of high discharge voltage and low charging voltage. In the absence of other transport or kinetic limitations, these data suggest that battery performance can be maximized via cathode designs or operating scenarios that favor the formation of an MgO_2 discharge product.

3.2   Computational Details

First-principles calculations were performed using the Vienna *ab initio* simulation package (VASP code).[60–63] The generalized gradient approximation (GGA) expressed with the formulation of

Perdew-Burke-Ernzerhof (PBE) was used for the exchange-correlation energy.[64] Blochl's projector augmented wave method[65] was used to treat the core-valence electron interaction, with valence states of *2s* for Mg and *2s2p* for O. For calculations involving the conventional unit cell for bulk phases, the Brillouin zone was sampled with a Gamma-centered k-point mesh of $8 \times 8 \times 8$ for oxides/peroxides and $16 \times 16 \times 16$ for metals. The plane-wave cutoff energy was set to 520 eV and a force tolerance of 0.01 eV/Å was used for all geometry optimizations. For bulk phases the cell shape, volume, and atom positions were relaxed; surface calculations employed in-plane lattice dimensions based on relaxation of the respective unit cell. To accommodate the large simulation cells necessary for calculations of reaction energies, a reduced plane-wave cutoff energy of 400 eV and force tolerance (0.04 eV/Å) were used. All calculations were spin polarized.

3.3 Results and Discussion

3.3.1 Bulk Phases

The conventional cell of face centered cubic (FCC) MgO (space group: *Fm3m*) and pyrite MgO_2 (space group: *Pa3*) from Vannenburg[47] are illustrated in Figure 3.1. The calculated lattice constants for HCP Mg (a = 3.19 Å, c = 5.18 Å), MgO (a = 4.24 Å), and MgO_2 (a = 4.88 Å) are all in good agreement with experimental values: Mg (a = 3.21 Å, c = 5.20 Å),[66] MgO (a = 4.21 b),[67] and MgO_2 (a = 4.84).[47] In MgO_2 the peroxide bond length was calculated to be 1.51 Å, which compares favorably with the value measured by X-ray diffraction, 1.50 Å.[47] An additional phase of interest is oxygen gas (O_2), for which we calculate a bond length of 1.23 Å, compared to the experimental value of 1.21 Å.[68]

3.3.2 Surface Stability

As described in more detail below, discharge and charge reactions are assumed to occur on the surfaces of MgO or MgO$_2$ discharge products. Modeling these reactions therefore requires knowledge of the low-energy facets of these compounds. Surface energies were evaluated for 31 distinct surface terminations of MgO and MgO$_2$ by cleaving along three low index directions: (100), (110), and (111). A vacuum region of 10 Å separated each of the two surfaces spanning a given slab, and both surfaces were identical, thereby avoiding spurious dipole interactions along the non-periodic direction of the computational cell.

MgO   MgO$_2$
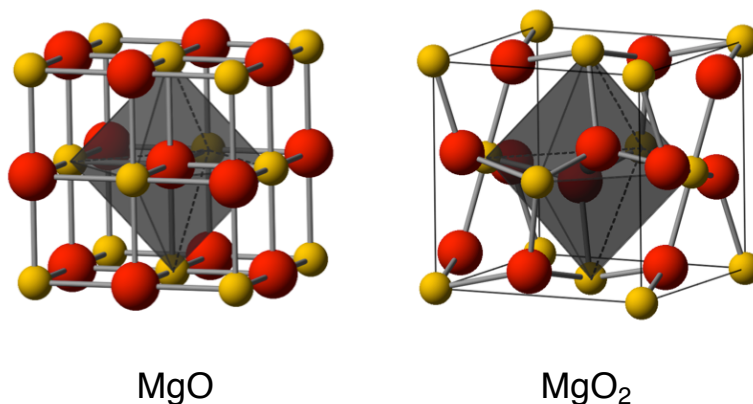
Figure 3.1. Crystal structure of MgO and MgO$_2$. (Left) The rock salt crystal structure of MgO; oxygen is octahedrally coordinated by Mg. (Right) The pyrite crystal structure of MgO$_2$; the covalently bonded oxygen dimer (O$_2$) is octahedrally coordinated by Mg. Red spheres represent oxygen atoms, yellow spheres are magnesium.

Surface energies were calculated using the methodology described by Reuter and Scheffler.[69] The most stable surface composition for a given cleavage direction will minimize the surface free energy,

$$\gamma = \frac{1}{2A}\left(G^{\text{slab}} - \sum_i n_i \mu_i\right) \qquad (3\text{-}4)$$

Here G^{slab} represents the energy of the surface slab, while n and μ are, respectively, the number and chemical potential of species i in the slab. A is the area of the surface, and the factor of two accounts for the double-sided slab model. The chemical potential of Mg (μ_{Mg}) and O_2 (μ_{O_2}) are linked by the expression,

$$g_{\text{MgO}_x} = \mu_{\text{Mg}} + (x/2)\mu_{O_2} \tag{3-5}$$

where g_{MgO_x} refers to the energy per formula unit of MgO_x, (x = 1, 2). The Gibbs free energy per oxygen atom is a function of temperature and pressure, $dg = -SdT + Vdp$. The chemical potential of an ideal gas at a temperature T and pressure p can be expressed as:

$$\mu_O(T,p) = \mu_O(T,p^0) + \frac{k_B T}{2}\ln\left(\frac{p}{p^0}\right) \tag{3-6}$$

Using Equation 4, 5, and 6, the surface energy at a fixed temperature can therefore be written as a function of oxygen chemical potential or O_2 pressure alone:

$$\gamma_{\text{MgO}_x}(T,p,n_{\text{Mg}},n_O) = \frac{1}{2A}\left(G^{\text{slab}}(T,p,n_{\text{Mg}},n_O) + (xn_{\text{Mg}} - n_O)\mu_O(T,p) - n_{\text{Mg}}g_{\text{MgO}_x}\right) \tag{3-7}$$

We assume that oxygen in the gas phase is in equilibrium with oxygen dissolved in the battery's electrolyte.

To examine the relative stability of each MgO_x surface, the surface energy is plotted as a function of O_2 pressure and oxygen chemical potential. The chemical potential of oxygen gas at standard conditions ($p^0 = 0.10$ MPa, $T^0 = 298.15$ K) is defined as,

$$\mu_{O_2} = \mu_{O_2}^{\text{DFT}} - TS_{\text{expt.}} + \left(\Delta E^{\text{DFT}} - \Delta H_f^0\right), \tag{3-8}$$

where empirically-determined entropy contributions (TS = 0.63 eV)[44] are included. Here the last term represents an empirical correction (applied on a per O_2 basis) evaluated as the difference between the calculated formation energy, ΔE^{DFT}, and the experimental enthalpy of formation, ΔH_f^0, for the compound in question (i.e., either MgO or MgO_2). These corrections – 1.46 eV/O_2 for MgO

and 1.26 eV/O_2 for MgO_2 – are similar in spirit to those proposed elsewhere,[55,70–72] and account for the well-known over-binding of O_2 gas, as well as for oxygen oxidation state errors. Contributions from pressure, vibrational energy, and entropy are neglected for solid phases.

The surface energies for all surfaces considered are summarized in Figure 3.2; ball-and-stick models of low energy structures appear in Figure 3.3. We first turn our attention to the surfaces of MgO (top row of Figure 3.2). In general, the most stable termination of rock salt-based compounds is the nonpolar (100) surface.[73] Consistent with this expectation, Figure 3.2 shows that the MgO (100) stoichiometric surface is the lowest in energy overall, with a calculated surface energy of 56 meV/$Å^2$. (The second most-stable MgO surface is the (110) stoichiometric surface, which has a much higher surface energy of 137 meV/$Å^2$.) Each oxygen atom in the stoichiometric (100) surface is coordinated by five Mg ions and the in-plane Mg-O distance is the same as in the bulk, 2.12 Å.

The calculated and experimental surface energies for MgO (100) are summarized in Table 3.1. The experimentally-determined surface energy is expected to be slightly higher than the calculated value of a pristine surface due to the presence of different crystallographic planes and surface atom vacancies typical of real surfaces.[74–76]
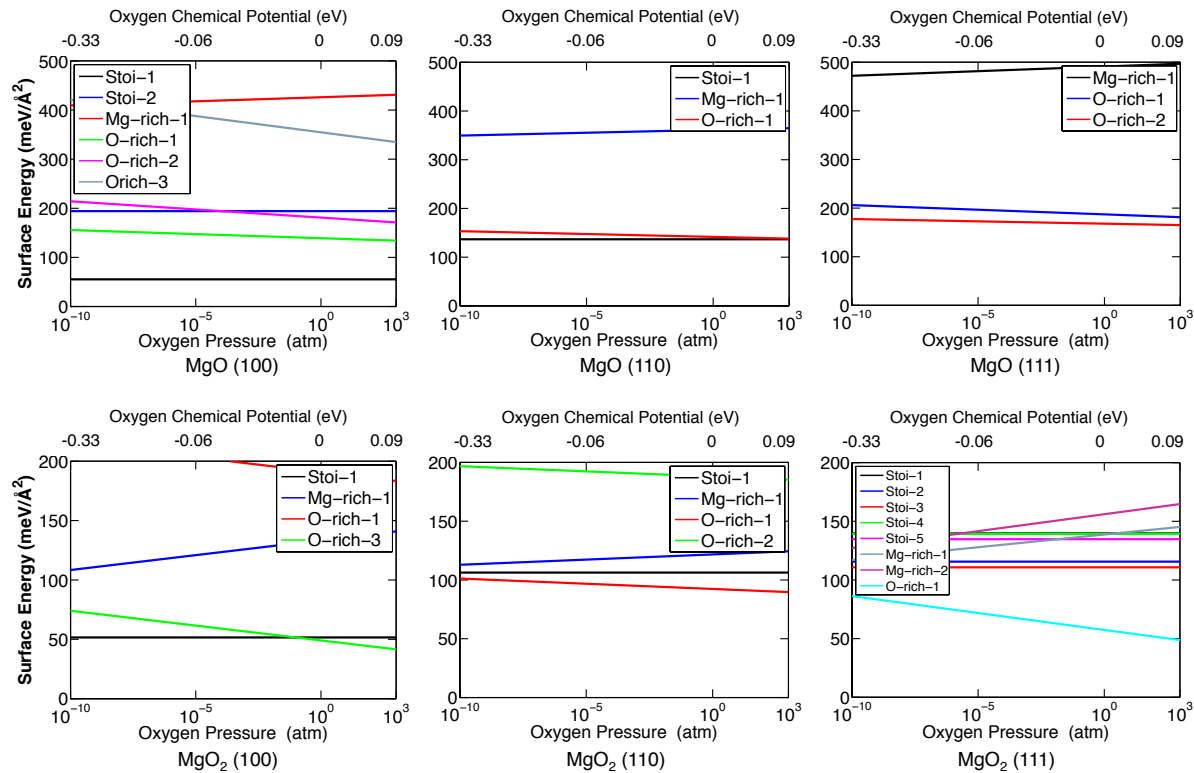
Figure 3.2. Surface free energies of MgO and MgO$_2$ as a function of oxygen chemical potential (top axis) and oxygen pressure (bottom axis) at 300 K. The notation 'O-rich' and 'Mg-rich' refer to the stoichiometry of the slabs. The chemical potential scale is defined to be zero at STP.

(a) MgO (100) Stoi-1   (b) MgO$_2$ (100) Stoi-1

(c) MgO$_2$ (100) Orich-3   (d) MgO$_2$ (111) Orich-1
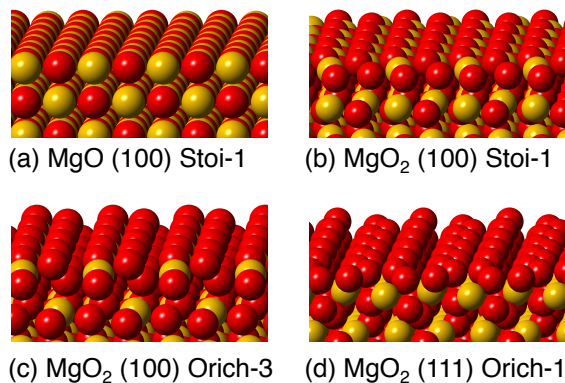
Figure 3.3. The most stable surface terminations for MgO and MgO$_2$. Red indicates oxygen atoms and yellow magnesium atoms.

Three nearly degenerate terminations comprise the stable surfaces of MgO_2, Figure 3.3 bottom panel. Two of these occur on the (111)-oriented facet, and one on the (100) facet. The surface energies across all three fall within a narrow range from 49 to 57 meV/$Å^2$, and include (in order of increasing surface energy): oxygen-rich (100) 'Orich-3', stoichiometric (100) 'Stoi-1', and oxygen-rich (111) 'Orich-1' (See Table 1). The stoichiometric surfaces have a 2 to 1 ratio of O to Mg atoms; for the Orich surfaces this ratio is greater than 2. More specifically, the surface layers of the Orich-1 and Orich-3 slabs have a stoichiometry with an O to Mg ratio of 4. In these cases the surface oxygen dimers have a bond length of 1.35 Å, a Bader charge of approximately -1, and a non-zero magnetic moment. These features are consistent with a the presence of a superoxide-like surface layer.[48] Below this surface layer the electronic structure quickly reverts to peroxide-like behavior, with O_2 bond lengths of 1.51 Å, Bader charges consistent with the presence of O_2^{2-}, and the absence of a magnetic moment.

Table 3.1. Surface energies for the most stable surfaces of MgO and MgO_2 at standard conditions.

Surface	Surface Energy (meV/$Å^2$)
MgO (100)-Stoi-1 (this work)	55
MgO (100)-Stoi-1 (expt)[74]	72
MgO (100)-Stoi-1 (expt)[75]	83
MgO (100)-Stoi-1 (calc)[76]	56
MgO_2 (100)-Stoi-1	52
MgO_2 (100)-Orich-3	49
MgO_2 (111)-Orich-1	57

The calculated surface energies were used to predict the equilibrium crystallite shapes for MgO and MgO_2 via the Wulff construction,[77] shown in Figure 3.4. For MgO, the stoichiometric (100) surface comprises the entire surface area of the crystallite. In contrast, two facets, (100) and (111), comprise the surface area of the MgO_2 crystallite, which is a 14-sided tetradecagon. The

yellow (111) facet comprises 54% of the surface area, and the blue (100) facet covers the remaining 46%. Given the slightly lower energies associated with the Orich-1 and Orich-3 terminations (Table 1), we expect that the surfaces of MgO_2 crystallites will be predominantly oxygen-rich, with a superoxide-like surface layer.

Having established the stable surfaces of MgO and MgO_2, the electrochemistry associated with discharge and charge reactions occurring on these surfaces was subsequently examined.

3.3.3   Reaction Energies

3.3.3.1   Review of the Theoretical Limiting Potential Method and its Application to the MgO (100) Surface.

Limiting potentials were evaluated for two reaction pathways (described below) involving discharge/charge reactions on MgO (100), following the approach of Norskov *et al.*[49,51,54,55,78–81] This treatment models the discharge process as a series of adsorption events onto the surface of an existing particle of the discharge product.

For illustrative purposes, Figure 3.5 presents a generic discharge process. In the present case the surface is assumed to be the stable Stoi-1 (100) surface of MgO. The surface is modeled using a 2×2 expansion of the primitive surface cell. In this geometry each surface layer contains 8 formula units of MgO. We define a "complete" discharge reaction pathway as consisting of the consecutive adsorption or deposition of 8 additional MgO formula units. At the completion of this process the thickness of the surface slab will have increased by two single formula-unit layers; atoms are added to each face of the slab so as to maintain identical surfaces. In a similar fashion, recharge can be modeled by the sequential removal of individual molecules or atoms from the surfaces.

Each step in the discharge or charging sequence is referred to as an "elementary electrochemical step." During a discharge step, two electrons are transferred from the Mg anode to the cathode, where they reduce oxygen; reduced oxygen can then also combine with an Mg^{2+} cation. (Similarly, during charging two electrons are removed.) The energy change associated with each elementary step i is given by the free energy of reaction $\Delta G_{rxn,i} = G_{products} - G_{reactants}$. During discharge, $G_{products}$ refers to the energy of the (neutral) species adsorbed on MgO (100); for example, these may be Mg^0, MgO, MgO_2, *etc.* The energy of the reactants, $\Delta G_{reactants}$, is given by a combination of the MgO slab (including any species adsorbed in previous steps) and magnesium and oxygen atoms in an appropriate reference state. The chemical potential of magnesium is taken to be that of HCP magnesium metal (i.e., equal to the chemical potential of the Mg anode), and the chemical potential of oxygen is that of oxygen gas at STP. As previously mentioned, this reference state assumes that oxygen dissolved in the electrolyte is in equilibrium with gas-phase oxygen. With this definition, the energy change associated with an elementary electrochemical (discharge) step, $\Delta G_{rxn,i}$, corresponds to the adsorption energy for an adatom of $Mg^0 = Mg^{2+} + 2e^-$, or of a molecule of MgO_x.

We note that the sum of all elementary reaction energies must equal the free energy associated with the growth of (two) formula-unit layers on the slab's surfaces:

$$\Delta G^{layer} = -\sum_i \Delta G_{rxn,i}^{elementary} \tag{3-9}$$

The energy of the initial configuration (i.e., before discharge) corresponds to reaction coordinate 0 of Figure 3.5 (solid line), and is equal to the sum of the energies of the bare surface layer and the energy of all magnesium and oxygen atoms in the reservoir. During discharge, each subsequent reaction at the surface reduces the free energy of the system until all reactants have been adsorbed, corresponding to a free energy which is equal to zero by definition (see reaction coordinate 8 in

Figure 6, solid line). Each change in free energy associated with an elementary discharge step is evaluated as,

$$\Delta G_{rxn,i}^{elem} = G^{step}(n_{Mg}^*, m_O^*) - \left\{ G_{previous}^{step} + m_{Mg}\mu_{Mg} + m_O\mu_O \right\}, \qquad (3\text{-}10)$$

where, $G^{step}(n^*, m^*)$ refer to the energy of the slab supercell after n_{Mg} and m_O, ions (respectively) have adsorbed on the surface. Likewise, $G^{step}_{previous}$ is the total energy of the computational cell from the previous step.

In principle, many different reaction pathways may be followed during discharge or charge. Here, two plausible pathways are examined. (For simplicity, the examples below are described assuming a discharge pathway.) The pathways include: (*i.*) A "single step" pathway where oxygen is reduced to a 2^- oxidation state through a one-step reaction:

$$\left(Mg^{2+} + 2e^- \right) + \frac{1}{2}O_2 + * \rightleftharpoons MgO^* \qquad (3\text{-}11)$$
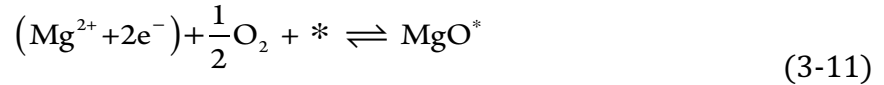
and (*ii.*) a multi-step pathway wherein oxygen is reduced incrementally to a 2^- oxidation state via two consecutive reduction reactions. The initial deposition results in the formation of an adsorbed peroxide intermediate molecule (MgO_2); a subsequent deposition of Mg^{2+} combined with transfer of 2 additional electrons forms 2 formula units of adsorbed MgO:

$$\left(Mg^{2+} + 2e^- \right) + O_2 + * \rightleftharpoons MgO_2^* \qquad (3\text{-}12a)$$

$$MgO_2^* + \left(Mg^{2+} + 2e^- \right) \rightleftharpoons 2MgO^* \qquad (3.12b)$$
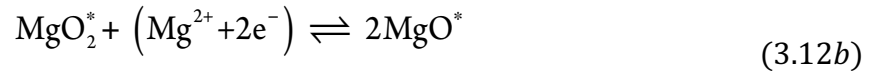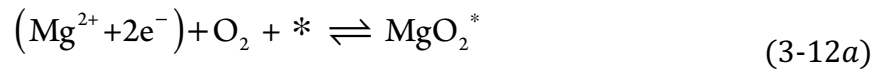
Here a lone asterisk denotes a surface site, while a superscript asterisk denotes a surface-adsorbed species.

The forward direction in the preceding reactions involve oxygen reduction (ORR) and the precipitation of a solid MgO_x discharge product, while the reverse corresponds to the oxygen

evolution reaction (OER) and the dissolution of that product during charging. In both pathways the elementary reactions (Eq. 3-11 or 3-12a + 3-12b) are repeated until a full surface layer has been added (discharge) or removed (charge). The disassociation of O_2 at the surface is not taken into account as this is a kinetic process, and the present formalism is concerned only with thermodynamics.
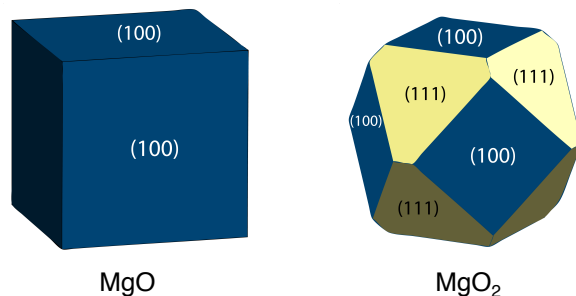
Figure 3.4. Equilibrium crystallite shapes predicted from the Wulff construction.

The multi-step reaction mechanism 3-12a + 3-12b is motivated by the thermodynamic theory of electron transfer.[82] In this pathway charge is temporarily "stored" in an intermediate, peroxide adsorbed species (MgO_2*) on the way to achieving a final oxidation state of 2- in MgO*. The peroxide intermediate has a higher oxidation state (i.e., it is less reduced compared to the oxide) wherein each oxygen atom has an effective charge of 1-. The present computational approach has previously been used to elucidate the important role played by intermediate species in other electrochemical processes, such as hydrogen evolution and oxidation,[82] oxygen evolution and reduction,[78,83] and carbon dioxide reduction.[84]

We emphasize that all steps in Reactions 3-11 and 3-12a + 3-12b are electrochemical steps that involve electron transfer. Although some studies have included non-electrochemical (i.e., chemical) steps in their analyses,[57,85] chemical steps are potential-independent and therefore do

25

not contribute to the useful electrical work supplied by the cell during discharge. For this reason we focus only on electrochemical steps.

3.3.3.2   MgO (100) Single-Step Reaction

The black line in Figure 3.6 depicts the free energy profile for the single step reaction pathway of Reaction 11. Reaction coordinate zero corresponds to the state before both charge transfer and deposition onto the MgO (100) surface (i.e., this is the "clean" surface). Similarly, reaction coordinate 8 corresponds to the final surface; this surface is equivalent to the initial surface except that the slab has grown thicker via the deposition of two formula-unit layers. As each layer corresponds to the addition of 8 Mg and 8 O ions, a total of 16 electrons are transferred per layer.

For each elementary step in the discharge sequence a search over possible deposition locations on the surface is carried out. Once identified, the lowest energy adsorption site is occupied, and its energy is recorded; the next deposition event then takes place in the presence of the adsorbate deposited in the previous step. At each step all atoms on the surface are relaxed to their minimum-force positions.
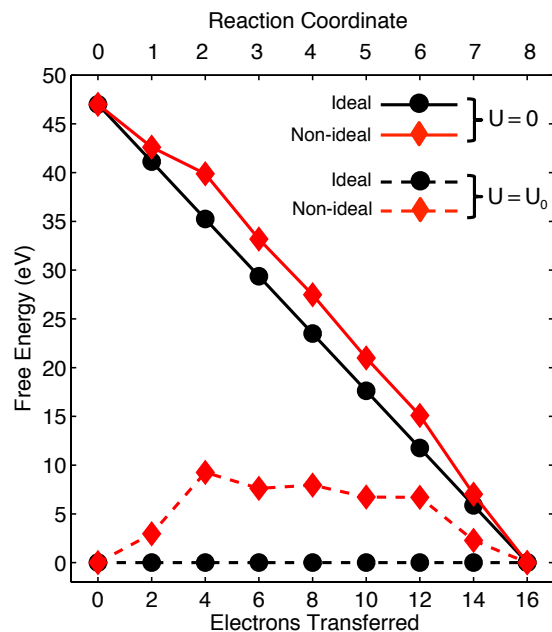
Figure 3.5. Prototypical discharge reactions. Black curves represent an ideal reaction pathway depicted at: zero applied voltage, $U = 0$ (solid line), and at an applied voltage $U = U_0$ equal to the cell's theoretical voltage (dashed line). The reaction is considered ideal because the voltage associated with each elementary step is equal to the theoretical voltage associated with the formation energy of the discharge product. For comparison, the red curves depict a non-ideal reaction plotted at $U = 0$ (solid) and $U = U_0$ (dashed).

For discharge to be spontaneous each elementary electrochemical step i must be "downhill," i.e., $\Delta G_{rxn,i} < 0$. For an idealized discharge mechanism, $\Delta G_{rxn,i}$ for each step will be equal to the formation energy, $\Delta G_f(MgO)$ of bulk MgO. When the energy of each elementary step is plotted *vs.* the number of electrons transferred, this idealized scenario yields a straight line comprised of 8 identical line segments, as shown using the solid black line in Figure 3.5. Each segment corresponds to an elementary deposition step during the growth of a single formula-unit layer on the MgO (100) surface.

The slope of each segment, which is equal to that of the full line, is the theoretical cell voltage associated with the formation energy of bulk MgO through the Nernst equation:

$$U_0 = -\frac{\Delta G_f^{bulk}}{e\nu_{e^-}},$$

(3-13)

where e is the charge of an electron and ν_e is the stoichiometric coefficient (2) associated with the number of electrons in the reaction. Such an idealized discharge mechanism would exhibit zero thermodynamic overvoltage.

Of course in a real system the energy change associated with an elementary discharge step need not be equal to the bulk formation energy: surface heterogeneity and deposition events that do not deposit a stoichiometric formula unit can result in energy changes $\Delta G_{rxn,i}$ which are greater or less than that for the formation energy of bulk MgO. During discharge, reactions steps whose energy change is less exergonic than $\Delta G_f(MgO)$ contribute to the discharge overvoltage. According to Norskov's definition, the least exergonic of these steps along a given reaction pathway is defined as the potential determining step. This step defines the limiting potential for discharge, $U^{\,discharge}$:

$$U^{discharge} = \min\left|\frac{\Delta G_{rxn,i}(U=0)}{e\nu_{e^-}}\right|$$

(3-14)

here, the 'min' function selects the elementary reaction that is the least exergonic.

During charging all elementary reaction steps should be endergonic. Steps having a free energy change which are more endergonic than the decomposition free energy of bulk MgO contribute to the charging overvoltage. Following Norskov's definition, the most "uphill" of these steps is defined as the potential determining step, with a limiting potential of,

$$U^{charge} = \max\left|\frac{\Delta G_{rxn,i}(U=0)}{e\nu_{e^-}}\right|.$$

(3-15)

A key goal in generating a free energy diagram such as Figure 3.6 is to identify the potential determining steps for charge and discharge. These predictions provide information regarding the expected efficiency of an Mg/O_2 cell. Moreover, by comparing the reaction energies associated with different reaction pathways it may be possible to identify thermodynamically favorable mechanisms. To assist in identifying the limiting potentials, it is helpful to plot the free energy diagram at an applied potential equal to the theoretical voltage of the cell, i.e., $U = U_0$. For an Mg/O_2 cell that discharges to MgO this would correspond to a voltage of 2.95 V (Eq. 3-2). This applied voltage shifts the energy of electrons present in the discharge pathway by eU_0, and thereby also shifts the electrochemical potential of magnesium such that it is the same in the anode and cathode. (In other words, the applied voltage exactly counter-acts the thermodynamic driving force for discharge.) In this case the idealized pathway described previously (Figure 3.5) would appear as a horizontal line at zero on the free energy diagram, i.e., $\Delta G_{rxn,i}(U=U_0) = 0$, for all steps since the change in free energy associated with every elementary reaction is opposed by the bias potential. The black dashed line in Figure 3.5 illustrates this scenario.
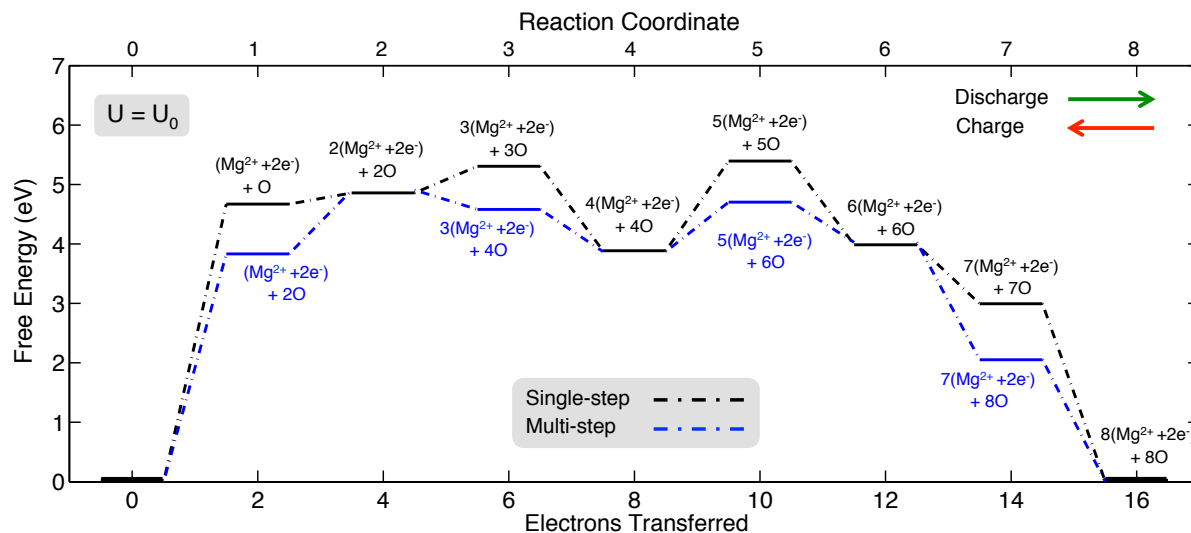
Figure 3.6. Free energy diagram for discharge and charge on the MgO (100) surface. Calculated free energy diagram for discharge (read left-to-right) and charging (read right-to-left) of an Mg/O_2 cell, assuming that all reactions occur on the MgO (100) surface. The black line refers to the single step pathway of Eq. 3-11; the blue line refers to the multi-step pathway, Eq. 3-12a-b. All energies are plotted assuming the application of a potential, U, equal to the theoretical cell voltage, $U = U_0$. The identity of the species that are adsorbed on the surface during each elementary discharge reaction is indicated with text; these same species are desorbed during charging. A total of 8 Mg^{2+} ions, 8 oxygen atoms, and 16 electrons are added to the surface to replicate its initial structure.

For an actual (i.e., non-ideal) discharge pathway plotted at $U = U_0$, free energy changes associated with elementary reaction steps will appear as a sequence of uphill and downhill steps; this is illustrated by the red dashed line in Figure 3.5. As previously mentinoed, the non-ideal nature of a pathway arises from differences in the composition of the species adsorbed in successive steps, and from heterogeneity in the surface adsorption sites.

Following this convention, potential determining steps can be straightforwardly identified as uphill steps in the reaction pathway when plotting with an applied bias of $U = U_0$. Thus for charge or discharge, an elementary reaction with a positive reaction energy, $\Delta G_{rxn,i}(U_0) > 0$, can be associated with a limiting potential. The magnitude of the uphill step is proportional to the amount of 'lost' or 'unharvested' energy during discharge, or the amount of additional energy

input required for charge. The largest of these steps over the entire pathway is defined as the potential determining step,

$$\max\left[\Delta G_{rxn,i}\left(U=U_0\right)\right]=\eta e \nu_{e^-}.$$

(3-16)

This step determines the "thermodynamic overvoltage," η, which is defined as the difference in the theoretical cell voltage and the limiting potential:

$$\eta^{discharge}=U_0-U^{discharge}, \quad \eta^{charge}=U^{charge}-U_0.$$

(3-17)

Note that the limiting potential is always an uphill step when plotting at $U = U_0$. For discharge, it is the largest uphill step when reading the reaction energy profile from left-to-right; for recharge, it is the largest step reading right-to-left.

Referring now to the single-step pathway (Eq. 3-11), during discharge single Mg and O atoms are deposited on the (100) surface at each step. Energy levels for each step are shown in Figure 3.6. As each reaction coordinate represents the minimum energy configuration of reactants and products, the diagram is equally valid for charging (right-to-left). The potential determining step for discharge is the initial deposition event, corresponding to the transfer of the first 2 electrons of a formula unit of MgO* onto an empty (100) terrace. The voltage U^{dis} associated with the step (Eq. 3-14) is very low, only 0.70 V. Subsequently, steps 2 through 7 represent reactions at low-coordinated sites such as islands, steps, kinks, *etc*. These steps all exhibit larger voltages (i.e., liberate more energy during discharge) than the initial reaction. That the initial deposition of MgO is the potential determining step can be understood based on simple bond counting: deposition onto a flat terrace presents the geometry with the fewest available neighbors for bonding.

For recharge, the potential determining step is the initial dissolution of a single formula unit of MgO* from the (100) terrace, corresponding to reaction coordinate 8 to 7 in Figure 7. This

reaction results in the formation of a vacancy or pit on an otherwise pristine terrace. The formation of this feature is energetically costly because dissolution from a filled terrace layer requires the most bonds to be broken. This step has a large limiting potential of $U^{chg} = 4.45$ V (Eq. 3-15). Subsequent reaction steps – coordinates 7 through 2 – correspond to the dissolution of MgO* at low-coordinated sites. These steps occur at much lower applied voltages.

Combining the calculated limiting potentials with the theoretical cell voltage, Eq. 3-17, yields large overvoltages for both discharge and charge: $\eta^{discharge} = 2.25$ V and $\eta^{charge} = 1.50$. Consequently, the voltaic efficiency for this pathway, defined as U^{dis}/U^{chg}, is very low, only 16%. A summary of the calculated limiting potentials, overvoltages, and efficiencies for the MgO (100) single-step pathway is given in Table 3.2.

3.3.3.3   MgO (100) Multi-Step Reaction

The blue line in Figure 7 depicts the free energy profile for the multi-step reaction pathway given by Eq. 3-12a-b. In this pathway two reaction steps are required to reduce oxygen to a nominal charge state of 2-. The first step corresponds to the deposition of MgO_2*. This is followed by the deposition of $(Mg^{2+} + 2e^-)$*, which further reduces the two oxygen atoms to the oxidation state of bulk MgO. This sequence is then repeated 3 more times, until a full monolayer is deposited.

The multi-step pathway is slightly more efficient than the single-step pathway: It increases the limiting discharge potential from 0.70 V to $U^{dis} = 1.15$ V, and reduces the limiting charge potential from 4.45 V to $U^{chg} = 3.98$ V. The increase (decrease) in discharge (charging) potential indicates that it is thermodynamically more favorable for oxygen to be reduced (oxidized) via a pathway that involves the multi-step reduction (oxidation) of oxygen, with MgO_2* as an intermediate. Consequently, the multi-step mechanism increases the voltaic efficiency to 29%.

Similarly, the thermodynamic overvoltages for discharge and charge are nearly 0.5 V smaller than for the single-step mechanism: $\eta^{discharge} = 1.80$ V and $\eta^{charge} = 1.03$.

Shiga *et al.*[11,12] reported a Mg/O$_2$ battery with a discharge voltage of approximately 1.1-1.2 V. Assuming an MgO discharge product, this voltage is in good agreement with the limiting potential calculated for the multi-step pathway, $U^{dis} = 1.15$ V. Similarly, their attempts to recharge the cell[11,12] revealed that the discharge product did not decompose at potentials as large as the oxidative stability limit of electrolyte (~3.2 V). This is also consistent with the limiting potential calculated for the multi-step pathway, which suggests that a minimum voltage of ~4 V is needed to initiate the oxygen evolution reaction.

Table 3.2. Calculated limiting potentials, thermodynamic overvoltages, and efficiencies associated with various discharge and charging reactions in an Mg/O$_2$ cell. Values in regular text refer to terrace-site reactions; values in parentheses refer to non-terrace reactions, which are limiting only for the superoxide-terminated surfaces, Orich-1 and Orich-3.

Discharge product, surface, and reaction mechanism	Limiting Potential (V)		Overvoltage (V)		Voltaic Efficiency (%)
	Discharge	Charge	Discharge	Charge	
MgO (100) Stoi [Single-step]	0.70	4.45	2.25	1.50	16
MgO (100) Stoi [Multi-step]	1.15	3.98	1.80	1.03	29
MgO$_2$ (100) Stoi [Single-step]	0.92	4.69	2.02	1.75	20
MgO$_2$ (100) Stoi [Multi-step]	1.31	4.04	1.63	1.10	33
MgO$_2$ (111) Orich-1 [Single-step]	2.76 (2.61)	3.01 (3.25)	0.18 (0.33)	0.07 (0.31)	92 (80)
MgO$_2$ (100) Orich-3 [Single-step]	2.83 (2.63)	3.27 (3.29)	0.11 (0.31)	0.33 (0.35)	87 (80)
Li$_2$O$_2$ (Ref. 37)			0.35, 0.68	0.20, 0.40	

3.3.3.4 MgO$_2$ (100) Stoichiometric Surface

Given that the formation energies of MgO and MgO$_2$ are very similar, it is conceivable that an Mg/O$_2$ cell could discharge to MgO$_2$ rather than to MgO. Discharge mechanisms that form MgO$_2$

may also exhibit faster kinetics than those leading to MgO, as the former does not require the disassociation of O_2. To examine whether such a pathway would be beneficial from the standpoint of thermodynamics, the limiting potentials on the stoichiometric MgO_2 (100) surface were evaluated. As done for the MgO calculations described above, a 2×2 expansion of the primitive surface cell was adopted. In this geometry each surface layer contains 8 formula units of MgO_2; a "complete" discharge reaction therefore consists of the consecutive adsorption of 8 additional formula units.

Two reaction pathways were considered; these include: (*i.*) a "single step" pathway wherein a full MgO_2 formula unit is created at each elementary step:

$$\left(Mg^{2+}+2e^{-}\right)+O_2 + * \rightleftharpoons MgO_2^*$$

(3-18)
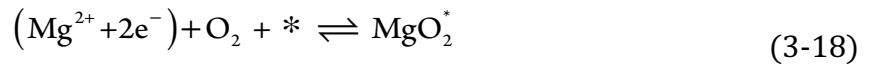
and, (*ii.*) a multi-step pathway where the initial deposition of an intermediate magnesium superoxide $Mg(O_2)_2^*$ unit is followed by the deposition of $(Mg^{2+} + 2e^{-})^*$. This pathway generates two formula units of MgO_2^* for every pair of 2 e- transfers:

$$\left(Mg^{2+}+2e^{-}\right)+2O_2 + * \rightleftharpoons Mg(O_2)_2^*$$

(3-19a)

$$Mg(O_2)_2^* + \left(Mg^{2+}+2e^{-}\right) \rightleftharpoons 2MgO_2^*$$

(3-19b)
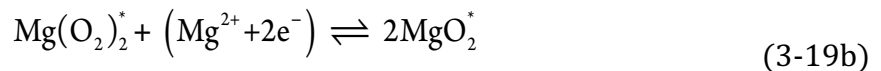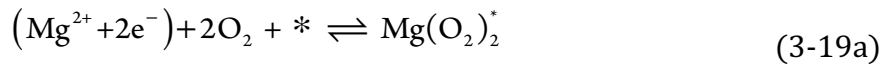
Reactions 19a-b are repeated until the surface has grown by one formula-unit layer.

The black line in Figure 8 depicts the free energy profile for the single-step reaction pathway, Eq. 3-18. The same methodology and bias potential (i.e., $U = U_0$, where U_0 reflects the theoretical voltage associated with formation of bulk MgO_2) described previously was used. As seen for the MgO pathways, the potential determining step for discharge (charge) corresponds to the deposition (dissolution) of a formula unit on (from) a flat terrace. The calculated discharge voltage is low, $U^{dis} = 0.92$ V. Similarly, the voltage needed for charging is high, $U^{chg} = 4.69$ V.

The large difference in discharge/charge voltages results in a poor voltaic efficiency of 20% (Table 3.2).

The blue line in Figure 8 depicts the free energy profile for the multi-step reaction pathway, Eq. 3-19a-b. Similar to the pathways discussed previously, the potential determining step for discharge is from step 1 to 2, corresponding to the deposition of $(Mg^{2+}+2e^-)^*$ near the previously deposited $Mg(O_2)_2{}^*$ species on an otherwise empty terrace. For charge, the potential is determined by the dissolution of $Mg(O_2)_2{}^*$ corresponding to step 7 to 6. The multi-step reaction increases the discharge voltage to $U^{dis} = 1.31$ V and reduces the charging voltage to $U^{chg} = 4.04$ V. These voltages correspond to an approximately 0.4-0.6 V improvement over the single–step pathway, and are reflected in an increase in the efficiency from 20% to 33%, Table 3.2. The trend of higher efficiency for the multi-step pathway on the MgO_2 (100) surface mimics what was observed previously on MgO (100). The similarity of these results suggest that reaction pathways involving intermediate charge states may in general be more efficient for ORR and OER in metal/oxygen batteries.[57,70,71,86]

3.3.3.5 MgO$_2$ Superoxide-Terminated Surface

Our discussion has thus far focused on reactions occurring on stoichiometric surfaces. We now shift attention to pathways on the oxygen-rich (111) 'Orich-1' and (100) 'Orich-3' surfaces, which are expected to appear on the surfaces of MgO_2 crystallites (Table 3.1, Figure 3.4), as they are the most stable terminations overall. As previously described, these surfaces contain superoxide moieties on the surface layer. Reaction energies for the Orich-1 surface were evaluated using a 2×1 expansion of the primitive surface cell. In this geometry each surface layer contains 8 formula units of MgO_2.

The reaction pathway for discharge/charge on the Orich-1 surface is shown in Figure 3.8 for the single-step mechanism of Eq. 3-18. The calculated limiting potentials on this surface are significantly closer to the theoretical cell voltage than for any of the foregoing systems: $U^{dis} =$ 2.61 V and $U^{chg} = 3.25$ V, Table 2. These potentials occur at reaction step 4→5 for discharge and at step 6→5 for charging. Indeed, this reaction pathway is nearly ideal, as suggested by its approximately flat profile in Figure 3.8 (cf. black dashed line in Figure 6). These potentials yield a round-trip efficiency of 80%.
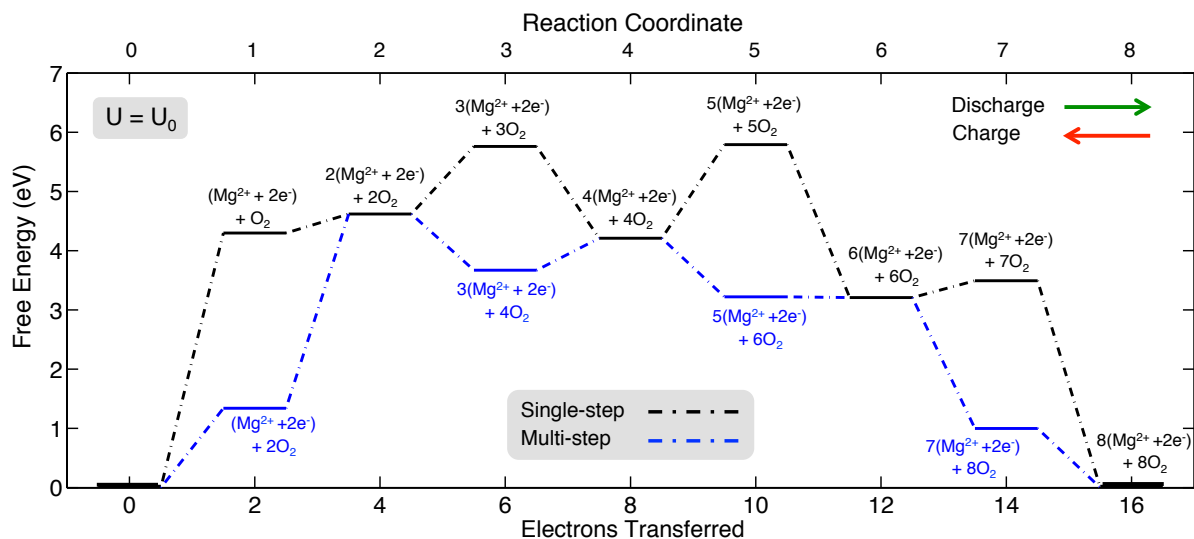
Figure 3.7. Calculated free energy diagram for discharge and charging of an Mg/O_2 cell, assuming that all reactions occur on the stoichiometric MgO_2 (100) surface. Black lines refer to the single step pathway, Eq. 18; blue lines refer to the multi-step pathway, Eqns. 19a-b. Energies are plotted assuming the application of a potential, U, equal to the theoretical cell potential, $U = U_0$.

The limiting potentials for pathways on the stoichiometric MgO and MgO_2 surfaces discussed earlier largely arise from terrace-based reactions. Due to their high concentration, terrace sites likely comprise the majority of sites accessed at the high current densities required for automotive applications.[56,59] Restricting our analysis of the Orich-1 surface only to terrace-site

reactions results in a further reduction in overvoltages [0.18 (0.07) V for discharge (charge), Table 3-2], and a correspondingly higher efficiency of 92%.

Reaction energies on the (100) Orich-3 superoxide surface were also evaluated using the single-step mechanism of Eq. 3-18, and are shown in Figure 3-8. Similar to the Orich-1 surface, the calculated limiting potentials are close to the theoretical cell voltage: $U^{dis} = 2.63$ V and $U^{chg} = 3.29$ V, resulting in a high round-trip efficiency of 80%. The limiting potential for discharge occurs from step 2→3, while the limiting potential for charge occurs from step 7→6. Restricting the analysis to terrace sites, we find that discharge is expected at a slightly higher potential, $U^{dis} = 2.83$ V, while the charging potential is mostly unchanged, $U^{chg} = 3.27$ V. These potentials yield a slightly higher round-trip efficiency of 87%, with low overvoltages of 0.11 and 0.33 V, Table 3.2.

3.4   Discussion

We note that the favorable electrochemistry on both of the superoxide-terminated surfaces occurs for a single-step reaction mechanism, Eq. 3-18. This may seem counter-intuitive given that our earlier calculations on the stoichiometric surfaces of MgO and MgO_2 suggested that intermediate-containing pathways (Eq. 3-12 and 3-19, respectively) exhibit more favorable thermodynamics than single-step pathways. In fact, the superoxide surfaces appear to be a special case of this rule, which emerges from the distinct nature of their surface charge state relative to the bulk. In support of this hypothesis we recall that oxygen dimers in the bulk regions of these slabs exhibit a peroxide-like charge state, as determined by a Bader charge and bond-length analysis; on the other hand, the surface dimers exist in a superoxide-like state. Analysis of changes to the charge state of the slab before and after an elementary discharge step reveal that the 2e- transferred according to Eq. 3-18 are split between an existing surface O_2, reducing it into a peroxide, and the newly-adsorbed O_2, which is a superoxide. Thus, the net amount of bulk peroxide increases, while maintaining the

superoxide surface layer. In contrast to the multi-step reactions (Eq. 3-12 & 3-19), where a separate step is devoted to the formation of a (less-reduced) intermediate species, here the less-reduced superoxide surface moieties can be considered as a permanently-present intermediate species. In other words, the slab's superoxide surface layer serves as a "built-in" intermediate.
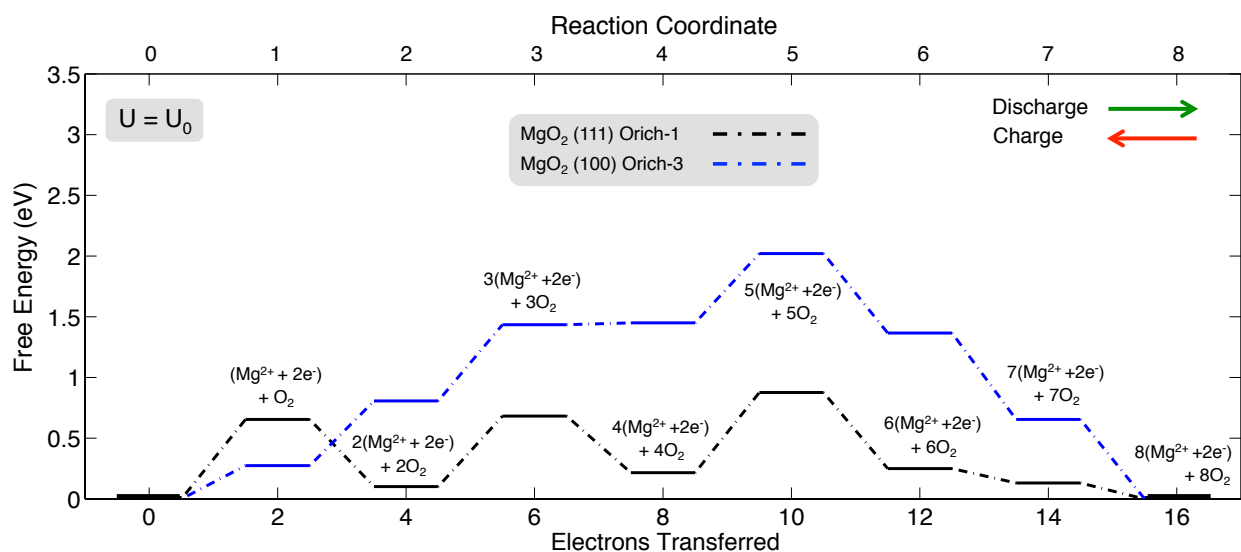
Figure 3.8. Calculated free energy diagram for discharge and charging of an Mg/O_2 cell, for single-step reactions (Eq. 18) occurring on the oxygen rich MgO_2 (111) 'Orich-1' (black curve) and MgO_2 (100) 'Orich-3' (blue curve) surfaces. Energies are plotted assuming the application of a potential, U, equal to the theoretical cell potential, $U = U_0$. (Note that the maximum value for the ordinate (3.5 eV) used in this plot is half the value used in Figs. 3.6 & 3.7.)

Our calculations suggest that discharge/charge reactions are much more efficient when they occur on the superoxide-terminated, oxygen-rich surfaces of MgO_2 than when they occur on stoichiometric surfaces, regardless of whether the latter belong to an oxide (MgO) or peroxide (MgO_2) discharge product. Recent experiments on Mg/O_2 batteries support this assertion: high overpotentials were observed in MgO-based cells,[11,12] whereas lower overpotentials and higher rechargeability were reported for a cell having a mixed MgO/MgO_2 discharge product.[13]

For the superoxide-terminated surfaces overvoltages are approximately 0.3 V or smaller, while for stoichiometric surfaces values in excess of 1 V are typical. This trend is consistent with

the behavior of metal oxygen batteries that discharge to superoxides, such as those based on potassium[87] and sodium anodes.[46,88] These superoxide-based cells exhibit much lower overvoltages than those that discharge to a peroxide.[88,89] It has been suggested[46,87] that the greater reversibility of the superoxide systems can be traced to more efficient reduction and oxidation of oxygen. In superoxide-based cells these processes occur via a single electron transfer ($O_2+Na^++1e^-\leftrightarrow NaO_2$), whereas two electrons must be exchanged for a peroxide product ($O_2+2Na^++2e^-\leftrightarrow Na_2O_2$). These experimental observations, in combination with the present calculations, suggest that the precipitation/dissolution of superoxide-based discharge products – be they stoichiometric superoxides, or superoxide-terminated peroxides – should be intrinsically more efficient than the cycling of stoichiometric peroxide- or oxide-based discharge products.

As previously mentioned, our calculations find that intermediate-containing reaction pathways are favored as they generally maximize discharge voltages and lower charging voltages. This observation is consistent with the thermodynamic theory of multi-electron transfer reactions. As described by Koper,[82] and based on Marcus theory, the simultaneous transfer of two electrons – which could in principle occur during the reduction of oxygen upon formation of an MgO discharge product – requires an activation energy which is four times larger than that needed for a single electron transfer. Consequently, a series of sequential, single electron transfers is expected to present a more energetically favorable pathway for such a reaction. The latter mechanism can be realized by temporarily "storing" charge from the first single electron transfer in an intermediate species, such as MgO_2, wherein oxygen is less reduced than in the final MgO product. A second single electron transfer subsequently converts MgO_2 to MgO. A similar pathway is proposed for cells that discharge to MgO_2, except that magnesium superoxide, $Mg(O_2)_2$, now serves as the intermediate.

It should be noted that the preceding description is based on kinetics, while the present study is based solely on a thermodynamic analysis of reaction energies. A link between thermodynamics and kinetics is provided by the Brønsted-Evans-Polanyi relationship,[90] which correlates the *energy of reaction* with the *activation energy* for that reaction. Hence, our (thermodynamic) observation that reaction pathways containing less-reduced intermediate species are favored is consistent with the system avoiding pathways that exhibit high activation energies that can arise from unfavorable simultaneous multi-electron transfers. Several studies have noted the presence or importance of intermediate species in reactions occurring in metal-oxygen batteries,[70,86] or in other contexts. [78,81,83,84]

Finally, it is instructive to compare the present results for an Mg/O_2 cell to studies on the Li/O_2 system.[54–56,85,91] A recent report by Viswanathan *et al.*[56] calculated overvoltages for terrace site reactions on the Li_2O_2 discharge product of 0.35 & 0.68 V for discharge, and 0.2 & 0.4 V for charging, Table 3.2. These values are slightly larger than the overvoltages calculated here for the oxygen-rich surfaces of MgO_2, which range from 0.11 to 0.18 V for discharge and 0.07 to 0.33 V for charging. Based on thermodynamics alone, this implies that an Mg/O_2 cell that discharges to MgO_2 could be more efficient than a Li/O_2 cell.

3.5   Conclusions

A rechargeable battery based on an Mg/O_2 couple presents an attractive chemistry due to its high theoretical energy density and potential for low cost. Nevertheless, few experimental studies of this system exist, and in all cases these studies report performance that is far from the ideal: high overpotentials and limited cycleability are commonly observed in Mg/O_2 cells. In addition, many fundamental aspects of this system remain poorly understood, such as the reaction mechanisms

associated with discharge and charge. Lacking this understanding, improvements to Mg/O$_2$ batteries will be limited to approaches based on trial-and-error.

To accelerate the development of Mg/O$_2$ batteries, the present study employs Density Functional Theory calculations to characterize discharge/charge mechanisms on the surfaces of plausible Mg/O$_2$ battery discharge products, MgO and MgO$_2$. These compounds have similar formation energies, and recent experiments have shown that both can be present following discharge of an Mg/O$_2$ cell.[13] Thermodynamic limiting potentials for charge and discharge were calculated for several scenarios, including variations in surface stoichiometry and the presence/absence of intermediate species in the reaction pathway.

Based on these calculations we conclude that: (*i.*) Reaction pathways that include (less-reduced) oxygen intermediates are more efficient than those that do not. These intermediate-containing pathways generally maximize discharge voltages and lower charging voltages. This conclusion is consistent with the thermodynamic theory of multi-electron transfer reactions.[82] (*ii.*) Due to the presence of large thermodynamic overvoltages, cells that discharge to MgO are expected to exhibit intrinsically poor performance. The calculated discharge/charge voltages of 1.15/~4.0 V are consistent with recent experiments,[11,12] which show that MgO-based cells exhibit low round-trip efficiencies. (*iii.*) In contrast, MgO$_2$-based cells are predicted to be much more efficient: the superoxide-terminated facets of MgO$_2$ crystallites allow for high discharge/low charging voltages, resulting in round-trip efficiencies approaching 90%. The possibility for improved performance in MgO$_2$-based cells is supported by a recent experiment which observed higher discharge voltages in a cell having a mixed MgO/MgO$_2$ discharge product.[13]

In turn, these observations suggest the following design directions for Mg/O$_2$ batteries: (*i.*) Maximum energy density can theoretically be achieved with a cell that reversibly cycles MgO.

However, surface-mediated reactions on MgO are shown by the present calculations to be highly inefficient, and should be avoided. Consequently, for an MgO-based cell to be viable a liquid-phase reaction pathway, likely in combination with a redox mediator, is preferred. Whether this pathway can be realized at high current densities – where many metal/O_2 systems transition to a surface-mediated mechanism/film-like morphology – remains an open question. (*ii.*) An alternative strategy is to bias the discharge so as to produce MgO_2 rather than MgO. As described above, surface-mediated reactions on the former compound are suggested by our calculations to be much more efficient than those on the latter. Increasing the oxygen pressure and/or reducing the temperature of the cell during operation could achieve such an outcome. The relative stability of MgO_2 *vs.* MgO could also be tuned by varying the composition of the electrolyte or the cathode support. Additional study is needed to examine the effectiveness of these strategies.

Chapter 4

Intrinsic Conductivity in Magnesium-Oxygen Battery Discharge Products

4.1 Introduction

Due to the nearly identical formation energies of magnesium oxide, $\Delta G_f^0(MgO) = -568.9$ kJ/mol,[44] and magnesium peroxide, $\Delta G_f^0(MgO_2) = -567.8$ kJ/mol,[92] both compounds may be expected to participate in the cycling of non-aqueous Mg/O_2 cells. By analogy with Li-air cells that reversibly cycle Li_2O_2, these MgO_x compounds could appear as a solid discharge product within the cathode during discharge, and subsequently decompose during charging, according to

$$Mg^{2+} + 2e^- + \frac{1}{2}O_2 \rightleftharpoons MgO, \ \ U_0 = 2.95 \text{ V} \tag{4-1}$$

$$Mg^{2+} + 2e^- + O_2 \rightleftharpoons MgO_2, \ \ U_0 = 2.94 \text{ V}. \tag{4-2}$$
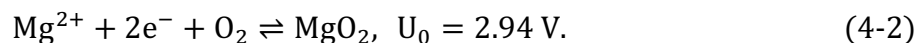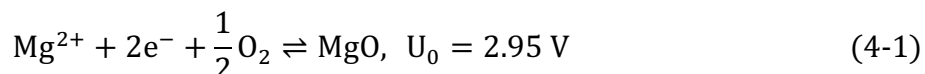
Mg/O_2 batteries using non-aqueous electrolytes have recently been reported.[11–13,93] In the experiments performed by Shiga *et al.* it was concluded that the discharge product was MgO; furthermore, it was demonstrated that MgO was not rechargeable at moderate voltages unless a redox mediator was present.[11,12] In a later study employing a different electrolyte, Vardar *et al.* found the discharge product to comprise a mixture of MgO and MgO_2, with the peroxide component exhibiting more facile decomposition during recharge.[13] In agreement with these experimental observations, *ab initio* calculations of the theoretical limiting voltage in Mg/O_2

batteries predicted low voltaic efficiency (~30%) for cells that cycle MgO. In contrast, cells that discharge to MgO_2 were predicted to achieve much higher efficiencies, up to approximately 90%.[92]

To realize high energy densities it is desirable to maximize the quantity of the MgO_x discharge product formed within the cathode (i.e., maximize discharge capacity). Unfortunately, maximizing capacity is likely at odds with achieving efficient battery operation, as "sudden death" and high charging voltages in analogous Li/O_2 batteries have both been attributed to the insulating nature of the discharge product.[1,39,94–100] In these systems lithium peroxide (Li_2O_2) forms on the cathode during discharge, impeding charge migration from the cathode support to the electrolyte/Li_2O_2 interface. One may speculate that sluggish charge transport through the discharge product is a universal limitation that must be circumvented to cycle any metal-oxygen battery at high capacity, regardless of the anode composition. These considerations suggest that understanding transport mechanisms in metal-oxygen compounds – including oxides, peroxides, and superoxides – is a prerequisite for the rational design of efficient metal-air batteries.

In the case of MgO, most experimental measurements of transport have been conducted at temperatures exceeding 1000 K.[101–112] Of course, for battery applications it is the low-temperature conductivity that is most relevant. The paucity of measurements near room temperature is presumably due to difficulties associated with measuring the (very low) conductivity of nominally-insulating MgO. These measurements are further compounded by the presence of impurities, variations in sample preparation, and sensitivity to the temperature history of the sample, the latter being indicative of a failure to achieve equilibrium at low temperatures.[103,104]

Despite these complications, clear trends in the experimental data for MgO have emerged. Most notable amongst these is the observation of three distinct "Arrhenius branches" associated with the conductivity as a function of temperature.[113] The conductivity is conventionally described

in terms of the Arrhenius energy, W, according to the expression $\sigma = \sigma_0 \exp(-W/k_B T)$. Here W is the sum $(E_f + E_b)$ of the formation and migration energies of a particular charge carrier. Unusually, the conductivity data for MgO exhibits three distinct W values of approximately 2.4, 1, and 0.2 eV.[101,103,104,113] These differing values suggest the transport mechanism in MgO varies as a function of temperature. Although speculation regarding the different mechanisms has been offered,[104,113–115] little direct evidence exists.

Transport in MgO has also been studied using a variety of computational methods. These studies typically focus on intrinsic ionic (point) defects such as vacancy-interstitial pairs (i.e., Frenkel defects) or vacancies involving both cations and anions (i.e., Schottky defects). Early calculations from Catlow[116] and Mackrodt[117,118] using model potentials found that the formation energies were large for both Schottky (~7 eV) and Frenkel (~12−15 eV) defects, precluding any sizeable concentration. Subsequent studies[119–129] have reaffirmed these high formation energies using more sophisticated methods that range from first-principles DFT[122,127–129] to quantum Monte Carlo.[125] In contrast to the large number of studies on Schottky and Frenkel defects in MgO, little effort has been devoted to characterizing electronic carriers such as polarons.

Although a large number of studies have been conducted on MgO, charge transport in alkaline earth peroxides such as MgO_2 is essentially unexplored. This also differs from the situation for alkali metal peroxides and superoxides, such as Li_2O_2, sodium peroxide (Na_2O_2), and sodium superoxide (NaO_2),[94,95,130–139] for which a number of studies have recently appeared. In the case of Li_2O_2, experiments and calculations agree on the identity of the charge carriers as negative Li vacancies and positive hole polarons, although there is some discrepancy in the magnitude of the conductivity.[95,134] Calculations on these compounds predict low electronic conductivities in the range of approximately 10^{-20} to 10^{-19} S/cm.[95,138] Likewise, ionic conductivity was also predicted

to be low in the peroxides – 10^{-19} S/cm in Li_2O_2 and Na_2O_2 – and several orders of magnitude higher, 10^{-10} S/cm, for the superoxide NaO_2.[95,138] Regarding experiments, the electrical conductivity of Li_2O_2 at 100 °C was measured at 10^{-12} to 10^{-11} S/cm.[134] Measurements on the alkali-metal superoxides (KO_2, RbO_2, and CsO_2) reported values in the same range as for Li_2O_2.[139] The difference between theory and experiment can arise from the presence of impurities or from non-equilibrium defect concentrations.[140–142] The latter effect results in higher-than-expected concentrations at low temperatures, due to the freeze-in of defects upon cooling of the sample.[141] To put these values in context, the electrical conductivity of common Li-ion cathode materials fall in the range of 10^{-5} to 10^{-9} S/cm.[143]

In the present Chapter *ab initio* calculations at the hybrid level of theory and beyond (GW method) are employed to identify the concentrations and mobilities of intrinsic (point) defects in MgO and MgO_2. In so doing, we shed light on potential performance limitations in Mg/O_2 batteries arising from sluggish transport through these phases. In addition, a comparison between our calculations and the experimental literature allow us to clarify the elusive conduction mechanisms associated with the three Arrhenius branches observed for MgO. Formation energies and concentrations are calculated for several varieties of vacancies, interstitials, and polarons. Subsequently, the mobility of the dominant (i.e., highest-concentration) defects are calculated with the nudged elastic band method.[144–146] The resulting conductivity data are compared to that of the discharge products of other metal-oxygen systems, namely Li/O_2 and Na/O_2.

Many-body perturbation theory calculations performed at the GW level of theory reveal MgO and MgO_2 to be insulators with large bandgaps approaching 8 eV. For MgO we find the dominant point defects to be hole polarons localized on the oxygen sub-lattice, and negative Mg vacancies (V_{Mg}^{2-}) with a formal charge of -2 The formation energy for both defects is high, 2.2 eV,

indicative of low concentrations. The calculated mobility of V_{Mg}^{2-}, 4×10^{-38} cm^2/Vs, is very low, but in excellent agreement with experimental data, 1.5×10^{-37} cm^2/Vs.[111] In contrast, the mobility of hole polarons is much higher, 6×10^{-3} cm^2/Vs. In the case of MgO$_2$, electronic charge carriers alone – electron and hole polarons – are the most prevalent. Similar to MgO, the absolute concentration of carriers in MgO$_2$ is low, and moderate-to-poor mobility further limits conductivity.

Our calculations indicate that at room temperature the equilibrium conductivity for both MgO and MgO$_2$ is low (~10^{-36} S/cm), even when compared to that of other insulating metal/O$_2$ discharge products such as Li$_2$O$_2$ and NaO$_2$. Consequently, sluggish charge transport will limit the performance of Mg/O$_2$ batteries by restricting the effective thicknesses, and thus the amount of discharge product formed (i.e., capacity), during discharge. Nevertheless, the observation of moderate-to-high mobility for hole polarons in both compounds suggests a strategy for improving battery performance: artificially enhancing the hole polaron concentration via introduction of monovalent dopants.

4.2 Methodology

Defect formation energy and mobility calculations were performed using the Vienna *ab initio* simulation package (VASP code).[60–63] Blochl's projector augmented wave (PAW) method[65] was used to treat core-valence electron interactions, with valence states of 3*s* adopted for magnesium and 2*s*2*p* for oxygen. Many-body perturbation theory (GW method) was used to predict the bandgap of MgO and MgO$_2$.[147,148] The screened hybrid functional expressed with the formulation of Heyd-Scuseria-Ernzerhof (HSE)[149,150] was used with the fraction of exact exchange tuned (α = 0.42) to reproduce the bandgap from GW calculations. Finite-size energy corrections for charged systems were included *via* the Makov-Payne method.[151,152] The dielectric constants of MgO and

MgO_2 were calculated using density functional perturbation theory;[153] values of 10.7 and 6.8 were obtained, respectively. The calculated value for MgO is in good agreement with the experimental dielectric constant, which falls in the range of 9 to 10.[115] To our knowledge the dielectric constant of MgO_2 has not been reported.

For calculations involving conventional (bulk) unit cells the Brillouin zone was sampled with a Gamma-centered k-point mesh of density $4 \times 4 \times 4$ for oxides/peroxides, and $16 \times 16 \times 16$ for Mg. Conventional cells were expanded into a $2 \times 2 \times 2$ supercell for defect and mobility calculations on MgO and MgO_2. In these cases k-point sampling was performed only at the Gamma point. The plane-wave cutoff energy was set to 400 eV; all atoms positions were relaxed until the forces were less than 0.04 eV/Å. The convergence criterion for electronic self-consistency was set to 10^{-6} eV. All calculations were spin polarized to account for the un-paired electron configurations preferred by some defects.

The formation energy, E_f, of a point defect X in charge state q was calculated according to the following equation:

$$E_f(X^q) = E(X^q) - E_0 - \sum_i n_i \mu_i + q\varepsilon_f + E_{MPI} \qquad (4\text{-}3)$$

Here E_0 represents the energy of a defect-free cell, n_i and μ_i denote the number and chemical potential of a species i that has been added to or removed from the cell in the course of creating the defect, ε_f is the Fermi level (referenced to the valence band maximum), and E_{MPI} is the Makov-Payne correction for charged systems.[151,152] Composite defects comprising more than a single point defect can also be studied with this formalism. For example, the formation energy of a Schottky defect can be evaluated by taking the sum of the energies required to form a stoichiometric defect involving vacancies on both cation and anion sites. Similarly, a Frenkel defect is evaluated as the sum of formation energies for a vacancy and an interstitial.

The chemical potential of magnesium was determined using the calculated energy, g of MgO$_x$ (x = 1, 2) and the chemical potential of oxygen gas (μ_{O2}), $\mu_{Mg} = g_{MgOx} - (x/2)\mu_{O_2}$. Following earlier studies, corrections based on the experimental formation enthalpies were applied to both compounds to account for the combined effects of overbinding within O$_2$ gas and for oxidation state errors in the solid phase.[92,154]

The equilibrium concentration c of a defect can be expressed as $c = N\exp(-E_f/k_B T)$, where N is the number of (symmetry-equivalent) available defect sites per unit volume, k_B is the Boltzmann constant, and T is the absolute temperature.[155] The mobility of a defect, defined as μ, is expressed as:[156]

$$\mu = \frac{vqa^2}{k_B T}\exp(-E_b/k_B T),$$

(4-4)

where v is the attempt frequency (10^{13} s^{-1}) for migration,[157] q is the charge on the defect, a is the distance between neighboring defect sites, and E_b is the migration barrier. The total conductivity is expressed as a sum of the product of concentration and mobility contributions from all charge carriers i:

$$\sigma = \sum |q_i| c_i \mu_i.$$

(4-5)

4.3   Results and Discussion

4.3.1   Lattice Geometry

MgO adopts the rocksalt structure with an experimental lattice constant of a = 4.21 Å.[67] Vannerburg reported that MgO$_2$ crystallizes in the cubic pyrite structure with a lattice constant of a = 4.84 Å.[47] These crystal structures are illustrated in Figure 4.1. Our calculations employing the PBE-GGA functional result in a slight over-prediction of the lattice constants: 4.24 Å for MgO

and 4.88 Å for MgO_2.[92] On the other hand, the HSE06 functional slightly under-predicts the lattice constants: 4.19 Å and 4.78 Å, respectively. Consequently, we adopted the experimental lattice constants, which fall between our GGA and HSE values, for subsequent GW and defect calculations.[158]
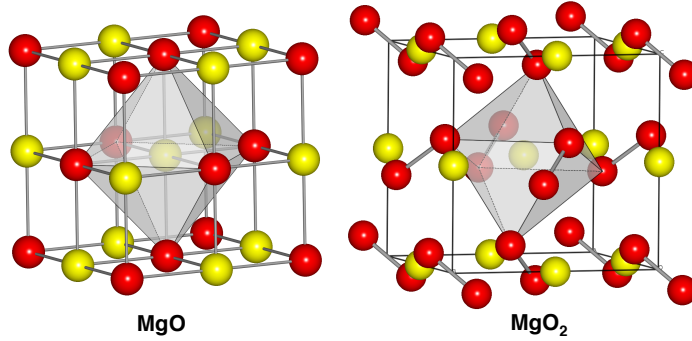
Figure 4.1. Crystal structure of MgO and MgO_2. Magnesium ions are octahedrally coordinated by oxygen ions in MgO, and by oxygen dimers in MgO_2. Red spheres represent oxygen atoms, yellow spheres are magnesium, and the oxygen octahedron is shown in gray.

4.3.2   Bandgaps

The bandgaps of MgO and MgO_2 were calculated using five different levels of theory: GGA, $HSE\alpha$, non-self-consistent GW (G_0W_0), partially self-consistent GW (GW_0), and self-consistent GW (GW) methods. The GW-based methods used the GGA wavefunctions as input. The calculated bandgaps are summarized in Table 4.1. The GW_0 method has been shown to best describe the band gap of semiconductors and insulators.[158] Our calculated GW_0 value of 7.5 eV for MgO closely matches that of an earlier GW study (7.7 eV),[158] as well as the experimental band gap of ~7.8 eV.[159] Our calculations indicate that MgO has a direct band gap at Γ, while MgO_2 has an indirect band gap. All levels of theory except the GGA predict a slightly larger bandgap for MgO_2 compared to MgO. Based on the GW calculations, the HSE functional was tuned to reproduce the bandgaps by mixing a fraction ($\alpha = 0.42$) of exact exchange with semi-local exchange, resulting in HSE_α bandgaps of 7.8 eV and 7.9 eV for MgO and MgO_2, respectively.

Table 4.1. Calculated band gap for MgO and MgO_2 from different levels of theory. Experimental optical band gaps of MgO.[159,160]

	Bandgap (eV)					
	GGA	HSEα	GGA+ G_0W_0	GGA+ GW_0	GW	Expt.
MgO	4.5	7.8	7.1	7.5	8.2	7.4, 7.69 7.7, 7.8
MgO (Ref. [158])	–	–	7.3	7.7	8.5	–
MgO_2	3.9	7.9	7.5	8.2	9.1	–

4.3.3 Defect Concentrations

Figure 4.2 shows the formation energies of 51 intrinsic defects evaluated as a function of the Fermi level for MgO and MgO_2. Five distinct charge states (-2, -1, 0, +1, and +2) were considered, with specific defect types including magnesium vacancies (blue lines), magnesium interstitials (blue dashed lines), oxygen vacancies (red lines), oxygen interstitials (red dashed lines), and di-oxygen vacancies (green lines); hole and electron polarons are shown in black. The slope of each line corresponds to charge state of that defect.

The vertical dashed line in Figure 4.2 indicates the position of the Fermi level. Under equilibrium conditions the Fermi level is set by the condition of charge neutrality, $\sum q_i c_i = 0$. This condition places the Fermi level somewhat below the center of the band gap, or 2.48 eV above the valence band maximum (VBM) for MgO and 2.69 eV above the VBM for MgO_2.

Figure 4.2a shows the formation energies for intrinsic defects in MgO. The defects having the lowest formation energies are the hole polaron (p^+) and magnesium vacancy (V_{Mg}^{2-}). The formation energies for these defects is high, 2.23 eV, resulting in low equilibrium concentrations for both defects of approximately 1×10^{-15} cm^{-3}. For comparison, this is many orders of magnitude less than the intrinsic carrier concentration of silicon ($\sim 10^{10}$ cm^{-3}),[161] and for Li_2O_2 and Na_2O_2

$(\sim 10^7$ cm^{-3}).[95,138] The defect with the next-lowest formation energy is the neutral oxygen interstitial at 2.3 eV.
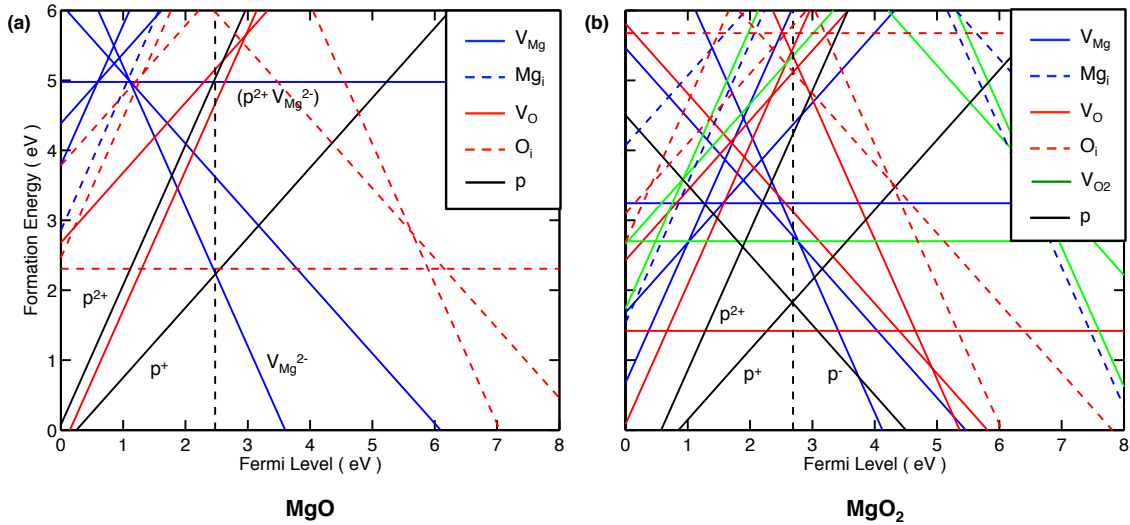
Figure 4.2. Formation energies of intrinsic defects in (a) MgO and (b) MgO$_2$ calculated using the HSEα functional. Magnesium vacancies (V$_{Mg}$) are depicted using blue lines, magnesium interstitials (Mg$_i$) with blue dashed lines, oxygen vacancies (V$_O$) with red lines, oxygen interstitials (O$_i$) red dashed lines, and oxygen di-vacancies (V$_{O2}$) with green lines. Hole and electron polarons are shown in black. The slope of each line corresponds to its respective charge state; values of -2, -1, 0, +1, and +2 were considered. The dashed line indicates the position of the Fermi level.

A polaron consists of a localized charge (electron or hole) and an induced local lattice distortion (i.e., polarization) in the crystal. In MgO O^{2-} anions are octahedrally coordinated by Mg^{2+} cations with an oxygen-Mg distance of 2.1 Å. The absence of one electron on an oxygen site results in the formation of a hole polaron (p$^+$). The resulting oxygen ion has an electronic configuration of 2s^{2}2p^5, a formal charge O^{1-}, and hosts an unpaired electron.

The magnetization density of MgO in the vicinity of a hole polaron is illustrated in Figure 4.3a. The density isosurface has a shape consistent with that of an oxygen 2p-orbital, and is aligned along the direction where the Mg ions are furthest from the hole (d = 2.25 Å). The oxygen-Mg distance along the other two directions is elongated to a smaller degree, d = 2.18 Å, but is still larger than the bulk Mg-O nearest-neighbor distance (2.1 Å). The general elongation of these

bonds relative to bulk is consistent with a weaker electrostatic interaction between the Mg^{2+} sublattice and the less-negatively-charged O^{1-} (resulting from the presence of p^+). We note that the hole polaron forms only from a starting configuration wherein the symmetry of the MgO crystal is broken along one of the O-Mg bond directions. Without this distortion, the charge density relaxes to a local minimum in which the hole is delocalized. The stabilization energy for p^+, defined as the energy difference between the localized and delocalized state, is -0.24 eV. Although hole polarons can be localized on oxygen sites in MgO, we were unable to localize electrons on Mg cations.
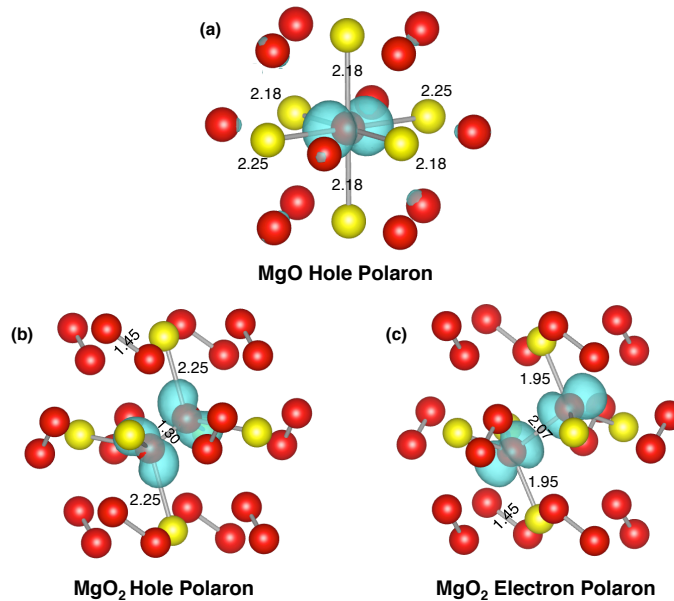
Figure 4.3. Magnetization density for (a) hole polaron in MgO, (b) hole polaron in MgO_2, and (c) electron polaron in MgO_2. The iso-surface is plotted at 0.01 $e/Å^3$. The numbers in the figure indicate bond length in Å. The oxygen to Mg bond distance in bulk is 2.1 Å for both MgO and MgO_2.

Our prediction that doubly negative Mg vacancies, V_{Mg}^{2-}, and holes, p^+, comprise the dominant defects in MgO is consistent with experiments.[113–115,162] For example, magnetic susceptibility measurements indicate the presence of paramagnetic species in MgO,[114] a feature which could be explained by a non-zero concentration of p^+. Also, abrupt changes in the magnetic

properties, charge distribution, and conductivity in MgO with respect to temperature were attributed to holes localized on the oxygen sub-lattice that are formed upon dissociation of a so-called "peroxy defect."[162] This composite defect is comprised of a peroxide ion (O_2^{2-}) and V_{Mg}^{2-}, and is therefore neutral and non-magnetic. Its formation energy is shown in Figure 4.2a as (p^{2+} V_{Mg}^{2-}).

Other defects of relevance in MgO include Schottky (a vacancy pair on anion and cation sublattices) and Frenkel (a vacancy-interstitial pair) defects, which are often present in ionic materials;[156] the formation energies of these composite defects are summarized in Table 4.2. Cation and anion Frenkel defects have a calculated formation energy of 10.1 and 13.8 eV, respectively, similar in magnitude to the result obtained by Mackrodt[118] (11.9 and 15.2 eV) using interatomic potentials. Regarding Schottky defects, experimental measurements of the formation energy range from 5 to 7 eV.[163] Table 2 shows our calculated Schottky defect formation energy, 6.91 eV, and compares with prior calculations and experiments. Our value falls near the middle of the range of calculated values,[116,117,126–129,118–125] which span 5.1 to 8.8 eV. A recent study[121] compared the calculated Schottky defect formation energies in MgO, as evaluated using the LDA, GGA, Hartree Fock theory, and many electron perturbation theory. They concluded that the formation energy was within the range of 6.9 to 7.22 eV, in good agreement with our value. To our knowledge the present calculations are the first to employ a tuned hybrid functional (HSEα) to evaluate defect formation energies in MgO.

Figure 4.2b shows the formation energies of intrinsic defects in MgO_2. The defect with the lowest formation energy overall is the neutral oxygen vacancy. However, since this is a neutral species a contribution to charge transport is not expected. The dominant charged defects are hole (p^+) and electron polarons (p^-). The formation energies of both defects is 1.82 eV, and their

concentrations are 6×10^{-9} cm^{-3}. The prediction that both charged defects in MgO$_2$ are electronic in nature (rather than ionic) differs from the behavior of Li- and Na-peroxide, where the lowest-energy carriers are hole polarons and negatively charged vacancies on the metal sublattice. In contrast to these other peroxides, the formation energy of a Mg cation vacancy in MgO$_2$ (assuming it is charge-compensated by a hole polaron) is high, 2.18 eV. An additional feature distinguishing MgO$_2$ from the alkali-metal peroxides is its relatively high formation energies: the most populous carriers in MgO$_2$ have formation energies (1.82 eV) that are approximately double those reported for Na$_2$O$_2$ and Li$_2$O$_2$.[95,138]

Table 4.2. Formation energies and migration barriers for various defects in MgO and MgO$_2$. Schottky and Frenkel defects are comprised of a pair of point defects; their formation energies are reported on a per pair basis. Experimental data appears in brackets.

	Formation Energy (E_f)				Migration Barrier (E_b)	
	Schottky	Cation Frenkel	Anion Frenkel	Selected Point Defects	Polaron	V_{Mg}^{2-}
MgO (This study)	6.91	10.05	13.8	2.23 (V_{Mg}^{2-} or p$^+$)	0.11 (p$^+$)	2.20
MgO (Prior studies)	7.5-7.9[a], 7.5[b], 7.72[c], 8.2[d], 6.88[e], 7.53[f], 8.44[g], 7.5[h], 6.0[i], 8.8[j], 5.79[k], 5.05[l], 7.22[m] [5-7[163]]	11.9[b], 12.43[c], 13.35[g], 14.1[h], 10.3[j], 14.1[j], 10.41[l]	15.2[b], 12.33[c], 13.81[g], 13.57[i], 12.2[j], 13.6[j], 13.32[l]	–	–	1.9-2.2[a], 2.16[b], 2.07[c], 1.93[f], 2.08[g], 2.10[k], [2.28[111]]
MgO$_2$ (This study)	8.33	9.78	$^\delta$10.24, $^\Delta$12.16	1.82 (p$^+$ or p$^-$)	0.56 (p$^+$), 1.76 (p$^-$)	–

[a]Catlow *et al.* (1976)[116]
[b]Mackrodt *et al.* (1979)[118]
[c]Sangster *et al.* (1981)[119]
[d]Grimes *et al.* (1990)[120]

[e]De Vita *et al.* (1992)[122]
[f]Vocadlo *et al.* (1995)[123]
[g]Busker et al. (2000)[124]
[h]Alfe et al. (2005)[125]

[i]Uberuaga et. (2005)[126]
[j]Gilbert *et al.* (2007)[127]
[k]Runevall *et al.* (2011)[128]
[l]Mulroue *et al.*(2011)[129]

[m]Grunies (2015)[121]

$^\delta \left(V_O^+, O_I^- \right)$, $^\Delta \left(V_O^{2+}, O_I^{2-} \right)$

In MgO$_2$, oxygen dimers have a formal charge of 2−, i.e., O$_2^{2-}$, and are octahedrally coordinated by Mg^{2+} ions. The hole and electron polarons are localized on these dimers. p+ is formed by removing an electron from the dimer, resulting a half-filled π^* molecular orbital with superoxide-like character. This orbital is illustrated using magnetization density isosurfaces in

Figure 4.3b. The shortened O-O bond distance of 1.3 Å in the presence of p^+ is consistent with the bond length in magnesium superoxide.[48] In addition, the neighboring Mg ions closest to the p^+ slightly increase their distance to the dimer to 2.25 Å. All bond lengths beyond the nearest neighbor bonds are similar to those in bulk MgO_2, 2.1 Å. The stabilization energy for p^+, is -0.84 eV.

The electron polaron is formed by adding an electron to O_2^{2-}, resulting in a half-filled σ^* molecular orbital with a single, unpaired electron. The shape of the magnetization density for p^-, shown in Figure 4.3c, also reflects this orbital topology. The presence of p^- increases the O-O bond length significantly, to 2.1 Å, compared to 1.45 Å in the bulk. Similarly, formation of p^- contracts the Mg-O nearest-neighbor bond distance from 2.1 to 1.95 Å. The stabilization energy for p^-, is -3.4 eV.

Regarding other defect types in MgO_2, the formation energies for Schottky and Frenkel defects are displayed in Table 2. For Schottky defects, the anion is defined as the oxygen dimer (i.e. O_2^{2-}) resulting in a vacancy pair of (V_{Mg}^{2-}, V_{O2}^{2+}). The formation energy of Frenkel defects involving cations was evaluated as the sum of a V_{Mg}^{2-} and Mg_I^{2+}. Two types of anion Frenkel defects were considered: (V_O^+, O_I^-) and (V_O^{2+}, O_I^{2-}). As shown in Table 4.2, all of these defects have similar formation energies (~8−12 eV) to the analogous defects in MgO. The extremely high formation energies of all Schottky and Frenkel defects considered suggest that they will not be present in meaningful concentrations, nor will they contribute significantly to charge transport.

4.3.4 Electronic Structure.

The density of states (DOS) for defect-free (pristine) MgO and MgO_2 are shown in Figures 4e and 4f, respectively. In both cases the DOS reflects the large bandgap of approximately 8 eV predicted by our GW calculations. Also, both compounds exhibit a valence band comprised of oxygen 2p

states. The conduction band character differs, however, with MgO exhibiting primarily Mg-based

states, while in MgO₂ the conduction band is comprised of σ* orbitals on the peroxide units.
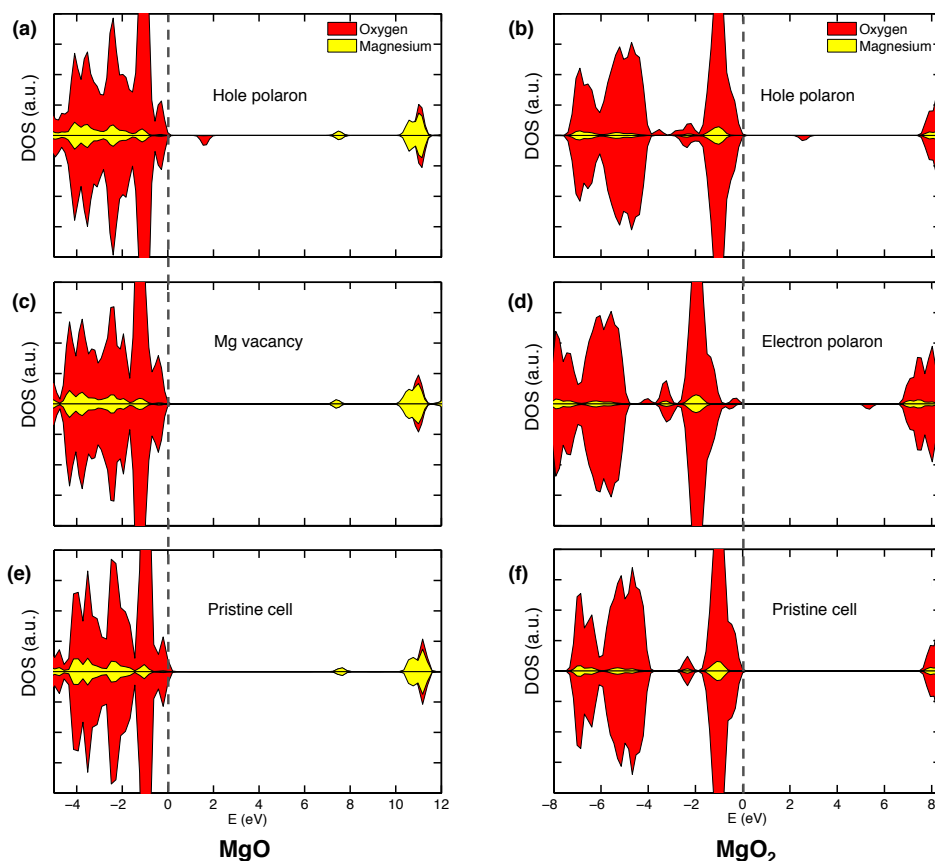
Figure 4.4. Density of states (DOS) calculated with the HSEα functional (α = 0.42). [Left panel] (a) Hole polaron, (c) magnesium vacancy, and (e) pristine cell in MgO. [Right panel] (b) Hole polaron, (d) electron polaron, and (f) pristine cell in MgO₂. The states above the mid-point horizontal axis are spin up, and the states below are spin down. The energies are given with respect to the top of the valence band.

Our discussion has thus far has used changes in bond lengths and magnetization densities

to support the presence of polarons in MgO and MgO₂. Additional evidence can be seen in the

DOS. The hole polaron in MgO (Figure 4.4a) and in MgO₂ (Figure 4.4b) introduces localized

oxygen 2p states in the gap closest to the valence band maximum (VBM). These empty states

emerge from the VBM upon removal of electrons from the oxygen π* orbital during hole creation.

Similarly, the electron polaron in MgO₂ (Figure 4.4d) introduces new 2p states near the conduction

band minimum, and also slightly alters the DOS just below the VBM. For comparison, the negative magnesium vacancy (V_{Mg}^{2-}) in MgO is shown in Figure 4.4c. In this case the DOS is mostly unchanged, indicating that the extraction of a Mg^{2+} cation has relatively minor impact on the electronic structure.

4.3.5 Mobility and Conductivity

The migration barriers for the highest concentration defects in MgO and MgO_2 were calculated using the nudged elastic band (NEB) method.[144–146] Both compounds possess high-symmetry (i.e., isotropic) cubic crystal structures with only one symmetry-distinct pathway for defect migration between neighboring sites. As previously mentioned, in MgO the two dominant defects are the hole polaron (p^+) and the negative Mg vacancy, V_{Mg}^{2-}. The calculated minimum energy pathway for migration of V_{Mg}^{2-} is shown in Figure 5c. This process is characterized by a high migration barrier, 2.2 eV, resulting in a low mobility of 4×10^{-38} cm^2/Vs at room temperature. The diffusion coefficient of V_{Mg}^{2-} is determined using the Nernst-Einstein equation, $D = \mu k_{B} T/q$, yielding a value of 1×10^{-39} cm^2/s, shown in Table 3. Previous computational studies of V_{Mg}^{2-} migration have reported similar activation energies in the range of 1.9 to 2.2 eV. [116,118,123,124,128,164] These values are summarized in Table 2 and agree well with the present hybrid-functional-based calculations. Our calculated activation energy and mobility for V_{Mg}^{2-} is also in good agreement with experimental measurements of Sempolinski and Kingery,[111] who reported an activation energy of 2.28 ± 0.2 eV and a mobility of 1.5×10^{-37} cm^2/Vs at room temperature.
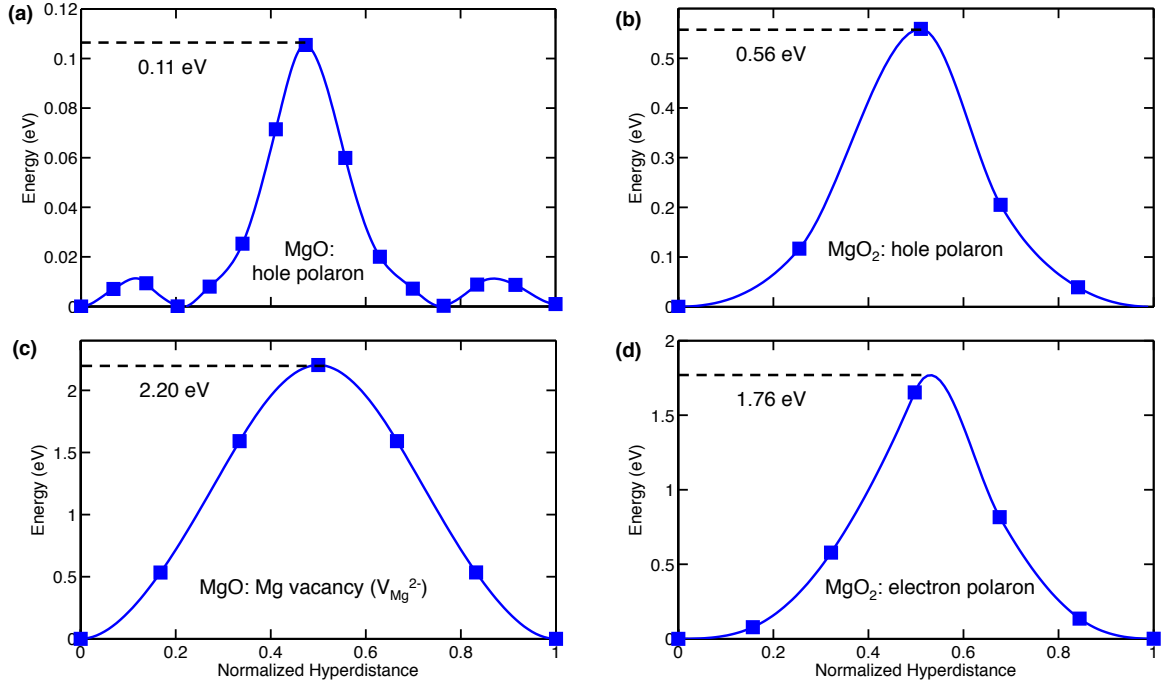
Figure 4.5. Migration energy barriers of dominant defects calculated using the NEB method. (a) hole polaron and (c) magnesium vacancy (V_{Mg}^{2-}) of MgO. (b) hole polaron of MgO_2 and (d) electron polaron of MgO_2.

In contrast to the low mobility of V_{Mg}^{2-}, hole polaron migration in MgO is relatively fast. Figure 4.5a plots the minimum energy pathway for p^+ migration, revealing a low barrier of 0.11 eV. Consequently, a moderately high mobility of 6.0×10^{-3} cm^2/V·s is predicted, along with a diffusion coefficient of 1.5×10^{-4} cm^2/s. For comparison, the mobility of holes in p-type silicon in the high doping regime is approximately 50 cm^2/V·s.[165] We are not aware of any prior calculations or measurements of polaron mobility in MgO.

In MgO_2 our calculations predict that the dominant defects are both electronic in nature: hole (p^+) and electron (p^-) polarons. The calculated migration barriers for these carriers are shown in Figure 4.5b and 5d, and demonstrate that the barrier for the migration of electron polarons is roughly three times higher (1.76 eV) than that for hole polarons, 0.56 eV. These barriers result in mobilities of 6×10^{-31} and 1×10^{-10} cm^2/V·s, respectively. To place these values in context, in

Li$_2$O$_2$ Radin *et al.*[95] reported in-plane and out-of-plane migration barriers for p$^+$ of 0.42 and 0.71 eV, respectively, using the HSEα functional. Garcia-Lastra *et al.*[94] found comparable barriers for p$^+$ of 0.39 and 0.48 eV using GGA+U. In contrast, much larger barriers were reported for migration of p$^-$: 1.41 and 1.47 eV. Additionally, the migration barrier for hole polaron hopping in Na$_2$O$_2$ was reported as 0.47 eV (in plane) and 0.62 eV (out-of-plane).[138] Taken together, these data suggest that in peroxides hole polarons are generally much more mobile than electron polarons, with the former exhibiting hopping barriers that are similar (~ 0.5 eV) regardless of peroxide composition, and approximately one third the size of p-.

Mobilities, diffusion coefficients, and conductivity data for MgO and MgO$_2$ are summarized in Table 4.3, along with data from the literature for other alkali metal peroxides and superoxides. Under equilibrium conditions, the conductivity arising from the migration of charged point defects is the product of the carrier's charge, concentration, and mobility (Equation 4-5). At room temperature our calculations suggest extremely low conductivities for MgO and MgO$_2$ of 3×10^{-36} and 3×10^{-37} S/cm, respectively. The similar conductivity of these compounds reflects a tradeoff between the mobility and the concentration of the dominant carriers in these phases. In MgO hole polarons are the dominant carriers; the p$^+$ have high mobility but very low equilibrium concentrations. In MgO$_2$ this trend is reversed: p+ remain the dominant carriers, but their mobility is now lower than in MgO, yet their concentrations are proportionally higher, resulting in approximately equal conductivities.

As mentioned in the Introduction, it is non-trivial to achieve an "apples-to-apples" comparison between the calculated and measured conductivity in nominally-insulating compounds at ambient temperatures. These difficulties can be traced to the presence of impurities in the sample and/or the freeze-in of non-equilibrium defect concentrations characteristic of the elevated

temperatures at which the sample was prepared or conditioned.[166,167] Contributions from the sample's microstructure may also be important. All of these effects are ignored in typical single-crystal calculations.

Table 4.3. Calculated diffusion coefficient, mobility, and conductivity of dominant defects in MgO and MgO$_2$. Data from literature for Li$_2$O$_2$, Na$_2$O$_2$, and NaO$_2$ are included for comparison.[95,138]

Compound	Diffusion coefficient D (cm^2/s)	Mobility $\mu \, (cm^2/Vs)$	Conductivity $\sigma \, (S/cm)$
MgO (p$^+$)	1×10^{-4}	6×10^{-3}	3×10^{-36}
MgO (V$_{Mg}^{2-}$)	1×10^{-39}	4×10^{-38}	1×10^{-71}
MgO$_2$ (p$^+$)	4×10^{-12}	1×10^{-10}	3×10^{-37}
MgO$_2$ (p$^-$)	2×10^{-32}	6×10^{-31}	7×10^{-58}
Li$_2$O$_2$ (p$^+$)	9×10^{-10}	~	5×10^{-20}
Na$_2$O$_2$ (p$^+$)	~	~	1×10^{-20}
NaO$_2$ (p$^-$)	~	~	1×10^{-19}
NaO$_2$ (V$_{O2}^+$)	6×10^{-7}	~	4×10^{-9}

Literature reports have confirmed difficulties in achieving reproducible conductivity values in MgO near room temperature (RT).[101,104] These difficulties are presumably tied to the slow equilibration of charge-carrying defects.[156,166,167] For other oxides, equilibrium is typically achieved above 400−800°C.[140] Consequently, it is not unexpected that the measured RT conductivity of MgO of ~10^{-9} S/cm[101] is significantly larger than our calculated equilibrium value of 10^{-36} S/cm. We postulate that this discrepancy is an artifact of comparing a *non-equilibrium* measurement with an *equilibrium* calculation. As described below, this explanation is bolstered by the good agreement between experiments and calculations at high temperatures, where both systems are in equilibrium.

In the case of MgO$_2$, it appears that conductivity measurements have not been reported. Nevertheless, we expect trends similar to those discussed above for MgO to hold for MgO$_2$, such

as a measured (non-equilibrium) conductivity that is larger than that predicted by calculations at RT.

Of course, in a practical battery RT operation is preferred. The preceding discussion suggests that an equilibrium carrier concentration is unlikely to be achieved at this temperature. Consequently, our calculated RT conductivities should be interpreted as a lower bound to the behavior likely present in an electrochemical cell. In a realistic Mg/O_2 cell there exist two additional, potentially significant contributions to the non-equilibrium nature of the carrier concentration. The first is the rapid growth of the MgO/MgO_2 product during battery discharge. Fast discharge/growth rates should result in substantially higher defect concentrations. Second, as the growth of the discharge product occurs in an (impure) liquid electrolyte, impurities from the electrolyte may be incorporated into this product.

These two effects suggest two strategies for improving Mg/O_2 battery performance. First, since discharging at a higher rate improves the conductivity of the discharge product, performance could in principle be improved by employing pack designs that employ a larger number of reduced-capacity cells. (In these cells the effective discharge rate will be higher.) This assumes other losses due to higher-rate operation can be neglected.

A potentially more promising strategy exploits the incorporation of species from the electrolyte into the discharge product during growth. By intentionally doping the discharge product one may increase the carrier concentration. This could be achieved by substitution of aliovalent dopants on Mg sites. For example, substitution with monovalent impurities such as Lithium[168,169] may increase the concentration of hole polarons, which our calculations predict are relatively mobile in both MgO and MgO_2. Assuming one polaron is created for each monovalent dopant, then a doping concentration of 10^{12} cm^{-3} (10^{19} cm^{-3}) would be needed to achieve a conductivity of

10^{-9} S/cm in MgO (MgO$_2$). A similar strategy has been proposed to improve the performance of Li/O$_2$ batteries.[98]

4.3.6 Explanation for the Three Arrhenius Branches in the Temperature-History-Dependent Conductivity of MgO

Measurements of the conductivity of solids such as MgO are conventionally presented as Arrhenius plots of the log of conductivity (log σ) *vs.* inverse temperature (1/*T*). The slope of the Arrhenius plot is interpreted as the "Arrhenius energy," *W*, which is the sum of the carrier migration barrier, E_b, as well as the carrier's formation energy, E_f ($W = E_b + E_f$):

$$\sigma = \sigma_0 \exp(-W/k_B T). \qquad (4\text{-}6)$$

Most experimental studies of conductivity in MgO focus on high temperatures above approximately 1000 K.[101,102,112,104–111] Data in this region, summarized in Figure 6, are in broad agreement that the Arrhenius energy is approximately 2.4 eV. Studies below 1000 K[101,104] noted that the conductivity was dependent on the temperature history of the sample; reproducible data could only be obtained during cooling after the sample was conditioned via heat treatment. At these low-to-moderate temperatures two other "Arrhenius branches" in the MgO conductivity data have been reported (Figure 4.6). These include a branch with a very low Arrhenius energy in the range of 0.15 to 0.25 eV,[101,104] and a higher-energy branch with W = 1.0 eV.[104] Although mechanisms responsible for these branches have been proposed, direct evidence linking the measured Arrhenius energies with the identities of specific charge carriers and their respective migration mechanisms does not exist. Below we propose transport mechanisms responsible for all three Arrhenius branches using the catalogue of formation and migration energies evaluated in the present study. Before doing so, we describe the concept of 'frozen in' defects in oxides.

As previously mentioned, the dearth of low-temperature conductivity data in MgO can presumably be attributed to difficulties achieving equilibrium at low temperatures. In practice, equilibrium within the crystal, and between the crystal and surrounding atmosphere, can be reliably obtained only at high temperatures.[166] This is because equilibrium concentrations of ionic defects are established via the transport of ions over potentially long distances, and this transport is often possible only at high temperatures. For example, the creation of a vacancy in the bulk region of a crystallite requires mass transport of ions to a 'sink' such as a surface, internal void, dislocation, or grain boundary. As a crystal cools from the temperature of preparation or from an intentional heat treatment, ionic defects quickly become less mobile and the time to achieve equilibrium increases. Consequently, defect concentrations representative of equilibrium at higher temperatures become 'frozen in' with respect to the time scale over which low-temperature measurements are performed. Below these temperatures it is commonly assumed that processes involving mass transport (i.e., ion migration) are likely to be frozen (i.e., non-equilibrated), while electronic processes such as electron transfer remain equilibrated.[156,166,170]

As described in Table 2, our calculations predict that the predominant charge carriers in MgO are (doubly) negative Mg vacancies, V_{Mg}^{2-}, and hole polarons, p^+. These carriers have identical formation energies of 2.23 eV, but dramatically different activation energies for migration, E_b, of 2.20 and 0.11 eV, respectively. As shown by Equation 6, the conductivity will be dominated by the carrier having the smallest Arrhenius energy, W. For an MgO crystallite in equilibrium, our calculations predict W values of 4.43 eV for V_{Mg}^{2-} and 2.34 eV for p^+. If equilibrium is not attained, for example, due to rapid cooling resulting in a frozen-in concentration of carriers, then the formation energy contribution to the Arrhenius energy can be neglected. In this case only carrier mobilities contribute to the Arrhenius energy, i.e., $W \approx E_b$.
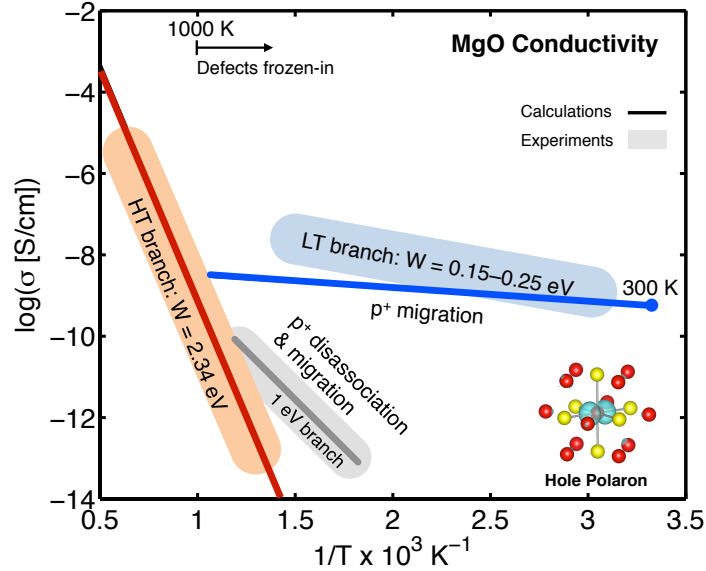
Figure 4.6. Arrhenius plot of the conductivity of MgO, illustrating the three Arrhenius Branches reported in experiments: (red) high temperature (HT) branch, (blue) low temperature (LT) branch, and (grey) 1 eV branch.

The conductivity of MgO at high temperatures predicted using the present calculations is shown in Figure 6 with a red line. This data is compared to experimental measurements in the same temperature range, whose spread is depicted using an orange oval.[101,102,104–106,109] The agreement between the calculations and measurements is very good. At these high temperatures, we expect that thermal equilibrium is achieved for both p^+ and V_{Mg}^{2-}. (The calculated diffusivity for V_{Mg}^{2-}, the slower-diffusing of the two species, indicates that vacancies can traverse distances of approximately 1 μm at 1000 K over a 24-hour period. This distance should be sufficient to establish equilibrium concentrations under these conditions, as diffusing ions would be capable of reaching ion sinks.) Furthermore, the experimental Arrhenius energy, W=2.4 eV, is in remarkable agreement with the calculated value, W = 2.34 eV, assuming a hole-polaron-dominated conduction mechanism. These data indicate that the mechanism responsible for high temperature conductivity in MgO is the formation and migration of p^+. In contrast, the large Arrhenius energy (W = 4.43

eV) for ionic conductivity due to V_{Mg}^{2-} implies that vacancies have a negligible contribution to conductivity in this temperature range.

The range of experimental data[101,104] for the so-called low-temperature conductivity branch is shown in Figure 6 using a blue oval. These data were obtained by heating the sample to approximately 1000 K, and recording the conductivity during cooling. The Arrhenius energy was reported to fall in the range of 0.15 to 0.25 eV. This branch can be rationalized by assuming that the concentration of charge carriers is frozen-in during the time over which measurements were performed. The presence of frozen-in defects has been noted in other oxides as well.[140,141]

To calculate a conductivity in the low-temperature regime it is necessary to adopt a value for the (non-equilibrium) carrier concentration. Given the low temperature, hole polarons, which possess a very low migration barrier of 0. 11 eV, are expected to be the only mobile carriers. We assume the concentration of p^+ to be frozen-in at a value equal to their calculated equilibrium concentration (6.2×10^{11} cm^{-3}) at 1000 K. This concentration is consistent with experimental measurements[104] that suggest the freezing-in temperature for defects in MgO is near 1000 K. (Samples annealed at room temperature exhibited a continuous decrease in their conductivity, consistent with a decrease in carrier concentration, as equilibrium was slowly approached.)[103,113]

The calculated conductivity of the low-temperature (LT) branch is plotted in Figure 6 using a blue line. These calculations adopt the frozen concentration of p^+ (at 1000 K) and employ the calculated migration energy. Good agreement is obtained between the calculated and measured (blue oval) data. This agreement reflects the similar values for the Arrhenius energies – 0.11 eV calculated vs. 0.15 to 0.25 eV measured – and suggests that the conduction mechanism underlying the LT branch is p^+ migration alone.

A third Arrhenius branch in the MgO conductivity data is obtained when heating of the sample is interrupted at approximately 800 K.[103,104] In this case an Arrhenius energy of 1.0 eV was reported. This branch is shown as a grey band in Figure 4.6, and can be reproduced using a heating and cooling routine where the temperature is progressively raised.[104] This phenomena, along with anomalies in magnetic susceptibility and charge distribution data, were argued by Batllo and co-workers[114] to arise from the disassociation of holes bound to doubly negative Mg vacancies. These hole-vacancy complexes are created by the incorporation of trace H_2O during crystal growth, and are thus of extrinsic origin.[114] The holes were postulated to be localized on the oxygen sublattice, which would make them very similar to the small hole polarons identified in the present study. Taken together, these observations suggest that the conduction mechanism in the 1 eV branch is the dissociative formation, and subsequent migration, of p^+.

To test this hypothesis we calculated the disassociation energy of a single p^+ bound within a $2p^+$- V_{Mg}^{2-} complex: [113]

$$\left(p^{2+} V_{Mg}^{2-}\right)^x \rightleftharpoons \left(p^+ V_{Mg}^{2-}\right)^- + p^+. \tag{4-7}$$

Reaction 7 may be followed by the dissociation of the remaining p^+, per:

$$\left(p^+ V_{Mg}^{2-}\right)^- \rightleftharpoons V_{Mg}^{2-} + p^+. \tag{4-8}$$

The calculated p^+ disassociation energies (Eq. 7 & 8) are similar, 0.87 and 0.85 eV, respectively. Taking these dissociation energies as an effective formation energy, and combining them with the polaron migration energy, we derive a calculated Arrhenius energy of 0.97 eV. This value is in remarkable agreement with the measured value of 1.0 eV, resulting in the similar slopes for the calculated (grey line) and measured (grey oval) data shown in Figure 4.6. This observation supports the hypothesis that the 1 eV branch is due to the liberation and migration of p+ bound to

negative vacancies. (Because the carriers in this branch are extrinsic in origin and their concentration is not well-established, the calculated Arrhenius branch in Figure 6 has been positioned (vertically) using the measured conductivity.[104] Therefore, the most meaningful comparison between theory and experiment in this branch is the Arrhenius energy)

4.4 Conclusions

This chapter has presented a comprehensive analysis of charge transport mechanisms within the primary discharge products, MgO and MgO_2, of an Mg/O_2 battery. While these batteries have extremely high theoretical energy densities, their benefits have yet to be realized in a practical cell that is both reversible and long-lived. Understanding transport within the nominally-insulating discharge phases is an important step towards overcoming these performance gaps.

In the case of MgO, our calculations identify doubly negative Mg vacancies and hole polarons as the dominant charge carriers. For MgO_2, electronic charge carriers alone – electron and hole polarons – are the most prevalent. Due to the large formation energies associated with defects in both compounds, the equilibrium concentration of charge carriers is predicted to be low at the near-ambient temperatures expected for battery operation. These low concentrations also offset the moderate (for MgO_2) to high (in MgO) mobility of hole polarons. Consequently, if *equilibrium* carrier concentrations are realized, the conductivity for both MgO and MgO_2 will be low, and thus likely limit battery performance.

Nevertheless, charge transport within the discharge products of a realistic battery cathode will be strongly influenced by *non-equilibrium* effects. These effects arise from fast growth rates during discharge, impurity incorporation from the electrolyte, and limited ion mobility at ambient temperatures. In combination with the moderate/high mobilities predicted for hole polarons, these non-equilibrium effects suggest a strategy for improving conductivity: artificially increasing

polaron concentrations *via* the incorporation of monovalent impurities into the discharge product during its growth. In principle, this could be achieved through the intentional addition of small quantities of lithium ions to the electrolyte.

Finally, the calculated conductivity data for MgO are observed to be in remarkable agreement with the three Arrhenius branches reported in experiments, and thus clarify the long-debated transport mechanisms within these regimes.

.

Chapter 5

Cooperative Ion Migration in Li-ion Conducting Glasses

5.1 Introduction

Inorganic solid electrolytes (SEs) offer the potential for improved safety and higher energy density compared to conventional Li-ion batteries.[4,24,171] The lithium thiophosphate family has reemerged as a promising candidate for use as a 'solid solution' solid electrolyte due to its favorable conductivity and formability. However, understanding ionic transport processes in amorphous materials has lagged behind that of crystals. Fundamental to diffusion in crystalline ionic conductors is the idea of lattice disorder put forth by Frenkel and Schottky. Migration in these systems relies on the availability of lattice sites being unoccupied (a vacancy) or ions occupying an interstice between normal lattice sites (an interstital). The probability for a transition between these sites is exponentially proportional to the potential energy differences associated with the formation and migration of these defects.[17] In highly disordered materials such as glasses, these fundamental ideas are mostly absent since no long-range order exists; the energy landscape is influenced by variations in local coordination and can be dynamically heterogeneous.[172–174] Moreover, in many SEs the concentration of ions is high ($\sim 10^{22}$ cm^{-3}) due to interparticle separations of only a few atomic radii. Consequently, the influence of cooperative (or correlated) ion-ion dynamics on the diffusion process can be significant. Given these circumstances, the

validity of the general theory of ionic transport in crystalline phases often does not apply.[175] Correlation effects ought to be considered for a more complete understanding of transport.

Some of the earliest molecular dynamic (MD) studies of binary Lennard-Jones supercooled glass-forming liquids recognized particle motion to be highly cooperative;[176–179] further studies support the premise.[180–185] In 1966, to interpret deviations in the Einstein relation for silver sulfide, Yokota proposed the 'caterpillar mechanism' where two or more ions cooperatively jump.[186] In 1973, a class of diffusion mechanisms was introduced for crystalline SEs with polyatomic anions: there, cation motion was coupled to the rotational motion of the anions via a so-called 'paddle-wheel mechanism'.[187]

More recently classical and *ab initio* MD studies of crystalline lithium ion conducting SEs have suggested that diffusion is a cooperative process. For example, the high conductivity of *c*-$Li_7La_3Zr_2O_{12}$ has been attributed to the collective motion of Li-ions.[188–190] Xu *et al.* observed 'string-like' lithium migration in crystalline $Li_{10}GeP_2S_{12}$.[191] He *et al.* found migration energy barriers consistent with experiment when concerted motion was considered versus single ion hopping.[192] In polyborane SEs, anion reorientation and thermal librations were shown to create a local driving force for cation diffusion.[193,194] We are not aware of any cooperative motion studies on LPS glasses.

In the present chapter *ab initio* molecular dynamics (MD) are employed to study the structure and dynamics of glassy-Li_3PS_4. Different from the largely static role played by anions in crystalline materials, we find lithium to be dynamically coupled to the reorientation and thermal vibrations of PS_4 anions. Moreover, lithium migration events involve the nearly simultaneous migration of adjacent lithium. This dynamic coupling is expected to contribute to the fast ion conducting nature of lithium thiophosphate solid solution electrolytes.

5.2 Computational Details

First-principles calculations were performed with the Vienna *ab initio* simulation package (VASP).[61–63] Core-valence electron interactions were treated with the projector augmented-wave method.[65,195] The generalized gradient approximation in the formulation of Perdew-Burke-Ernzerhof was used for exchange and correlation.[64] The computational cell consisted of lithium and ortho-thiophosphate ions (PS_4^{3-}). A Monte Carlo annealing procedure employing a classical interatomic potential was used to generate the initial disordered atomic structure[196,197] comprising of sixty lithium (Li^+) and twenty PS_4^{3-} ions at a density of 1.9 g cm^{-3} within a computational cell having periodic boundary conditions. Starting from the Monte Carlo-generated structure, DFT geometry optimization calculations and *ab initio* melt-and-quench molecular dynamics were used to generate a plausible structure for glassy-Li_3PS_4. Parrinello-Rahman dynamics[31,198] with variable cell shape and volume (NPT ensemble) were employed in combination with a Langevin thermostat.[32] The plane-wave energy cutoff energy was set to 400 eV to minimize Pulay stresses. The friction coefficients of atomic species and lattice was 10 ps^{-1}. The lattice mass was set to 1000 amu. The MD time step was 2 femto-seconds. A Gamma-only *k*-point mesh was used. Melt-and-quench MD involved an initial equilibration at 300 K for 3 pico-seconds (ps), heating to 1000 K at 70 K/ps, a 3 ps hold at 1000K, cooling to the desired temperature at the same 70K/ps rate, and, finally, equilibration for an additional 3 ps at the target temperature.

5.3 Results and Discussion

5.3.1 Structure

Figure 5.1shows the structure of glassy Li_3PS_4 predicted by *ab initio* molecular dynamics at T = 300 K. The resulting density was 1.56 g cm^{-3}; for comparison, the experimental density of crystalline γ- Li_3PS_4[199] is 1.93 g cm^{-3}. PS_4 tetrahedra comprise the anionic components of the

computed glass structure at 300 K; at this temperature no other complex anion types (such as P_2S_6 and P_2S_7) were observed.[200]
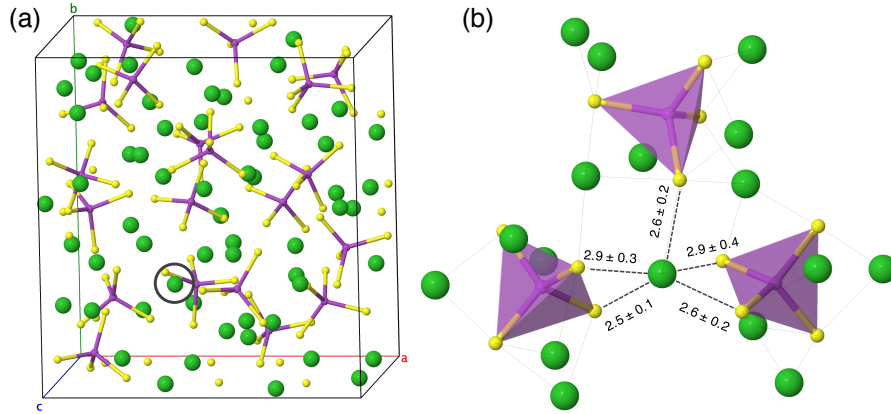
Figure 5.1. Computed structure of glassy Li_3PS_4 at 300 K generated from melt-and-quench *ab initio* MD. Green spheres represent lithium atoms, phosphorus is magenta, and sulfur is yellow. (a) Computational cell. A representative Li-ion is identified with a blue circle. The local structure of this ion is magnified in (b), where numbers indicate the mean and standard deviation of nearest-neighbor S distances (Å).

The static structure of the computed LPS model was characterized using three techniques: (*i.*) the partial pair distribution function (p-PDF), $g(r)_{\alpha\beta}$, (*ii.*) the coordination number, $n(r)_{\alpha\beta}$, and, (*iii.*) the total neutron weighted PDF, G'(r). The p-PDF $g(r)_{\alpha\beta}$ is a commonly-used measure of the local structure of glasses and liquids. It is defined as:

$$g(r)_{\alpha\beta} = \frac{1}{\rho_\beta N_\alpha} \left\langle \sum_{\alpha,i} \sum_{\beta,j\neq i} \delta(r - r_{\alpha\beta}) \right\rangle. \tag{5-1}$$

Here δ is the Dirac delta function, N_α is the number of species of type α and ρ_β is the number density of species β. For homogeneous and isotropic materials, the PDF is a function of separation only. In this case $r_{\alpha\beta}$ is the scalar distance from atom α to atom β, and the angled brackets represent a time average. The coordination number, $n(r)_{\alpha\beta}$, of an ion of type α is the average number of ions of type β within a distance r of α. It is defined as an integral of the p-PDF: $n(r)_{\alpha\beta} =$

$4\pi \int \rho_\beta g_{\alpha\beta} r^2 dr$. Finally, the total neutron weighted PDF, $G'(r)$, was calculated to allow comparisons with recent neutron measurements of the structure of glassy LPS.[200] $G'(r)$ is given by:

$$G'(\mathrm{r}) = \left(\sum_\alpha^n c_\alpha \bar{b}_\alpha \right)^{-2} \sum_{\alpha,\beta}^n c_\alpha c_\beta \bar{b}_\alpha \bar{b}_\beta\ g_{\alpha\beta}(r). \tag{5-2}$$

Here, $\bar{b}_i$ is the coherent bound neutron scattering length of an atom of type i[201] and c_i is the concentration of species i. [202]

Figure 5.2a shows p-PDFs for all relevant atom pairs in glassy-Li$_3$PS$_4$ at 300 K. The most prominent peak in the p-PDF is due to the P-S covalent bond found in the PS$_4^{3-}$ tetrahedra, with a maximum at 2.1 Å. The local environment of lithium ions is shown by the blue (Li-S), green (Li-P), and dashed green (Li-Li) lines. Clear peaks exist in the Li p-PDF at 2.5 Å and 3.1 Å, indicating the presence of local ordering with S and P, respectively. Nevertheless, both of the Li-S and Li-P PDFs are non-zero at distances slightly larger than their peak values. (For example, the Li-P PDF exhibits a shoulder at 3.8 Å.) This behavior differs from the localized peak associated with covalent P-S bonds, and indicates greater variability in the local structure of Li. In contrast, the Li-Li PDF exhibits no sharp peaks, suggesting that the Li distribution is disordered. Longer-ranged pair distances include those for S-S and P-P. S-S distances are shown by the black line; peaks at 3.4 Å and 4.0 Å correspond to intra- and inter-PS$_4^{3-}$ distances, respectively. P-P distances (dashed magenta line) exhibit a peak at 6.1 Å, corresponding to the average spacing of PS$_4^{3-}$ centers.

Figure 5.2b illustrates the average coordination number of ions of type A by ions of type B (labeled as 'A-B' in the figure) as a function of distance, r. Turning first to the coordination of P by S, $n(r)$ displays a clear plateau for $r = 2$ to 4 Å. This behavior reflects the well-defined P-S covalent bonds present in the PS$_4^{3-}$ tetrahedra. (Beyond 4 Å, $n(r)$ increases continuously due to

coordination of P by S from different tetrahedra.) In contrast to the behavior of P-S, the coordination number of Li does not exhibit a plateau-like shape. The absence of a plateau-region suggests that Li-ions experience a range of different coordination environments in LPS glass. The coordination number is typically defined at the distance r corresponding to the first minimum in the PDF. For Li-S pairs this minimum occurs at 3.3 Å, corresponding to a coordination of 4.25 sulfur atoms. The fact that $n(r)$ is a non-integer further supports the notion of variable coordination of Li. Finally, a combined analysis of the Li PDF and $n(r)$ suggests that Li-ions experience coordination environments ranging from 3 to 5 S anions.
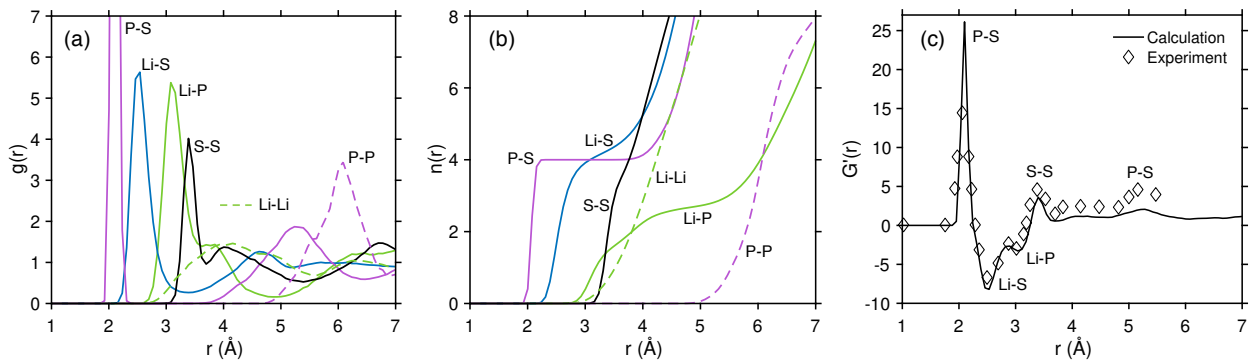
Figure 5.2. Characterization of the static structure of glassy Li_3PS_4 at ambient temperature. (a) Partial pair distribution functions, $g(r)$. (b) Coordination numbers, $n(r)$. (c) Total neutron-weighted pair distribution function, G'(r), (solid line) compared with experimental neutron diffraction data (diamonds) reported by Ohara et al.[200] Atom pair distances associated with the peaks in G'(r) are labeled.

Recently, Ohara et al. performed time-of-flight neutron diffraction measurements on LPS glasses having the same composition as those modeled here.[200] Those measurements suggested that the structure consisted entirely of ortho-thiophosphate anions, consistent with the present computational findings. Figure 5.2c compares the measured and computed total neutron-weighted pair distribution functions, G'(r). Very good agreement is obtained: all of the major peaks in G'(r) are reproduced by both theory and experiments. Furthermore, since Equation 2 is the weighted sum of calculated partial-PDFs, the calculations allow for the determination of the individual pair

distances responsible for each peak in G'(r). Visible in both calculation and experiment are: (*i.*) P-S bonds within and between PS_4^{3-} tetrahedra at 2.1 Å and 5.2 Å, respectively; (*ii.*) S-S pairs at 3.4 Å arising from inter-PS_4^{3-} interactions, and (*iii.*) the Li-anion peaks with characteristic distances of approximately 2.5 Å for Li-S and 3.1 Å for Li-P. All of these distances are very similar to those reported in the p-PDFs of Figure 5.2a. Finally, the simulated G'(r) data also explains why peaks associated with Li-Li and P-P correlations are not observed in the experimental measurements. The absence of the former peaks can be explained by the disordered distribution of Li (see the dashed green line in Figure 5.2a), while the relatively low concentration of P explains the latter omission.

5.3.2 Dynamics

Li migration events were characterized using a protocol previously used to describe dynamics in LLZO and in glass-forming liquids.[190,203] Following those studies, we define the functional, $h_i(t; a, \Delta t, t_a)$ as an indicator of a long-lived Li-ion displacement of at least a distance a occurring at time t:

$$h_i(t; a, \Delta t, t_a) = \prod_{t' = \frac{t_a}{2} - \Delta t}^{t_a/2} \theta(|\boldsymbol{r}_i(t + t') - \boldsymbol{r}_i(t - t')| - a). \qquad (5\text{-}3)$$

$h_i = 1$ for atoms that undergo a displacement, otherwise $h_i = 0$. Here, $\theta(x)$ is the Heaviside step function, while the difference $\boldsymbol{r}_i(t + t') - \boldsymbol{r}_i(t - t')$ represents the displacement of atom i. $\Delta t = 3$ ps, is a residence time that both precedes and follows a displacement event and ensures that these displacements are long-lived. Finally, $t_a = 9$ ps, is a longer time window that includes the residence times and the transition time. Eq. 3 implies that a migration event will occur over a time that is at most $t_a - 2\Delta t$, which, with the current parameters is equal to 3 ps.

Figure 5.3a plots h_i individually for each of the 60 Li-ions contained in the computational

cell during 80 ps of MD at 300 K. The data show that a total of 7 ions underwent long-lived

migration events. Summing Equation 3 at each time t allows for the identification of ions whose

migration events occur simultaneously (or near-simultaneously). These events are shown in Figure

5.3b. The first event observed occurs over a window t = 5 to 9 ps and involves the displacement

of 5 distinct Li-ions. This event can be approximately divided into an initial 3-ion event that is

followed soon afterwards by a 4-ion process. The ions participating in the 4-ion event are

highlighted in blue in Figure 5.3a. (The preceding 3-ion event also involves two of these ions; the

third participating ion is shown without shading in Figure 5.3a.) The displacements of the ions

participating in the 4-body event (relative to their positions at the start of the first residence time)

are shown in Figure 5.3c. These data show that two of the ions undergo large displacements of 4-

5 Å, which are well above the $a = 1.6$ Å threshold for detecting a migration event.
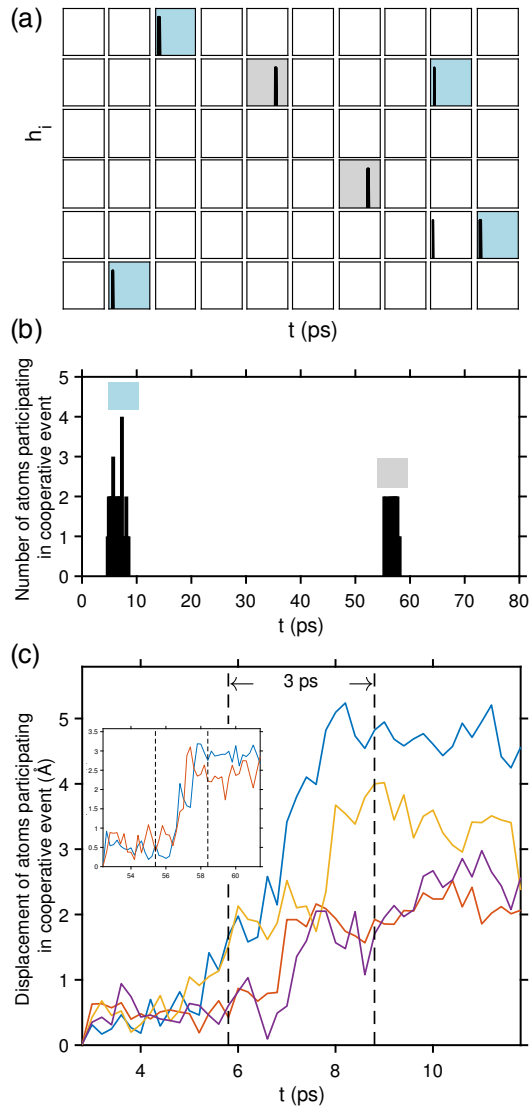
Figure 5.3. (a) Identification of Li-ion migration events at 300 K. (b) Number of atoms participating in cooperative event. Blue and gray shaded subplots correspond to the maximum in the first and second event, respectively. (c) Displacement of the blue shaded Li-ions relative to beginning of residence time (Insert: displacement of gray shaded Li-ions).

A second simultaneous migration event involving two ions occurs at t = 57 ps in Figure 5.3b. These ions are identified with grey shading in Figure 5.3a and displacement shown in the insert of Figure 5.3c. Various values for the parameters used in Equation 5-3 were investigated, the same qualitative behavior persists – i.e., the existence of simultaneous migration events –

across the range of explored parameters. This suggests that the observed behavior is not an artifact of the sampling procedure.

Analysis of the MD trajectories by Equation 5-3 implies that Li-ion migration events in LPS glass are correlated in time. Are these events also correlated in space? Figure 5.4 addresses this question by illustrating the real-space displacements associated with the 4-ion migration event occurring at $t = 7$ ps in Figure 5.3. Trajectories are shown over a time window corresponding to $t = 0$-10 ps in Figure 5.3b.

Figure 5.4a illustrates a sub-set of the computational cell showing the beginning ('B') and end ('E') points for Li trajectories during this window. Similarly, the displacements of nearest-neighbor PS_4 anions (labelled with numbers) are depicted by plotting their positions at the beginning (translucent) and end of the interval (opaque). On the time scale shown here, four adjacent lithium ions undergo migration. Three of these ions, colored orange, teal, and maroon, undergo displacements that impinge upon (or partially overlap with) the previous locations of the others. This behavior is reminiscent of the 'string-like' displacements observed in earlier simulations of Lennard-Jonesian glasses.[181] The forth ion, shown in blue, depicts a displacement of a neighboring Li-ion that shares anion 11 with one of the other mobile ions.
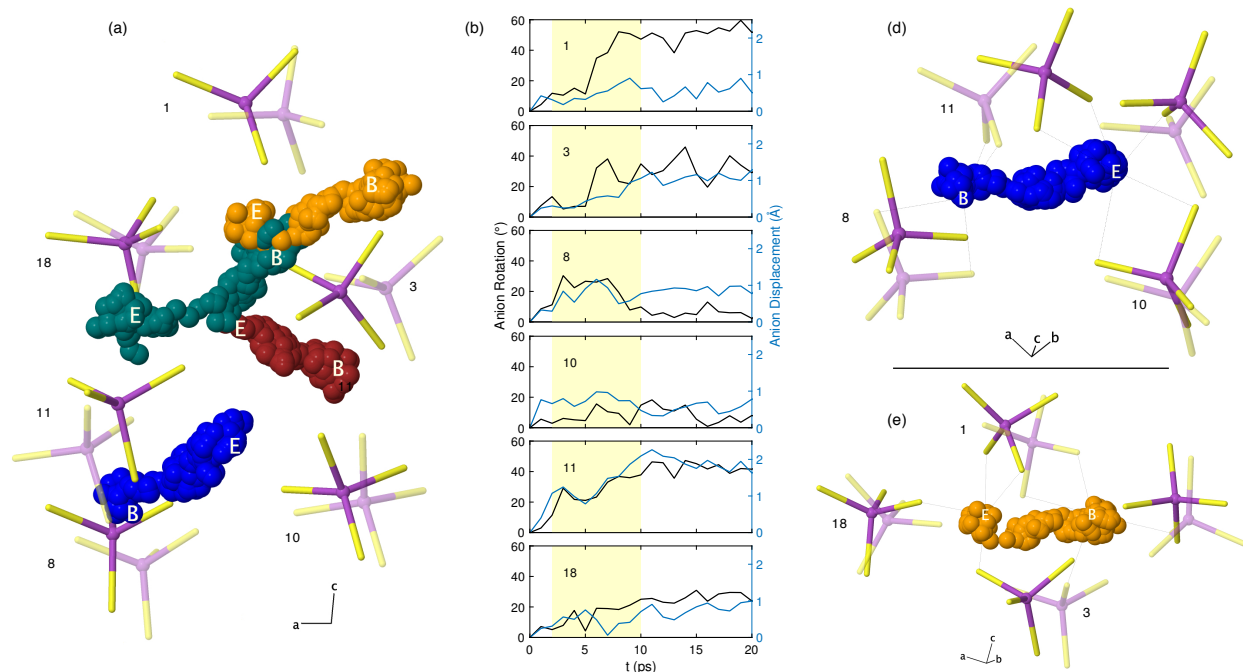
Figure 5.4. Real-space cation-anion cooperative motion event involving multiple adjacent cations with anion reorientation. (a) Distinct colored spheres represent different lithium atoms superimposed at 40 femto-second intervals over a 10 ps trajectory, initial and final position are labeled "B" and "E", respectively. Tetrahedra PS_4 anions are colored magenta and yellow, initial position is translucent and final is opaque, numeric labels refer to individual anions. For clarity, only the portion of the simulation cell is shown. (b) Angular and linear displacement of anions from initial orientation and position. (d-e) Prototypical real-space mechanism of diffusion, illustrating the dynamic coupling of cation transport and reorientation of anions ('paddle-wheel' mechanism). Faint dashed lines indicate sulfur within a 3 Å radius of lithium at times "B" and "E".

Importantly, the nearest-neighbor PS_4 anions, which comprise the solvating 'cage' surrounding the Li prior to migration, also undergo significant rotations during Li migration. Figure 5.4b illustrates these anion displacements and rotations relative to their position at $t = 0$ (i.e., the same time origin as in Figure 5.3b). Rotational displacements are defined with respect to a vector whose tail is located at the center of mass of the anion, corresponding approximately to the position of the central P ion, and whose head sits on a S ion at a vertex of the PS_4 tetrahedron. (Four of these vectors can be drawn; the rotational displacements shown in Figure 5.4b correspond to the vector undergoing the largest displacement.) Linear displacements were tracked based on

the position of the central P ion. The shaded yellow region in Figure 5.4b represents a time window from 2-10 ps where anion angular displacements are the most significant.

Regarding rotational displacements, in the case of anion 1, a large rotation of nearly 45° occurred during t = 5 – 10 ps; the anion then largely remained in that orientation for the following 10 ps. After undergoing a reorientation during t = 5 – 7 ps, anion 3 undergoes oscillatory rotations with displacements as large as 30°. In contrast, anion 8 returns to its initial orientation after a rotational displacement that persists from t = 2 – 10 ps. Anion 11underwent a sustained reorientation of nearly 50°. Finally, anions 10 and 18 did not exhibit significant rotational displacements. The rotational displacements of all anions in the computational cell are shown by the black lines in Figure 5.5
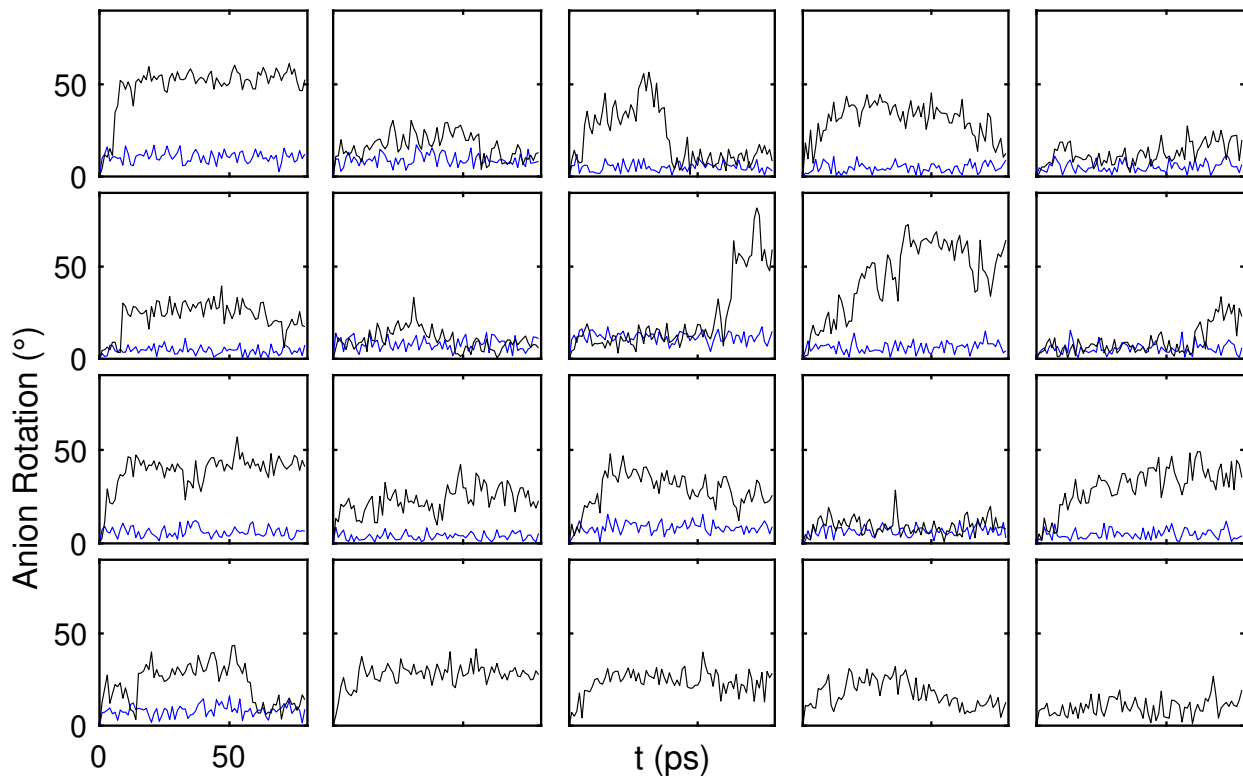
Figure 5.5. Individual anion rotation in glassy-Li_3PS_4 (black) and γ-Li_3PS_4 (blue) at 300 K. γ-Li_3PS_4 crystal structure from Homma *et al.*[199]

For comparison, equivalent AIMD calculations on crystalline γ-Li_3PS_4 were also performed. These angular displacements are also shown by the blue lines in Figure 5.5. In contrast to the large rotational displacements observed for the PS_4 tetrahedra in glassy LPS, no significant rotations were observed in the crystalline system over a 80 ps time window. This suggests that ion migration mechanisms in the glass are qualitatively different from those in the crystalline phase.

Figure 5.4b also illustrates that translational displacement of anions generally accompany their rotation, in contrast to disordered crystals (e.g. where the anions occupy a regular lattice while the cations are distributed at random). The correlation between translation and rotation is evident for the anions that exhibit reorientation, particularly anions 8 and 11. The translation of all anions are shown in Figure 5.6, and compared with crystalline γ-Li_3PS_4. The crystalline system displays the behavior of a fixed anion sub-lattice, while the glass shows significantly more freedom in PS_4 translation and oscillation.
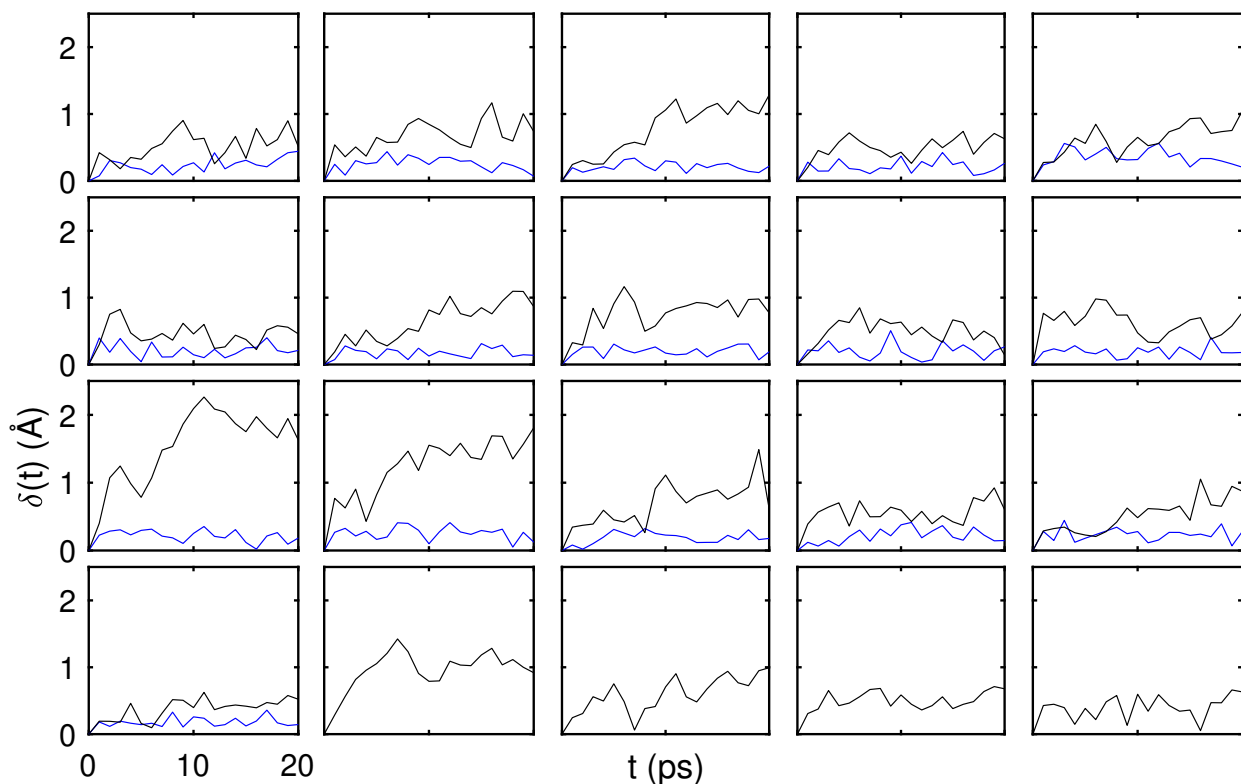
Figure 5.6. Individual anion displacements in glassy-Li$_3$PS$_4$ (black) and γ-Li$_3$PS$_4$ (blue) at 300 K.

Figure 5.4d-e illustrate the dynamic coupling of cation transport and reorientation of anions ('paddle-wheel' mechanism). The blue and orange lithium ions remains coupled to the same two sulfurs ions throughout the reorientation of anion 11 and 1, respectively. In this manner the rotating PS$_4$ tetrahedra are correlated with the long-lived displacement of lithium identified from Equation 5-3. Naturally, the displacement of lithium must also include the uncoordination with anions at "B" and coordination with anions at "E". Such a mechanism could permit lithium to percolate throughout the system by coupled anion reorientations. Although, this mechanism would induce extended correlation effects, as will be discussed later. Enhanced transport of cations by a dynamic coupling to the reorientational motion of polyatomic anions has been discussed widely and supported by quasielastic neutron scattering experiments for alkali metal sulphate and phosphate crystalline SEs.[187,204–208] Similar experiments suggest the high temperature transition to a

superionic conducting phase is accompanied by anion reorientation in the borate class of SEs.[209] We are not aware of any computational or experimental anion reorientation studies on lithium thiophosphates.

The degree of freedom for anion motion is also evident in the illustration of particle density shown in Figure 5.7. Lithium is shown in green, and its behavior is typical of caged motion due to the shell of neighboring anions. In resemblance to lithium, sulfur (shown in yellow) displays a degree of motion corresponding to the rotation of the PS_4 anion. In contrast, phosphorus (shown in teal) displays considerably less freedom of motion.
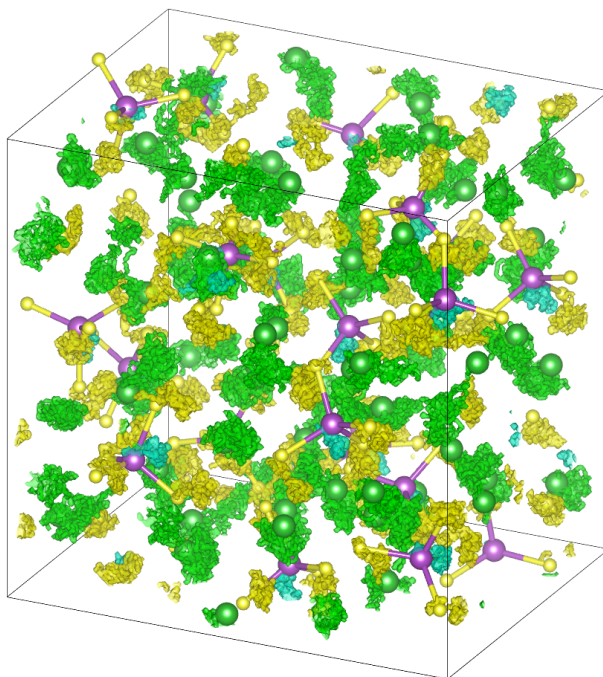
Figure 5.7. Particle density at 300 K averaged over 10 ps. Evaluated on a grid of 0.08 Å, isosurface level shown is 10^{-4} Bohr^{-3}. Green is lithium, yellow sulfur, and teal is phosphorus.

The above discussion illustrates considerable room temperature rotational mobility of anions and correlated cation-anion dynamics. To characterize these dynamics further we calculated the power spectrum $\tilde{Z}(\omega)$, of cation velocity $\boldsymbol{v}$, and anion angular velocity $\boldsymbol{\omega} = \mathbf{u} \times \dot{\mathbf{u}}$:

$$\tilde{Z}(\omega) = \int Z(t)e^{i\omega t}dt \qquad\qquad (5\text{-}4)$$

$$Z(t) = \langle \boldsymbol{x}(t) \cdot \boldsymbol{x}(0) \rangle / \langle \boldsymbol{x}^2 \rangle, \qquad \boldsymbol{x} = \boldsymbol{v}, \boldsymbol{\omega}$$

where **u** is a unit vector from the anion center of mass to a sulfur ion.[210]
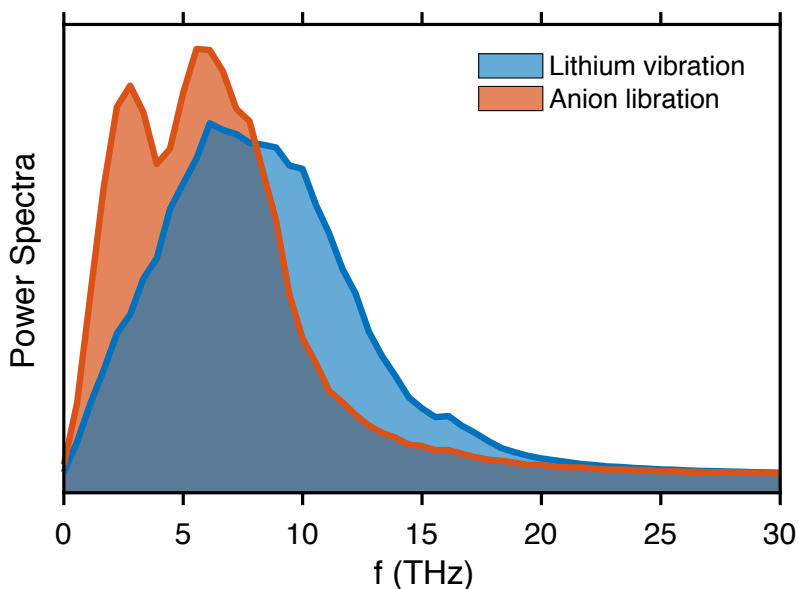
Figure 5.8. Power spectrum of lithium (blue) and anion (red) at 300 K.

Figure 5.8 illustrates a coupling between two dynamical processes, lithium vibrations and anion librations. Both processes exhibit significant overlap of low frequency modes (0 to 10 THz), and both have a maximum at 6 THz. The intrinsic anion libration dynamics facilitate lithium transport by the paddle-wheel mechanism (as shown in Figure 5.4) but also alter the local energy landscape. Referring back to Figure 5.2b, we note that the Li-S coordination number at the minimum in the p-PDF is 4.25, which indicates lithium is shared among at least two anions, and likewise anions are sharing multiple lithium. The coupled cation-anion reorientational motion would inevitably uncoordinate lithium from neighboring anions (and itself) creating "new vacancies" and inducing additional nearby lithium to migrate as they seek new local energy minima–leading to the 'string' mechanism of diffusion. Moreover, lithium that are uncoordinated

from adjoining anions also change the local energy landscape of those anions persuading further anion rotation and potentially a cascade of cation transport and anion rotation. Clearly, there is no simple classification of mechanisms in a highly correlated diffusion process; instead several mechanisms can work in unison: (*i*) anion reorientation actively transports cations; (*ii*) reorientation passively transports cations as a passage mechanism, where cation diffusion pathways of different sizes are obtained; (*iii*) rotationally mobile anions accommodate the passage of cations.[205]

5.4   Additional Content

5.4.1   Elastic Properties

The elastic moduli are important design parameters for all-solid-state lithium ion batteries. The considerable volume changes that occur throughout operation can result in fragmentation of the solid and poor electrolyte/electrode contact resulting in poor cycle life and stability. A desirable electrolyte can accommodate these strains by reversible deformation, which could be aided by small elastic moduli. Moreover, small moduli are indicative of a material suitable for room temperature sintering which is ideal for an economical grade solid electrolyte.[211]

Glassy LPS has been shown experimentally to have favorable mechanical properties.[211–213] However, there are no reports of these properties determined from *ab initio* calculations. We have calculated the 21 independent elastic constants needed to describe the elastic properties of glassy lithium thiophosphate.

The elastic constants C_{ij} were determined from the stress due to applying six finite strains with displacement ± 0.015 Å as implemented in VASP.[214] The bulk, shear, and Young's modulus are calculated with the Voigt-Reuss-Hill approximation which transforms single-crystal elastic constants into polycrystalline elastic moduli.[215] The Voigt moduli provide the upper bound while

86

Reuss moduli is the lower bound, the Hill moduli is the arithmetic average of the two. The bulk

modulus B was calculated as:

$$B_V = \frac{(C_{11} + C_{22} + C_{33} + 2(C_{12} + C_{23} + C_{31}))}{9} \tag{5-5}$$

$$B_R = \frac{1}{(S_{11} + S_{22} + S_{33} + 2(S_{12} + S_{23} + S_{31}))} \tag{5-6}$$

$$B_H = \frac{(B_V + B_R)}{2} \tag{5-7}$$

where S is the compliance tensor and the subscripts refer to either the Voigt, Reuss, or Hill moduli.

The shear modulus G was obtained from the following equations:

$$G_{V=} \frac{(C_{11} + C_{22} + C_{33} - C_{12} - C_{23} - C_{31} + 3(C_{44} + C_{55} + C_{66}))}{15} \tag{5-8}$$

$$G_R = \frac{15}{(4(S_{11} + S_{22} + S_{33}) - 4(S_{12} + S_{23} + S_{31}) + 3(S_{44} + S_{55} + S_{66}))} \tag{5-9}$$

$$G_H = \frac{(G_V + G_R)}{2}. \tag{5-10}$$

The Young's moduli E and Poisson's ratio v are determined by:

$$E = \frac{9BG}{2(3B + G)}, \qquad v = \frac{(3B - 2G)}{2(3B + G)}. \tag{5-11}$$

The 21 independent elastic constants and moduli of glassy-Li_3PS_4 are shown in Table 5.1 at four

densities, 1.55, 1.65, 1.76, and 2.42 g cm^{-3} corresponding to pressures of 1 Bar, 3.6, 10, and 100

kBar, respectively.

Table 5.1. Calculated mechanical properties of glassy-Li$_3$PS$_4$ and crystals: γ- Li$_3$PS$_4$, β-Li$_3$PS$_4$, Li$_7$P$_3$S$_{11}$; elastic constants C_{ij}, bulk modulus B, shear modulus G, Young's modulus E, and Poisson's ratio ν as a function of hydrostatic pressure P, and corresponding density ρ.

	P (kBar)	ρ (g/cm³)	B (GPa)	G (GPa)	E (GPa)	ν	C_{ij}					
glass-Li$_3$PS$_4$												
This work	0.001	1.55	9.82	5.10	13.04	0.28	12.7	6.4	6.8	0.4	0.0	-1.5
							6.4	15.7	7.3	1.7	-1.0	-0.9
							6.8	7.3	19.7	0.8	-1.2	0.1
							0.4	1.7	-1.2	5.5	0.4	-0.3
							0.0	-1.0	-1.2	0.4	5.8	0.4
							-1.5	-0.9	0.1	-0.3	0.4	6.2
This work	3.6	1.65	14.26	6.75	17.49	0.30	20.6	9.7	9.8	-0.4	-0.2	-0.5
							9.7	25.2	10.0	1.3	-0.1	-0.9
							9.8	10.0	24.1	0.4	0.2	-0.3
							-0.4	1.3	0.2	7.4	-0.6	0.0
							-0.2	-0.1	0.2	-0.6	6.6	0.3
							-0.5	-0.9	-0.3	0.0	0.3	6.8
This work	10	1.76	16.93	6.61	17.54	0.33	24.4	12.0	13.4	-1.3	-0.1	0.7
							12.0	26.8	12.0	-0.8	0.1	2.0
							13.4	12.0	27.7	1.1	-3.5	0.6
							-1.3	-0.8	-3.5	8.3	-0.7	0.9
							-0.1	0.1	-3.5	-0.7	7.2	-0.2
							0.7	2.0	0.6	0.9	-0.2	5.1
This work	100	2.42	50.70	16.27	44.10	0.36	71.8	37.2	41.7	-0.5	-0.2	-0.3
							37.2	71.5	41.2	-1.3	0.7	-0.1
							41.7	41.2	71.0	0.5	6.1	1.8
							-0.5	-1.3	6.1	18.9	0.3	-0.1
							-0.2	0.7	6.1	0.3	17.6	-0.4
							-0.3	-0.1	1.8	-0.1	-0.4	14.4
Expt. Ref.[212]	1.8	1.45	–	3.40	8.80	0.28						
	3.6	1.68	–	5.90	15.00	0.30						
γ-Li$_3$PS$_4$												
This work		1.87	31.90	13.02	34.40	0.32						
Calc. Ref.[216]			32.90	12.60	33.40	0.33						
Calc. Ref.[217]			31.90	14.11	36.88	0.31						
β-Li$_3$PS$_4$												
This work		1.80	21.72	11.14	28.55	0.28						
Calc. Ref. [216]			23.30	11.40	29.50	0.29						
Calc. Ref. [217]			21.39	11.33	28.90	0.27						
Li$_7$P$_3$S$_{11}$												
This work		1.80	23.43	9.32	24.69	0.32						
Calc. Ref. [216]			23.90	8.10	21.90	0.35						

The Young's modulus increases with the density and its magnitude agrees well with the extensive experiments performed by Sakuda.[212] We have also calculated the moduli of the crystalline structures reported by Homma *et al*[199] using the same methodology as the glassy phase. The latter has lower moduli compared to the crystalline phases, which is typically for disordered materials. Additionally, we compare our calculated moduli of crystalline phases with other *ab initio* studies of crystalline LPS and those results are in very good agreement.

5.4.2 Diffusivity

Parrinello-Rahman dynamics (NPT) allows the computational cell to establish equilibrium density under constant external hydrostatic pressure. Lithium diffusivity was evaluated with applied pressures of 1 Bar, 3.6, 10, and 100 kBar. The mean square displacement is defined as,

$$\langle \delta^2(t) \rangle = \langle |r(t) - r(0)|^2 \rangle, \tag{5-12}$$

where r is the position of an atom, the enclosing brackets is the mean with respect to time. For motion in the diffusive regime, the Einstein relation yields

$$\langle \delta^2(t) \rangle = 6Dt \tag{5-13}$$

where D is the diffusion coefficient. Shown in Figure 5.9, at 1000 K and 700 K pressures up to 10 kBar have little influence on the diffusion coefficient. However, 100 kBar results in a diffusion coefficient nearly one order of magnitude lower. At 500 K and lower temperatures, the system has not fully reached the diffusive limit.
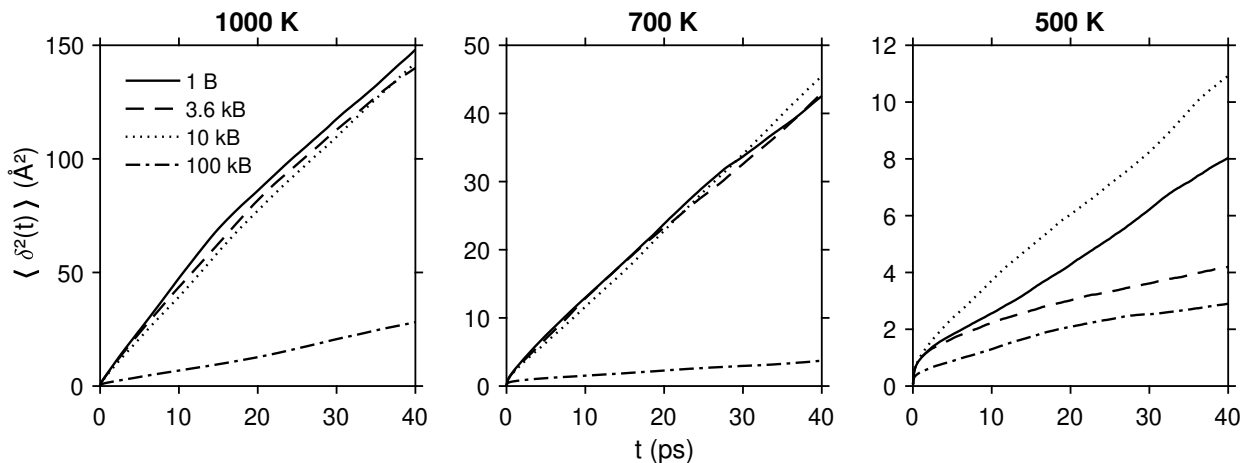
Figure 5.9. Mean square displacement of lithium in glassy Li₃PS₄ as a function of temperature and pressure.

Shown in Table 5.2, the hydrostatic pressure results in an increased density, at 10 kBar the density is similar to the calculated density at 300 K for the crystalline stable phase γ- Li₃PS₄, and high temperature phase β-Li₃PS₄ (Table 5.3). The density at 100 kB is a 50% increase to the density at atmospheric pressure. Higher density reduces the available volume of cation diffusion pathways and likely constrains anion rotational mobility, both are contributing factors to the decrease in diffusivity at high pressure.

Table 5.2. Calculated density of glassy-Li₃PS₄ as a function of temperature and pressure.

	T (K)				
P (kBar)	1000	700	500	400	300
0.001	1.44	1.50	1.47	1.49	1.55
3.6	1.56	1.60	1.62	1.63	1.63
10	1.69	1.74	1.76	1.73	1.76
100	2.35	2.39	2.41	2.42	2.42

Table 5.3. Calculated and experimental density of glassy-Li₃PS₄, γ- Li₃PS₄, and β-Li₃PS₄.

	Density (g/cm^3)		
	glassy-Li$_3$PS$_4$	γ-Li$_3$PS$_4$	β-Li$_3$PS$_4$
Expt.	—	1.93 (297 K)	1.85 (637 K)
Calc. (0 K)	1.62	1.87	1.80
Calc. (300 K)	1.55	1.83	1.76

The diffusivity and activation energy at a pressure of 1 Bar are shown in Figure 5.10. The activation energy is 0.25 eV with an extrapolated diffusion coefficient at 300 K of 6.7×10^{-8} cm^2 s^{-1}. Assuming the Nernst-Einstein relation holds, the conductivity is 6.5 mS cm^{-1}. Experimentally, mixture of Li$_2$S–P$_2$S$_5$ with stoichiometry Li$_3$PS$_4$ prepared by mechanical milling have been shown to yield a conductivity of 0.3 mS cm^{-1} and 0.4 eV for the activation energy.[218]
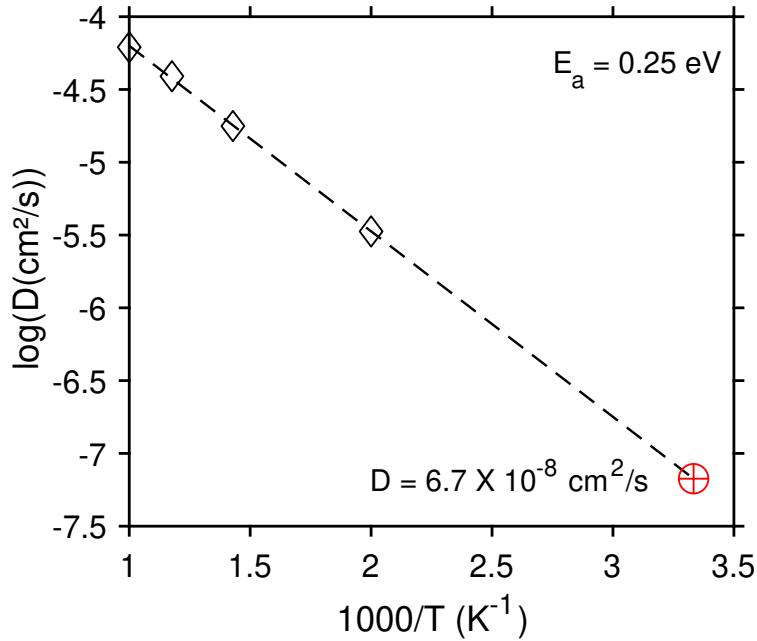

Figure 5.10. Diffusivity and activation energy at 1 Bar. The extrapolated diffusion coefficient at 300 K is shown by the red marker and in text at 300 K.

Chapter 6

Conclusions and Next Steps

The Mg-air chemistry is an enticing composition for a battery system due to its essentially inexhaustible supply of cathode reactant (oxygen) combined with an earth-abundant multi-valent metal anode and higher safety compared to Li analogues. Nevertheless, relatively few experimental studies of this system have been reported, and these studies demonstrate performance that is far from ideal: high discharge overpotentials and the electrochemical irreversibility of magnesium oxide. These reports illustrate the challenges that remain before the benefits of the Mg/O_2 chemistry can be realized in a practical cell.

This work addresses these challenges by employing first principles calculations to characterize reaction mechanisms associated with discharge and charging, and the charge transport properties of likely discharge products, MgO and MgO_2. These calculations indicate that reaction pathways involving intermediates such as superoxides and peroxides are preferred. In agreement with experiment, calculations predict MgO to be electrochemically irreversible. In contrast, MgO_2-based batteries are predicted to exhibit low overpotentials with efficiencies approaching 90%. This suggests that performance can be improved by 'steering' discharge towards formation of MgO_2.

Intrinsic charge transport in MgO and MgO_2 is predicted to be hole polarons. The equilibrium concentration is low at the near-ambient temperatures expected for battery operation. Consequently, if equilibrium carrier concentration is realized, the conductivity for both MgO and MgO_2 will be low and limit battery performance. Nevertheless, charge transport within the

92

discharge products will be strongly influenced by nonequilibrium carrier concentrations. This, in combination with high/moderate mobilities predicted for hole polarons suggests a strategy for improving conductivity: artificially increasing polaron concentration via the incorporation of monovalent impurities into the discharge product during its growth. Finally, the calculated conductivity for MgO is in remarkable agreement with the three Arrhenius branches reported in experiment.

Looking to the future, MgO-based batteries will likely suffer from intrinsically high charging overpotentials. Consequently, redox-mediators should be employed to facilitate a favorable oxygen evolution reaction. Overall, research efforts should focus on biasing discharge toward the formation of MgO_2. As a preliminary step to examine the viability of a MgO_2-based cell, magnesium peroxide can be prepared by the methods of Vannerberg[47] or Volnov and Latysheva[43] and electrochemically recharged using the approach of Shiga et al.[11]

The challenge of developing lithium solid electrolytes with conductivity as high or higher than conventional liquid electrolytes has been overcome with sulfide class of solids. However, interpretation of ionic transport processes in the amorphous versions of these materials has lagged far behind understanding of crystalline materials. Furthermore, the first fast ion conductors discovered were found to have a highly ordered and immobile sublattice which provided the framework for mobile ions. Subsequently, emphasis has been and currently is placed on understanding ion transport in terms of the static host-lattice.

This work examines correlated effects in the transport processes of glassy lithium thiophosphate. In contrast to the largely static role anions play in crystalline systems for cation transport, we find lithium to be dynamically coupled to the reorientation and thermal vibration of

ortho-thiophosphate anions. This suggests that the coordination environment provided by a static host-structure alone is insufficient to account for fast ion conduction in lithium glasses.

Towards a goal of realizing batteries that rely on earth abundant metals, first principles simulations can be utilized to acquire a better understanding of transport in multivalent sulfide solid solution electrolytes, for instance, compositions where magnesium, calcium, and aluminum are the working ions. The diffusion of these cations are generally poor in intercalation cathodes, which may explain their lack of consideration as solid electrolytes. Nevertheless, the diffusion rates of large ions can be nearly equal to that of lithium in several high temperature modifications of sulfate mixtures, where it was proposed that diffusion of the larger ions was made possible by the rotational motion of the sulfate anions.[187] We have directly observed the coupled rotational motion at room temperature in lithium thiophosphate glass. This, combined with experimental observations, opens the possibility that high diffusivity at room temperature is not limited by the size of the working cation and the size of the diffusion pathways provided by the host-sublattice. If high rotational mobility of polyatomic anions persists at room temperature in the presence of multivalent cations then fast ion conducting multivalent solid electrolytes may be a realized. Earth abundant solid electrolytes would transform the search for "beyond Li-ion" technologies.

Appendix A

Vibrational Spectra of MgO and MgO$_2$

Density functional perturbation theory[34,219] was used to calculate Infrared and Raman activities in MgO$_2$. Calculations were performed using the VASP code.[60–63] The generalized gradient approximation (GGA) expressed using the formulation of Perdew-Burke-Ernzerhof (PBE) was used for the exchange-correlation energy.[64] A kinetic energy cutoff of 520 eV was used for the planewave basis, and the brilloiun zone was sampled with a regular, Γ-centered grid with a density of 16×16×16, corresponding to 24 k-points per Å^{-1}. All ion positions were relaxed to a force tolerance less than 10^{-5} eV/Å. Born effective charge tensors and dielectric tensors were calculated for each atom according to the method of Gajdos.[153] The Hellmann-Feynman forces were used in combination with the supplemented direct method[33] to evaluate the interatomic force constants of a 2×2×2 supercell. To calculate the phonon frequencies in the long wavelength limit, the macroscopic electric field that follows from the collective displacement of ions was treated separately using the non-analytical form of the dynamical matrix.[34,36] The derivatives of the polarizability tensor with respect to atomic displacements were calculated using a finite difference approach; ions were displaced ±0.06 Å in each Cartesian direction. The Raman susceptibility tensor was then constructed and applied to the differential cross section for nonresonant first-order Raman scattering. The calculation was performed for a polycrystal using 532 nm unpolarized light at 300 K. Phonon dispersion and density of states is shown in Figure A.1. Infrared and Raman activity is shown in Figure A.2. The phonon and Raman frequency at 26 THz arises from a mode associated with the covalently bonded oxygen dimer in MgO$_2$.
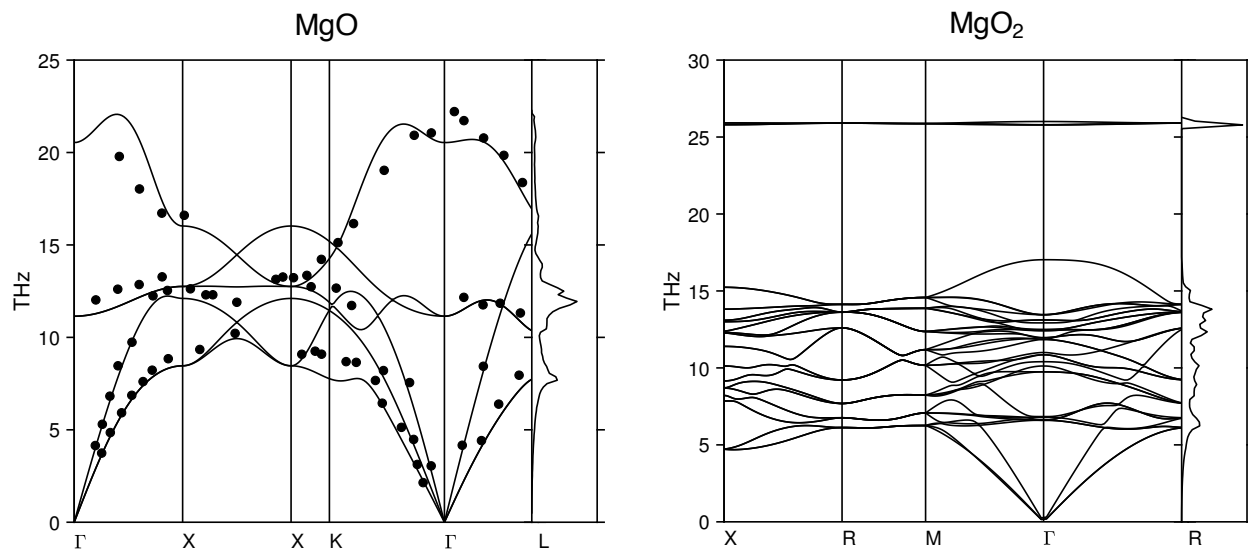
Figure A.1. Phonon dispersion and density of states for MgO and MgO_2. For MgO, experimental data from inelastic neutron scattering is shown by black circles.[164]
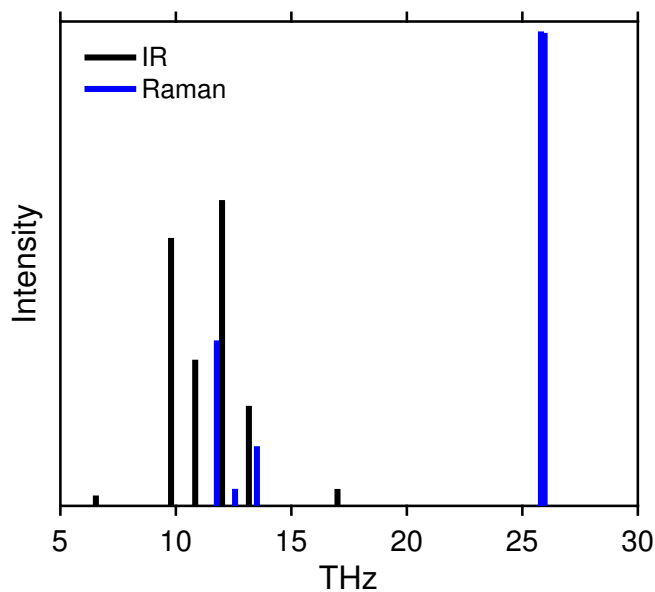

Figure A.2. Infrared and Raman Spectra of MgO_2.

Bibliography

(1)   Bruce, P. G.; Freunberger, S. A.; Hardwick, L. J.; Tarascon, J.-M. Li-O2 and Li-S Batteries with High Energy Storage. *Nat. Mater.* **2012**, *11*, 19–29.

(2)   *Batteries 2017 Annual Progress Report*; Washington, D.C., 2018.

(3)   Tarascon, J. M.; Armand, M. Issues and Challenges Facing Rechargeable Lithium Batteries. *Nature* **2001**, *414*, 359–367.

(4)   Armand, M.; Tarascon, J.-M. Building Better Batteries. *Nature* **2008**, *451*, 652–657.

(5)   Bruce, P. G.; Freunberger, S. a.; Hardwick, L. J.; Tarascon, J.-M. Li–O2 and Li–S Batteries with High Energy Storage. *Nat. Mater.* **2012**, *11*, 19–29.

(6)   Van Noorden, R. A Better Battery. *Nature* **2014**, *507*.

(7)   Harting, K.; Kunz, U.; Turek, T. Zinc-Air Batteries: Prospects and Challenges for Future Improvement. *Zeitschrift für Phys. Chemie* **2012**, *226*, 151–166.

(8)   Carson, W. N.; Kent, C. E. The Magnesium-Air Cell. In *Power Sources*; Collins, D. H., Ed.; Elsevier, 1967; pp 119–131.

(9)   Muldoon, J.; Bucur, C. B.; Oliver, A. G.; Sugimoto, T.; Matsui, M.; Kim, H. S.; Allred, G. D.; Zajicek, J.; Kotani, Y. Electrolyte Roadblocks to a Magnesium Rechargeable Battery. *Energy Environ. Sci.* **2012**, *5*, 5941–5950.

(10)   Abraham, K. M. A Brief History of Non-Aqueous Metal-Air Batteries. *ECS Trans.* **2008**, *3*, 67–71.

(11)   Shiga, T.; Hase, Y.; Kato, Y.; Inoue, M.; Takechi, K. A Rechargeable Non-Aqueous Mg-O2 Battery. *Chem. Commun.* **2013**, *49*, 9152–9154.

(12)   Shiga, T.; Hase, Y.; Yagi, Y.; Takahashi, N.; Takechi, K. Catalytic Cycle Employing a TEMPO − Anion Complex to Obtain a Secondary Mg − O2 Battery. *J. Phys. Chem. Lett* **2014**, *5*, 1648–1652.

(13)   Vardar, G.; Nelson, E. G.; Smith, J. G.; Naruse, J.; Hiramatsu, H.; Bartlett, B. M.; Sleightholme, A. E. S.; Siegel, D. J.; Monroe, C. W. Identifying the Discharge Product and Reaction Pathway for a Secondary Mg/O2 Battery. *Chem. Mater.* **2015**, *27*, 7564–7568.

(14)   Tubandt, C.; Lorenz, E. Molekularzustand Und Elektrisches Leitvermögen Kristallisierter Salze. *Zeitschrift für Phys. Chemie* **1914**, *87*, 513–542.

(15)   Funke, K. Marking the Centennial of the Discovery of Alpha Silver Iodide. *Diffus. Found.* **2016**, *6*, 1–43.

(16)   Funke, K. AgI-Type Solid Electrolytes. *Prog. Solid State Chem.* **1976**, *11*, 345–402.

(17)   Jost, W. *Diffusion in Solids, Liquids, Gases*; Academic Press: New York, 1960.

(18)   Armstrong, R. D.; Bulmer, R. S.; Dickinson, T. Some Factors Responsible for High Ionic Conductivity in Simple Solid Compounds. *J. Solid State Chem.* **1973**, *8*, 219–228.

(19)   Ingram, M. D. Ionic Conductivity in Glass. *Phys. Chem. Glas.* **1987**, *28*, 215–234.

(20)   Ravaine, D. Glasses as Solid Electrolytes. *J. Non. Cryst. Solids* **1980**, *38–39*, 353–358.

(21)   Malugani, J. P.; Robert, G. Preparation and Electrical Properties of the 0,37Li2S-0,18P2S5-0,45LiI Glass. *Solid State Ionics* **1980**, *1*, 519–523.

(22)   Mercier, R.; Malugani, J.-P.; Fahys, B.; Robert, G. Superionic Conduction in Li2S - P2S5 - LiI - Glasses. *Solid State Ionics* **1981**, *5*, 663–666.

(23)   Malugani, J. P.; Wasniewski, A.; Doreau, M.; Robert, G.; Rikabi, A. Al. Conductivite Ionique Dans Les Verres AgPO3-AgX (X = I.Br.Cl). *Mater. Res. Bull.* **1978**, *13*, 427–433.

(24)   Kato, Y.; Hori, S.; Saito, T.; Suzuki, K.; Hirayama, M.; Mitsui, A.; Yonemura, M.; Iba, H.; Kanno, R. High-Power All-Solid-State Batteries Using Sulfide Superionic Conductors. *Nat.*

Energy **2016**, *1*, 16030.

(25) Seino, Y.; Ota, T.; Takada, K.; Hayashi, A.; Tatsumisago, M. A Sulphide Lithium Super Ion Conductor Is Superior to Liquid Ion Conductors for Use in Rechargeable Batteries. *Energy Environ. Sci.* **2014**, *7*, 627–631.

(26) Kamaya, N.; Homma, K.; Yamakawa, Y.; Hirayama, M.; Kanno, R.; Yonemura, M.; Kamiyama, T.; Kato, Y.; Hama, S.; Kawamoto, K.; et al. A Lithium Superionic Conductor. *Nat. Mater.* **2011**, *10*, 682–686.

(27) Ohtomo, T.; Hayashi, A.; Tatsumisago, M.; Tsuchida, Y.; Hama, S.; Kawamoto, K. All-Solid-State Lithium Secondary Batteries Using the 75Li2S·25P2S5 Glass and the 70Li2S·30P2S5 Glass-Ceramic as Solid Electrolytes. *J. Power Sources* **2013**, *233*, 231–235.

(28) Feynman, R. P.; Leighton, R. B.; Sands, M. L. *The Feynman Lectures of Physics*; Addison Wesley: Reading, Massachusetts, 1963.

(29) Hohenberg, P.; Kohn, W. Inhomogeneous Electron Gas. *Phys. Rev.* **1964**, *136*, B864–B871.

(30) Kohn, W.; Sham, L. J. Self-Consistent Equations Including Exchange and Correlation Effects. *Phys. Rev.* **1965**, *140*.

(31) Parrinello, M.; Rahman, A. Crystal Structure and Pair Potentials: A Molecular-Dynamics Study. *Phys. Rev. Lett.* **1980**, *45*, 1196–1199.

(32) Allen, M.; Tildeslay, D. *Computer Simulations of Liquids*, Second.; Oxford University Press: Oxford, United Kingdom, 2017.

(33) Parlinski, K.; Li, Z.; Kawazoe, Y. First-Principles Determination of the Soft Mode in Cubic ZrO2. *Phys. Rev. Lett.* **1997**, *78*, 4063–4066.

(34) Gonze, X.; Lee, C. Dynamical Matrices, Born Effective Charges, Dielectric Permittivity Tensors, and Interatomic Force Constants from Density-Functional Perturbation Theory. *Phys. Rev. B* **1997**, *55*.

(35) Gonze, X. First-Principles Responses of Solids to Atomic Displacements and Homogeneous Electric Fields: Implementation of a Conjugate-Gradient Algorithm. *Phys. Rev. B* **1997**, *55*, 10337–10354.

(36) Parlinski, K. PHONON. 2014.

(37) Wichtendahl, R.; Ha, U.; Kuhlenbeck, H.; Freund, H. TDS Study of the Bonding of CO and NO to Vacuum-Cleaved NiO (100). *Surf. Sci.* **1999**, *423*, 90–98.

(38) Muldoon, J.; Bucur, C. B.; Gregory, T. Quest for Nonaqueous Multivalent Secondary Batteries: Magnesium and Beyond. *Chem. Rev.* **2014**, *114*, 11683–11720.

(39) Radin, M. D.; Rodriguez, J. F.; Tian, F.; Siegel, D. J. Lithium Peroxide Surfaces Are Metallic, While Lithium Oxide Surfaces Are Not. *J. Am. Chem. Soc.* **2012**, *134*, 1093–1103.

(40) Xu, W.; Xu, K.; Viswanathan, V. V.; Towne, S. A.; Hardy, J. S.; Xiao, J.; Nie, Z.; Hu, D.; Wang, D.; Zhang, J. G. Reaction Mechanisms for the Limited Reversibility of Li-O 2 Chemistry in Organic Carbonate Electrolytes. *J. Power Sources* **2011**, *196*, 9631–9639.

(41) Obrovac, M. N.; Dunlap, R. A.; Sanderson, R. J.; Dahn, J. R. The Electrochemical Displacement Reaction of Lithium with Metal Oxides. *J. Electrochem. Soc.* **2001**, *148*, A576–A588.

(42) Poizot, P.; Laruelle, S.; Grugeon, S.; Dupont, L.; Tarascon, J.-M. Nano-Sized Transition-Metal Oxides as Negative-Electrode Materials for Lithium-Ion Batteries. *Nature* **2000**, *407*.

(43) Volnov, I.; Latysheva, E. Thermal Stability of Magnesium Peroxide. *Izv. Akad. Nauk SSSR* **1970**, No. 1, 13–18.

(44) Chase, M. W. NIST-JANAF Thermochemical Tables, 4th Ed. *Am. Inst. Phys.* **1998**.

(45) Coughlin, J. P. Contributions to the Data on Theoretical Metallurgy. *Bur. Mines* **1954**, *542*.

(46) Hartmann, P.; Bender, C. L.; Vračar, M.; Dürr, A. K.; Garsuch, A.; Janek, J.; Adelhelm, P. A Rechargeable Room-Temperature Sodium Superoxide (NaO2) Battery. *Nat. Mater.* **2013**, *12*, 228–232.

(47) Vannerberg, N. The Formation and Structure of Magnesium Peroxide. *Ark. foer Kemi* **1959**, *14*, 99–105.

(48) Volnov, I. I.; Tokareva, S. A.; Belevskii, V. N.; Latysheva, E. I. The Formation of Magnesium Perperoxide in the Reaction of Magnesium Peroxide with Ozone. *Izv. Akad. Nauk SSSR* **1970**, No. 3, 468–471.

(49) Nørskov, J. K.; Rossmeisl, J.; Logadottir, A.; Lindqvist, L.; Kitchin, J. R.; Bligaard, T.; Jonsson, H. Origin of the Overpotential for Oxygen Reduction at a Fuel-Cell Cathode. *J. Phys. Chem. B* **2004**, *108*, 17886–17892.

(50) Greeley, J.; Stephens, I. E. L.; Bondarenko, A. S.; Johansson, T. P.; Hansen, H. A.; Jaramillo, T. F.; Rossmeisl, J.; Chorkendorff, I.; Nørskov, J. K. Alloys of Platinum and Early Transition Metals as Oxygen Reduction Electrocatalysts. *Nat. Chem.* **2009**, *1*, 552–556.

(51) Man, I. C.; Su, H.-Y.; Calle-Vallejo, F.; Hansen, H. A.; Martínez, J. I.; Inoglu, N. G.; Kitchin, J.; Jaramillo, T. F.; Nørskov, J. K.; Rossmeisl, J. Universality in Oxygen Evolution Electrocatalysis on Oxide Surfaces. *ChemCatChem* **2011**, *3*, 1159–1165.

(52) Greeley, J.; Jaramillo, T. F.; Bonde, J.; Chorkendorff, I. B.; Nørskov, J. K. Computational High-Throughput Screening of Electrocatalytic Materials for Hydrogen Evolution. *Nat. Mater.* **2006**, *5*, 909–913.

(53) Nørskov, J. K.; Bligaard, T.; Rossmeisl, J.; Christensen, C. H. Towards the Computational Design of Solid Catalysts. *Nat. Chem.* **2009**, *1*, 37–46.

(54) Hummelshøj, J. S.; Blomqvist, J.; Datta, S.; Vegge, T.; Rossmeisl, J.; Thygesen, K. S.; Luntz, A. C.; Jacobsen, K. W.; Nørskov, J. K. Communications: Elementary Oxygen Electrode Reactions in the Aprotic Li-Air Battery. *J. Chem. Phys.* **2010**, *132*, 071101-4.

(55) Hummelshøj, J. S.; Luntz, A. C.; Nørskov, J. K. Theoretical Evidence for Low Kinetic Overpotentials in Li-O2 Electrochemistry. *J. Chem. Phys.* **2013**, *138*, 034703-12.

(56) Viswanathan, V.; Norskov, J. K.; Speidel, A.; Scheffler, R.; Gowda, S.; Luntz, A. C. Li−O2 Kinetic Overpotentials: Tafel Plots from Experiment and First-Principles Theory. *J. Phys. Chem. Lett.* **2013**, *4*, 556–560.

(57) Lee, B.; Seo, D.-H.; Lim, H.-D.; Park, I.; Park, K.-Y.; Kim, J.; Kang, K. First-Principles Study of the Reaction Mechanism in Sodium–Oxygen Batteries. *Chem. Mater.* **2014**, *26*, 1048–1055.

(58) Siahrostami, S.; Tripković, V.; Lundgaard, K. T.; Jensen, K. E.; Hansen, H. a; Hummelshøj, J. S.; Mýrdal, J. S. G.; Vegge, T.; Nørskov, J. K.; Rossmeisl, J. First Principles Investigation of Zinc-Anode Dissolution in Zinc-Air Batteries. *Phys. Chem. Chem. Phys.* **2013**, *15*, 6416–6421.

(59) Chen, L. D.; Norskov, J. K.; Luntz, A. C. Al − Air Batteries: Fundamental Thermodynamic Limitations from First-Principles Theory. *J. Phys. Chem. Lett.* **2015**, *6*, 175–179.

(60) Kresse, G.; Furthmuller, J. Efficiency of Ab-Initio Total Energy Calculations for Metals and Semiconductors Using a Plane-Wave Basis Set. *Comput. Mater. Sci.* **1996**, *6*, 15–50.

(61) Kresse, G.; Hafner, J. Ab Initio Molecular Dynamics for Liquid Metals. *Phys. Rev. B* **1993**, *47*, 558–561.

(62) Kresse, G.; Hafner, J. Ab Initio Molecular-Dynamics Simulation of the Liquid-Metal-

Amorphous-Semiconductor Transition in Germanium. *Phys. Rev. B* **1994**, *49*, 14251–14269.

(63) Kresse, G.; Furthmüller, J. Efficient Iterative Schemes for Ab Initio Total-Energy Calculations Using a Plane-Wave Basis Set. *Phys. Rev. B. Condens. Matter* **1996**, *54*, 11169–11186.

(64) Perdew, J.; Burke, K.; Ernzerhof, M. Generalized Gradient Approximation Made Simple. *Phys. Rev. Lett.* **1996**, *77*, 3865–3868.

(65) Blochl, P. E. Projector Augmented-Wave Method. *Phys. Rev. B* **1994**, *50*, 17953–17979.

(66) Straumanis, M. E. The Precision Determination of Lattice Constants by the Powder and Rotating Crystal Methods and Applications. *J. Appl. Phys.* **1949**, *20*, 726.

(67) Smith, D. K.; Leider, H. R. Low-Temperature Thermal Expansion of LiH, MgO and CaO. *J. Appl. Crystallogr.* **1968**, *1*, 246–249.

(68) *CRC Handbook of Chemistry and Physics*, 87th ed.; Lide, D. R., Ed.; Taylor and Francis: London, 2006.

(69) Reuter, K.; Scheffler, M. Composition, Structure, and Stability of RuO2(110) as a Function of Oxygen Pressure. *Phys. Rev. B* **2001**, *65*, 035406.

(70) Kang, S.; Mo, Y.; Ong, S. P.; Ceder, G. A Facile Mechanism for Recharging Li2 O2 in Li − O2 Batteries. *Chem. Mater.* **2013**, *25*, 3328–3336.

(71) Kang, S.; Mo, Y.; Ong, S. P.; Ceder, G. Nanoscale Stabilization of Sodium Oxides: Implications for Na-O2 Batteries. *Nano Lett.* **2014**, *14*, 1016–1020.

(72) Christensen, R.; Hummelshøj, J. S.; Hansen, H. A.; Vegge, T. Reducing Systematic Errors in Oxide Species with Density Functional Theory Calculations. *J. Phys. Chem. C* **2015**, *119*, 17596–17601.

(73) Tasker, P. W. The Stability of Ionic Crystal Surfaces. *J. Phys. C Solid State Phys.* **1979**, *12*, 4977–4984.

(74) Westwood, A. R. C.; Goldheim, D. L. Cleavage Surface Energy of {100} Magnesium Oxide. *J. Appl. Phys.* **1963**, *34*, 3335.

(75) Hayun, S.; Tran, T.; Ushakov, S. V; Thron, A. M.; Benthem, K. Van; Navrotsky, A.; Castro, R. H. R. Experimental Methodologies for Assessing the Surface Energy of Highly Hygroscopic Materials : The Case of Nanocrystalline Magnesia. *J. Phys. Chem. C* **2011**, *115*, 23929–23935.

(76) Bajdich, M.; Nørskov, J. K.; Vojvodic, A. Surface Energetics of Alkaline-Earth Metal Oxides : Trends in Stability and Adsorption of Small Molecules. *Phys. Rev. B* **2015**, *91*, 155401–155410.

(77) Strickland-Constable, R. F. *Kinetics And Mechanisms of Crystallization*; Acememic Press: London and New York, 1968.

(78) Rossmeisl, J.; Logadottir, a.; Nørskov, J. K. Electrolysis of Water on (Oxidized) Metal Surfaces. *Chem. Phys.* **2005**, *319*, 178–184.

(79) Rossmeisl, J.; Qu, Z. W.; Zhu, H.; Kroes, G. J.; Nørskov, J. K. Electrolysis of Water on Oxide Surfaces. *J. Electroanal. Chem.* **2007**, *607*, 83–89.

(80) Valdés, Á.; Qu, Z. W.; Kroes, G. J.; Rossmeisl, J.; Nørskov, J. K. Oxidation and Photo-Oxidation of Water on TiO2 Surface. *J. Phys. Chem. C* **2008**, *112*, 9872–9879.

(81) Hansen, H. A.; Rossmeisl, J.; Nørskov, J. K. Surface Pourbaix Diagrams and Oxygen Reduction Activity of Pt, Ag and Ni(111) Surfaces Studied by DFT. *Phys. Chem. Chem. Phys.* **2008**, *10*, 3722–3730.

(82) Koper, M. T. M. Thermodynamic Theory of Multi-Electron Transfer Reactions:

Implications for Electrocatalysis. *J. Electroanal. Chem.* **2011**, *660*, 254–260.

(83) Viswanathan, V.; Hansen, H. A.; Rossmeisl, J.; Nørskov, J. K. Universality in Oxygen Reduction Electrocatalysis on Metal Surfaces. *ACS Catal.* **2012**, *2*, 1654–1660.

(84) Angamuthu, R.; Byers, P.; Lutz, M.; Spek, A. L.; Bouwman, E. Electrocatalytic CO2 Conversion to Oxalate by a Copper Complex. *Science (80-.).* **2010**, *327*, 313–315.

(85) Mo, Y.; Ong, S. P.; Ceder, G. First-Principles Study of the Oxygen Evolution Reaction of Lithium Peroxide in the Lithium-Air Battery. *Phys. Rev. B* **2011**, *84*, 205446.

(86) Lu, Y.; Shao-horn, Y. Probing the Reaction Kinetics of the Charge Reactions of Nonaqueous Li-O2 Batteries. *J. Phys. Chem. Lett.* **2013**, *4*, 93–99.

(87) Ren, X.; Wu, Y. A Low-Overpotential Potassium-Oxygen Battery Based on Potassium Superoxide. *J. Am. Chem. Soc.* **2013**, *135*, 2923–2926.

(88) Mccloskey, B. D.; Garcia, J. M.; Luntz, A. C. Chemical and Electrochemical Differences in Nonaqueous Li−O2 and Na−O2 Batteries. *J. Phys. Chem. Lett.* **2014**, *5*, 1230–1235.

(89) Sun, Q.; Yang, Y.; Fu, Z.-W. Electrochemical Properties of Room Temperature Sodium–Air Batteries with Non-Aqueous Electrolyte. *Electrochem. commun.* **2012**, *16*, 22–25.

(90) Nørskov, J. K.; Bligaard, T.; Hvolbæk, B.; Abild-Pedersen, F.; Chorkendorff, I.; Christensen, C. H. The Nature of the Active Site in Heterogeneous Metal Catalysis. *Chem. Soc. Rev.* **2008**, *37*, 2163–2171.

(91) Viswanathan, V.; Thygesen, K. S.; Hummelshøj, J. S.; Nørskov, J. K.; Girishkumar, G.; McCloskey, B. D.; Luntz, a C. Electrical Conductivity in Li2O2 and Its Role in Determining Capacity Limitations in Non-Aqueous Li-O2 Batteries. *J. Chem. Phys.* **2011**, *135*, 214704.

(92) Smith, J. G.; Naruse, J.; Hiramatsu, H.; Siegel, D. J. Theoretical Limiting Potentials in Mg/O 2 Batteries. *Chem. Mater.* **2016**, *28*, 1390–1401.

(93) Vardar, G.; Smith, J. G.; Thompson, T.; Inagaki, K.; Naruse, J.; Hiramatsu, H.; Sleightholme, A. E. S.; Sakamoto, J.; Siegel, D. J.; Monroe, C. W. A Mg/O2 Battery Based on the MACC Electrolyte. *Chem. Mater.* **2016**, *28*, 7629–7637.

(94) Garcia-Lastra, J. M.; Myrdal, J. S. G.; Christensen, R.; Thygesen, K. S.; Vegge, T. DFT+U Study of Polaronic Conduction in Li2O2 and Li2CO3: Implications for Li-Air Batteries. *J. Phys. Chem. C* **2013**, *117*, 5568–5577.

(95) Radin, M. D.; Siegel, D. J. Charge Transport in Lithium Peroxide: Relevance for Rechargeable Metal–Air Batteries. *Energy Environ. Sci.* **2013**, *6*, 2370–2379.

(96) Girishkumar, G.; McCloskey, B.; Luntz, A. C.; Swanson, S.; Wilcke, W. Lithium−Air Battery: Promise and Challenges. *J. Phys. Chem. Lett.* **2010**, *1*, 2193–2203.

(97) Radin, M. D.; Monroe, C. W.; Siegel, D. J. Impact of Space-Charge Layers on Sudden Death in Li/O2 Batteries. *J. Phys. Chem. Lett.* **2015**, *6*, 3017–3022.

(98) Radin, M. D.; Monroe, C. W.; Siegel, D. J. How Dopants Can Enhance Charge Transport in Li2O2. *Chem. Mater.* **2015**, *27*, 839–847.

(99) Tian, F.; Radin, M. D.; Siegel, D. J. Enhanced Charge Transport in Amorphous Li2O2. *Chem. Mater.* **2014**, *26*, 2952–2959.

(100) Radin, M. D.; Tian, F.; Siegel, D. J. Electronic Structure of Li2O2 {0001} Surfaces. *J. Mater. Sci.* **2012**, *47*, 7564–7570.

(101) Lempicki, A. The Electrical Conductivity of MgO Single Crystals at High Temperatures. *Proc. Phys. Soc.* **1953**, *66*, 281–283.

(102) Mansfield, R. The Electrical Conductivity and Thermoelectric Power of Magnesium Oxide. *Proc. Phys. Soc.* **1953**, *66*, 612–614.

(103) Kathrein, H.; Knipping, U.; Freund, F. Atomic Carbon in Magnesium Oxide, Part VI, Electrical Conductivity. *Mat. Res. Bull.* **1980**, *15*, 1393–1399.

(104) Kathrein, H.; Freund, F. Electrical Conductivity of Magnesium Oxide Single Crystal below 1200 K. *J. Phys. Chem. Solids* **1983**, *44*, 177–186.

(105) Yamaka, E.; Sawamoto, K. Electrical Conductivity and Thermo-Electric Motive Force in MgO Single Crystal. *J. Phys. Soc. Japan* **1955**, *10*, 176–179.

(106) Mitoff, S. P. Electrical Conductivity of Single Crystals of MgO. *J. Chem. Phys.* **1959**, *31*, 1261–1269.

(107) Mitoff, S. P. Electronic and Ionic Conductivity in Single Crystals of MgO. *J. Chem. Phys.* **1962**, *36*, 1383–1389.

(108) Davies, M. O. Transport Phenomena in Pure and Doped Magnesium Oxide. *J. Chem. Phys.* **1963**, *38*, 2047–2055.

(109) Lewis, T. J.; Wright, A. J. The Electrical Conductivity of Magnesium Oxide at Low Temperatures. *J. Physics. D.* **1968**, *1*, 441–447.

(110) Osburn, C. M.; Vest, R. W. Electrical Properties of Single Crystals, Bicrystals, and Polycrystals of MgO. *J. Am. Ceram. Soc.* **1971**, *54*, 428–435.

(111) Sempolinski, D. R.; Kingery, W. D. Ionic Conductivity and Magnesium Vacancy Mobility in Magnesium Oxide. *J. Am. Ceram. Soc.* **1980**, *63*, 664–669.

(112) Sempolinski, D. R.; Kingery, W. D.; Tuller, H. L. Electronic Conductivity of Single Crystalline Magnesium Oxide. *J. Am. Ceram. Soc.* **1980**, *63*, 669–675.

(113) Freund, F.; Freund, M.; Batllo, F. Critical Review of Electrical Conductivity Measurements and Charge Distribution Analysis of Magnesium Oxide. *J. Geophys. Res.* **1993**, *98*, 209–229.

(114) Batllo, F.; Leroy, R. C.; Parvin, K.; Freund, F. Dissociation of O2-2 Defects into Paramagnetic O- in Wide Band-Gap Insulators: A Magnetic Susceptibility Study of Magnesium Oxide. *J. Appl. Phys.* **1990**, *67*, 5844–5846.

(115) Batllo, F.; Leroy, R. C.; Parvin, K.; Freund, F.; Freund, M. M. Positive Holes in Magnesium Oxide. Correlation between Magnetic, Electric, and Dielectric Anomalies. *J. Appl. Phys.* **1991**, *69*, 6031–6033.

(116) Catlow, C. R. A.; Faux, I. D.; Norgett, M. J. Shell and Breathing Shell Model Calculations for Defect Formation Energies and Volumes in Magnesium Oxide. *J. Phys. C Solid State Phys.* **1976**, *9*, 419–430.

(117) Mackrodt, W. C.; Stewart, R. F. Defect Properties of Ionic Solids. II. Point Defect Energies Based on Modified Electron-Gas Potentials. *J. Phys. C Solid State Phys.* **1979**, *12*, 431–449.

(118) Mackrodt, W. C.; Stewart, R. F. Defect Properties of Ionic Solids. III. The Calculation of the Point-Defect Structure of the Alkaline-Earth Oxides and CdO. *J. Phys. C Solid State Phys.* **1979**, *12*, 5015–5036.

(119) Sangster, M. J. L.; Rowell, D. K. Calculation of Defect Energies and Volumes in Some Oxides. *Philos. Mag. A* **1981**, *44*, 613–624.

(120) Grimes, R. W.; Catlow, C. R. A. Modeling Localized Defects in Ionic Materials Using Mott-Littleton and Embedded Quantum Cluster Methodology. *J. Am. Ceram. Soc.* **1990**, *73*, 3251–3256.

(121) Grüneis, A. Efficient Explicitly Correlated Many-Electron Perturbation Theory for Solids: Application to the Schottky Defect in MgO. *Phys. Rev. Lett.* **2015**, *115*, 066402.

(122) De Vita, A.; Gillan, M. J.; Lin, J. S.; Payne, M. C.; Stich, I.; Clarke, L. J. Defect Energetics

in MgO Treated by First-Principles Methods. *Phys. Rev. B* **1992**, *46*, 12964–12973.

(123) Vočadlo, L.; Wall, A.; Parker, S. C.; Price, G. D. Absolute Ionic Diffusion in MgO-Computer Calculations via Lattice Dynamics. *Phys. Earth Planet. Inter.* **1995**, *88*, 193–210.

(124) Busker, G.; Van Huis, M. A.; Grimes, R. W.; Van Veen, A. Predicted Vacancy Cluster Structures in MgO and Their Interaction with Helium. *Nucl. Instruments Methods Phys. Res. Sect. B Beam Interact. with Mater. Atoms* **2000**, *171*, 528–536.

(125) Alfè, D.; Gillan, M. J. Schottky Defect Formation Energy in MgO Calculated by Diffusion Monte Carlo. *Phys. Rev. B* **2005**, *71*, 220101.

(126) Uberuaga, B. P.; Smith, R.; Cleave, A. R.; Henkelman, G.; Grimes, R. W.; Voter, A. F.; Sickafus, K. E. Dynamical Simulations of Radiation Damage and Defect Mobility in MgO. *Phys. Rev. B* **2005**, *71*, 104102.

(127) Gilbert, C. A.; Kenny, S. D.; Smith, R.; Sanville, E. Ab Initio Study of Point Defects in Magnesium Oxide. *Phys. Rev. B* **2007**, *76*, 184103.

(128) Runevall, O.; Sandberg, N. Self-Diffusion in MgO—a Density Functional Study. *J. Phys. Condens. Matter* **2011**, *23*, 345402.

(129) Mulroue, J.; Duffy, D. An Ab Initio Study of the Effect of Charge Localization on Oxygen Defect Formation and Migration Energies in Magnesium Oxide. *Proc. R. Soc. London. A. Math. Phys. Sci.* **2011**, *467*, 2054–2065.

(130) Viswanathan, V.; Thygesen, K. S.; Hummelshøj, J. S.; Nørskov, J. K.; Girishkumar, G.; McCloskey, B. D.; Luntz, A. C. Electrical Conductivity in Li 2 O 2 and Its Role in Determining Capacity Limitations in Non-Aqueous Li-O 2 Batteries. *J. Chem. Phys.* **2011**, *135*, 214704.

(131) Lee, B.; Kim, J.; Yoon, G.; Lim, H. D.; Choi, I. S.; Kang, K. Theoretical Evidence for Low Charging Overpotentials of Superoxide Discharge Products in Metal-Oxygen Batteries. *Chem. Mater.* **2015**, *27*, 8406–8413.

(132) Kang, J.; Jung, Y. S.; Wei, S.-H.; Dillon, A. C. Implications of the Formation of Small Polarons in Li2O2 for Li-Air Batteries. *Phys. Rev. B* **2012**, *85*, 035210.

(133) Ong, S. P.; Mo, Y.; Ceder, G. Low Hole Polaron Migration Barrier in Lithium Peroxide. *Phys. Rev. B* **2012**, *85*, 081105.

(134) Gerbig, O.; Merkle, R.; Maier, J. Electron and Ion Transport in Li2O2. *Adv. Mater.* **2013**, *25*, 3129–3133.

(135) Lu, Y.-C.; Kwabi, D. G.; Yao, K. P. C.; Harding, J. R.; Zhou, J.; Zuin, L.; Shao-Horn, Y. The Discharge Rate Capability of Rechargeable Li–O2 Batteries. *Energy Environ. Sci.* **2011**, *4*, 2999–3007.

(136) Timoshevskii, V.; Feng, Z.; Bevan, K. H.; Goodenough, J.; Zaghib, K. Improving Li2O2 Conductivity via Polaron Preemption: An Ab Initio Study of Si Doping. *Appl. Phys. Lett.* **2013**, *103*, 073901.

(137) Araujo, R. B.; Chakraborty, S.; Ahuja, R. Unveiling the Charge Migration Mechanism in Na2O2: Implications for Sodium–Air Batteries. *Phys. Chem. Chem. Phys.* **2015**, *17*, 8203–8209.

(138) Yang, S.; Siegel, D. J. Intrinsic Conductivity in Sodium–Air Battery Discharge Phases: Sodium Superoxide vs Sodium Peroxide. *Chem. Mater.* **2015**, *27*, 3852–3860.

(139) Gerbig, O.; Merkle, R.; Maier, J. Electrical Transport and Oxygen Exchange in the Superoxides of Potassium, Rubidium, and Cesium. *Adv. Funct. Mater.* **2015**, *25*, 2552–2563.

(140) Sasaki, K.; Maier, J. Low-Temperature Defect Chemistry of Oxides . I. General Aspects

and Numerical Calculations. *J. Appl. Phys.* **1999**, *10*, 5422–5433.

(141) Maier, J. Complex Oxides: High Temperature Defect Chemistry vs. Low Temperature Defect Chemistry. *Phys. Chem. Chem. Phys.* **2003**, *5*, 2164–2173.

(142) Maier, J. High Temperature versus Low Temperature Defect Chemistry. *Solid State Ionics* **2004**, *173*, 1–8.

(143) Whittingham, M. S. Lithium Batteries and Cathode Materials. *Chem. Rev.* **2004**, *104*, 4271–4301.

(144) Sheppard, D.; Terrell, R.; Henkelman, G. Optimization Methods for Finding Minimum Energy Paths. *J. Chem. Phys.* **2008**, *128*, 134106.

(145) Henkelman, G.; Jónsson, H. Improved Tangent Estimate in the Nudged Elastic Band Method for Finding Minimum Energy Paths and Saddle Points. *J. Chem. Phys.* **2000**, *113*, 9978–9985.

(146) Henkelman, G.; Uberuaga, B. P.; Jónsson, H. A Climbing Image Nudged Elastic Band Method for Finding Saddle Points and Minimum Energy Paths. *J. Chem. Phys.* **2000**, *113*, 9901–9904.

(147) Shishkin, M.; Kresse, G. Implementation and Performance of the Frequency-Dependent GW Method within the PAW Framework. *Phys. Rev. B* **2006**, *74*, 035101.

(148) Shishkin, M.; Marsman, M.; Kresse, G. Accurate Quasiparticle Spectra from Self-Consistent GW Calculations with Vertex Corrections. *Phys. Rev. Lett.* **2007**, *99*, 246403.

(149) Heyd, J.; Scuseria, G. E.; Ernzerhof, M. Hybrid Functionals Based on a Screened Coulomb Potential. *J. Chem. Phys.* **2003**, *118*, 8207–8215.

(150) Krukau, A. V; Vydrov, O. a; Izmaylov, A. F.; Scuseria, G. E. Influence of the Exchange Screening Parameter on the Performance of Screened Hybrid Functionals. *J. Chem. Phys.* **2006**, *125*, 224106.

(151) Makov, G.; Payne, M. C. Periodic Boundary Conditions in Ab Initio Calculations. *Phys. Rev. B* **1995**, *51*, 4014–4022.

(152) Komsa, H.-P.; Rantala, T. T.; Pasquarello, A. Finite-Size Supercell Correction Schemes for Charged Defect Calculations. *Phys. Rev. B* **2012**, *86*, 045112.

(153) Gajdoš, M.; Hummer, K.; Kresse, G.; Furthmüller, J.; Bechstedt, F. Linear Optical Properties in the Projector-Augmented Wave Methodology. *Phys. Rev. B* **2006**, *73*, 045112.

(154) Wang, L.; Maxisch, T.; Ceder, G. Oxidation Energies of Transition Metal Oxides within the GGA+U Framework. *Phys. Rev. B* **2006**, *73*, 195107.

(155) Van de Walle, C. G.; Neugebauer, J. First-Principles Calculations for Defects and Impurities: Applications to III-Nitrides. *J. Appl. Phys.* **2004**, *95*, 3851–3879.

(156) Lidiard, A. *Handbuch Der Physik Vol. XX*; Flugge, S., Ed.; Springer-Verlag: Berlin, 1957.

(157) Tilley, Richard, J. D. *Defects in Solids*; John Wiley & Sons, Inc., 2008.

(158) Shishkin, M.; Kresse, G. Self-Consistent GW Calculations for Semiconductors and Insulators. *Phys. Rev. B* **2007**, *75*, 235102.

(159) Whited, R. C.; Flaten, C. J.; Walker, W. C. Exciton Thermoreflectance of MgO and CaO. *Solid State Commun.* **1973**, *13*, 1903–1905.

(160) Strehlow, W. H.; Cook, E. L. Compilation of Energy Band Gaps in Elemental and Binary Compound Semiconductors and Insulators. *J. Phys. Chem. Ref. Data* **1973**, *2*, 163–200.

(161) Sproul, A. B.; Green, M. A.; Zhao, J. Improved Value for the Silicon Intrinsic Carrier Concentration at 300 K. *Appl. Phys. Lett.* **1990**, *57*, 255–257.

(162) Freund, M. M.; Freund, F.; Batllo, F. Highly Mobile Oxygen Holes in Magnesium Oxide. *Phys. Rev. Lett.* **1989**, *63*, 2096–2099.

(163) Mackrodt, W. C. Defect Calculations for Ionic Materials. In *Computer Simulation of Solids*; Mackrodt, W. C., Catlow, C. R. A., Eds.; Springer-Verlag: Berlin, 1982; p 175.

(164) Sangster, M. J. L.; Peckham, G.; Saunderson, D. H. Lattice Dynamics of Magnesium Oxide. *J. Phys. C Solid State Phys.* **1970**, *3*, 1026–1036.

(165) Masetti, G.; Severi, M.; Solmi, S. Modeling of Carrier Mobility Against Carrier Concentration in Arsenic-, Phosphorus-, and Boron-Doped Silicon. *IEEE Trans. Electron Devices* **1983**, *30*, 764–769.

(166) Kroger, F. A.; Vink, H. J. Relations between the Concentrations of Imperfections in Crystalline Solids. *Solid State Phys.* **1956**, *3*, 307–435.

(167) Kroger, F. A. *The Chemistry of Imperfect Crystals*; North-Holland Publishing Company Amsterdam, 1964.

(168) Chen, Y.; Kernohan, R. H.; Boldu, J. L.; Abraham, M. . Enhancement of Electrical Conductivity in MgO Due to Lithium Impurities. *Solid State Commun.* **1980**, *33*, 441–443.

(169) Tardío, M.; Ramírez, R.; González, R.; Pinto, J. V.; Da Silva, R. C.; Alves, E.; Chen, Y. Electrical Conductivity of As-Grown and Oxidized MgO:Li Crystals Implanted with Li Ions. *Nucl. Instruments Methods Phys. Res. Sect. B Beam Interact. with Mater. Atoms* **2004**, *218*, 164–169.

(170) Jost, W. Berechnung Der Grosse Und Druckabhangigkeit von Ionen-Fehlordnungsenergien Und Beweglichkeiten in Kristallen. *Phys. Zeitschrift* **1935**, *36*, 757–760.

(171) Crabtree, G.; Kócs, E.; Trahey, L. The Energy-Storage Frontier: Lithium-Ion Batteries and Beyond. *MRS Bull.* **2015**, *40*, 1067–1076.

(172) Stillinger, F. H. A Topographic View of Supercooled Liquids and Glass Formation. *Science (80-.).* **1995**, *267*, 1935–1939.

(173) Sastry, S.; Debenedetti, P. G.; Stillinger, F. H. Signatures of Distinct Dynamical Regimes in the Energy Landscape of a Glass-Forming Liquid. *Nature* **1998**, *393*, 554–557.

(174) Debenedetti, P. G.; Stillinger, F. H. Supercooled Liquids and the Glass Transition. *Nature* **2001**, *410*, 259–267.

(175) Tuller, H. .; Button, D. .; Uhlmann, D. . Fast Ion Transport in Oxide Glasses. *J. Non. Cryst. Solids* **1980**, *40*, 93–118.

(176) Miyagawa, H.; Hiwatari, Y.; Bernu, B.; Hansen, J. P. Molecular Dynamics Study of Binary Soft-sphere Mixtures: Jump Motions of Atoms in the Glassy State. *J. Chem. Phys.* **1988**, *88*, 3879–3886.

(177) Roux, J. N.; Barrat, J. L.; Hansen, J. P. Dynamical Diagnostics for The Glass-Transition in Soft-Sphere Alloys. *J. Phys. Condens. Matter* **1989**, *1*, 7171–7186.

(178) Barrat, J. L.; Roux, J. N.; Hansen, J. P. Diffusion, Viscosity and Structural Slowing down in Soft Sphere Alloys near the Kinetic Glass Transition. *Chem. Phys.* **1990**, *149*, 197–208.

(179) Wahnström, G. Molecular-Dynamics Study of a Supercooled Two-Component Lennard-Jones System. *Phys. Rev. A* **1991**, *44*, 3752–3764.

(180) Kob, W.; Donati, C.; Plimpton, S. J.; Poole, P. H.; Glotzer, S. C. Dynamical Heterogeneities in a Supercooled Lennard-Jones Liquid. *Phys. Rev. Lett.* **1997**, *79*, 2827–2830.

(181) Donati, C.; Douglas, J. F.; Kob, W.; Plimpton, S. J.; Poole, P. H.; Glotzer, S. C. Stringlike Cooperative Motion in a Supercooled Liquid. *Phys. Rev. Lett.* **1998**, *80*, 2338–2341.

(182) Donati, C.; Glotzer, S. C.; Poole, P. H.; Kob, W.; Plimpton, S. J. Spatial Correlations of Mobility and Immobility in a Glass-Forming Lennard-Jones Liquid. *Phys. Rev. E* **1999**, *60*, 3107–3119.

(183) Glotzer, S. C.; Ediger, M. D. Spatially Heterogeneous Dynamics in Supercooled Liquids. *J.*

Non-Crystalline Solids **2000**, *51*, 342–355.

(184) Chaudhuri, P.; Berthier, L.; Kob, W. Universal Nature of Particle Displacements Close to Glass and Jamming Transitions. *Phys. Rev. Lett.* **2007**, *99*, 2–5.

(185) Chaudhuri, P.; Sastry, S.; Kob, W. Tracking Heterogeneous Dynamics during the α Relaxation of a Simple Glass Former. *Phys. Rev. Lett.* **2008**, *101*, 1–4.

(186) Yokota, I. On the Deviation from the Einstein Relation Observed for Diffusion of Ag+ Ions in Alpha-Ag2S and Others. *J. Phys. Soc. Japan* **1966**, *21*, 420–423.

(187) Kvist, A.; Bengtzelius, A. Tracer Diffusion and Electrical Conductivity of Cubic Lithium Sulphate and a Transport Model for Cubic Sulphates. In *Fast ion transport in solids*; van Gool, W., Ed.; Noth-Holland Publishing Company: Amsterdam, 1973; pp 193–199.

(188) Jalem, R.; Yamamoto, Y.; Shiiba, H.; Nakayama, M.; Munakata, H.; Kasuga, T.; Kanamura, K. Concerted Migration Mechanism in the Li Ion Dynamics of Garnet-Type Li 7La3Zr2O12. *Chem. Mater.* **2013**, *25*, 425–430.

(189) Meier, K.; Laino, T.; Curioni, A. Solid-State Electrolytes: Revealing the Mechanisms of Li-Ion Conduction in Tetragonal and Cubic LLZO by First-Principles Calculations. *J. Phys. Chem. C* **2014**, *118*, 6668–6679.

(190) Burbano, M.; Carlier, D.; Boucher, F.; Morgan, B. J.; Salanne, M. Sparse Cyclic Excitations Explain the Low Ionic Conductivity of Stoichiometric Li7La3Zr2 O12. *Phys. Rev. Lett.* **2016**, *116*, 1–6.

(191) Xu, M.; Ding, J.; Ma, E. One-Dimensional Stringlike Cooperative Migration of Lithium Ions in an Ultrafast Ionic Conductor. *Appl. Phys. Lett.* **2012**, *101*.

(192) He, X.; Zhu, Y.; Mo, Y. Origin of Fast Ion Diffusion in Super-Ionic Conductors. *Nat. Commun.* **2017**, *8*, 15893.

(193) Varley, J. B.; Kweon, K.; Mehta, P.; Shea, P.; Heo, T. W.; Udovic, T. J.; Stavila, V.; Wood, B. C. Understanding Ionic Conductivity Trends in Polyborane Solid Electrolytes from Ab Initio Molecular Dynamics. *ACS Energy Lett.* **2017**, *2*, 250–255.

(194) Kweon, K. E.; Varley, J. B.; Shea, P.; Adelstein, N.; Mehta, P.; Heo, T. W.; Udovic, T. J.; Stavila, V.; Wood, B. C. Structural, Chemical, and Dynamical Frustration: Origins of Superionic Conductivity in Closo-Borate Solid Electrolytes. *Chem. Mater.* **2017**, acs.chemmater.7b02902.

(195) Kresse, G.; Joubert, D. From Ultrasoft Pseudopotentials to the Projector Augmented-Wave Method. *Phys. Rev. B* **1999**, *59*, 1758–1775.

(196) Dassault Systemes BIOVIA, Amorphous Cell Module. San Diego 2017.

(197) Sun, H.; Jin, Z.; Yang, C.; Akkermans, R. L. C.; Robertson, S. H.; Spenley, N. A.; Miller, S.; Todd, S. M. COMPASS II: Extended Coverage for Polymer and Drug-like Molecule Databases. *J. Mol. Model.* **2016**, *22*, 1–10.

(198) Parrinello, M.; Rahman, A. Polymorphic Transitions in Single Crystals: A New Molecular Dynamics Method. *J. Appl. Phys.* **1981**, *52*, 7182–7190.

(199) Homma, K.; Yonemura, M.; Kobayashi, T.; Nagao, M.; Hirayama, M.; Kanno, R. Crystal Structure and Phase Transitions of the Lithium Ionic Conductor Li3PS4. *Solid State Ionics* **2011**, *182*, 53–58.

(200) Ohara, K.; Mitsui, A.; Mori, M.; Onodera, Y.; Shiotani, S.; Koyama, Y.; Orikasa, Y.; Murakami, M.; Shimoda, K.; Mori, K.; et al. Structural and Electronic Features of Binary Li2S-P2S5 Glasses. *Sci. Rep.* **2016**, *6*, 21302.

(201) Sears, V. F. Neutron Scattering Lengths and Cross Sections. *Neutron News* **1992**, *3*, 26–37.

(202) Keen, D. A. A Comparison of Various Commonly Used Correlation Functions for

Describing Total Scattering. *J. Appl. Crystallogr.* **2001**, *34*, 172–177.

(203) Keys, A. S.; Hedges, L. O.; Garrahan, J. P.; Glotzer, S. C.; Chandler, D. Excitations Are Localized and Relaxation Is Hierarchical in Glass-Forming Liquids. *Phys. Rev. X* **2011**, *1*, 1–15.

(204) Lundén, A. Enhancement of Cation Mobility in Some Sulphate Phases Due to a Paddle-Wheel Mechanism. *Solid State Ionics* **1988**, *28–30*, 163–167.

(205) Jansen, M. Volume Effect or Paddle-Wheel Mechanism—Fast Alkali-Metal Ionic Conduction in Solids with Rotationally Disordered Complex Anions. *Angew. Chemie Int. Ed. English* **1991**, *30*, 1547–1558.

(206) Wilmer, D.; Funke, K.; Witschas, M.; Banhatti, R. D.; Jansen, M.; Korus, G.; Fitter, J.; Lechner, R. E. Anion Reorientation in an Ion Conducting Plastic Crystal - Coherent Quasielastic Neutron Scattering from Sodium Ortho-Phosphate. *Phys. B Condens. Matter* **1999**, *266*, 60–68.

(207) Hull, S. Superionics: Crystal Structures and Conduction Processes. *Reports Prog. Phys.* **2004**, *67*, 1233–1314.

(208) Lynden-Bell, R. M.; Michel, K. H. Translation-Rotation Coupling, Phase Transitions, and Elastic Phenomena in Orientationally Disordered Crystals. *Rev. Mod. Phys.* **1994**, *66*, 721–762.

(209) Verdal, N.; Udovic, T. J.; Stavila, V.; Tang, W. S.; Rush, J. J.; Skripov, A. V. Anion Reorientations in the Superionic Conducting Phase of Na2B12H12. *J. Phys. Chem. C* **2014**, *118*, 17483–17489.

(210) Hansen, J. P.; McDonald, I. R. *Theory of Simple Liquids*, 4th ed.; Acememic Press, 2013.

(211) Sakuda, A.; Hayashi, A.; Tatsumisago, M. Sulfide Solid Electrolyte with Favorable Mechanical Property for All-Solid-State Lithium Battery. *Sci. Rep.* **2013**, *3*, 2261.

(212) Sakuda, A.; Hayashi, A.; Takigawa, Y.; Higashi, K.; Tatsumisago, M. Evaluation of Elastic Modulus of Li2S–P2S5 Glassy Solid Electrolyte by Ultrasonic Sound Velocity Measurement and Compression Test. *J. Ceram. Soc. Japan* **2013**, *121*, 946–949.

(213) McGrogan, F. P.; Swamy, T.; Bishop, S. R.; Eggleton, E.; Porz, L.; Chen, X.; Chiang, Y.-M.; Van Vliet, K. J. Compliant Yet Brittle Mechanical Behavior of Li 2 S-P 2 S 5 Lithium-Ion-Conducting Solid Electrolyte. *Adv. Energy Mater.* **2017**, *7*, 1602011.

(214) Le Page, Y.; Saxe, P. Symmetry-General Least-Squares Extraction of Elastic Data for Strained Materials from *Ab Initio* Calculations of Stress. *Phys. Rev. B* **2002**, *65*, 104104.

(215) Hill, R. The Elastic Behaviour of a Crystalline Aggregate. *Proc. Phys. Soc. Sect. A* **1952**, *65*, 349–354.

(216) Deng, Z.; Wang, Z.; Chu, I.-H.; Luo, J.; Ong, S. P. Elastic Properties of Alkali Superionic Conductor Electrolytes from First Principles Calculations. *J. Electrochem. Soc.* **2016**, *163*, A67–A74.

(217) Yang, Y.; Wu, Q.; Cui, Y.; Chen, Y.; Shi, S.; Wang, R.-Z.; Yan, H. Elastic Properties, Defect Thermodynamics, Electrochemical Window, Phase Stability, and Li + Mobility of Li 3 PS 4 : Insights from First-Principles Calculations. *ACS Appl. Mater. Interfaces* **2016**, *8*, 25229–25242.

(218) Dietrich, C.; Weber, D.; Sedlmaier, S. J.; Indris, S.; Culver, S.; Walter, D.; Janek, J.; Zeier, W. Lithium Ion Conductivity in Li 2 S-P 2 S 5 Glasses – Building Units and Local Structure Evolution during the Crystallization of the Superionic Conductors Li 3 PS 4 , Li 7 P 3 S 11 and Li 4 P 2 S 7. *J. Mater. Chem. A* **2017**, 18111–18119.

(219) Baroni, S.; Gironcoli, S. De; Corso, A. D.; Scuola, S.; Superiore, I.; Istituto, I.; Materia, F.;

Trieste, I.-; Giannozzi, P. Phonons and Related Crystal Properties from Density-Functional Pertubation Theory. *Rev. Mod. Phys.* **2001**, *73*.